University of Tennessee, Knoxville
Trace: Tennessee Research and Creative Exchange

Doctoral Dissertations | Graduate School

5-2006

Magnetism and Transport Properties of Transition Metal Oxides and Nanoparticles

Dane Thomas Gillaspie
University of Tennessee - Knoxville

Recommended Citation

Gillaspie, Dane Thomas, "Magnetism and Transport Properties of Transition Metal Oxides and Nanoparticles. " PhD diss., University of Tennessee, 2006.
https://trace.tennessee.edu/utk_graddiss/1669

This Dissertation is brought to you for free and open access by the Graduate School at Trace: Tennessee Research and Creative Exchange. It has been accepted for inclusion in Doctoral Dissertations by an authorized administrator of Trace: Tennessee Research and Creative Exchange. For more information, please contact trace@utk.edu.

To the Graduate Council:

I am submitting herewith a dissertation written by Dane Thomas Gillaspie entitled "Magnetism and Transport Properties of Transition Metal Oxides and Nanoparticles." I have examined the final electronic copy of this dissertation for form and content and recommend that it be accepted in partial fulfillment of the requirements for the degree of Doctor of Philosophy, with a major in Physics.

E. Ward Plummer, Major Professor

We have read this dissertation and recommend its acceptance:

Robert Compton, Pengcheng Dai, Philip Rack, Jian Shen

Accepted for the Council:
Dixie L. Thompson

Vice Provost and Dean of the Graduate School

(Original signatures are on file with official student records.)

To the Graduate Council:

I am submitting herewith a dissertation written by Dane Thomas Gillaspie entitled "Magnetism and Transport Properties of Transition Metal Oxides and Nanoparticles." I have examined the final electronic copy of this dissertation for form and content and recommend that it be accepted in partial fulfillment of the requirements for the degree of Doctor of Philosophy, with a major in Physics.

E. Ward Plummer
Major Professor

We have read this dissertation
and recommend its acceptance:

Robert Compton

Pengcheng Dai

Philip Rack

Jian Shen

Accepted for the Council:

Anne Mayhew
Vice Chancellor and
Dean of Graduate Studies

(Original signatures are on file with official student records.)

Magnetism and Transport Properties of Transition Metal Oxides and Nanoparticles

A Dissertation

Presented for the

Doctor of Philosophy Degree

The University of Tennessee, Knoxville

Dane Thomas Gillaspie

May 2006

Copyright © 2006 by Dane Thomas Gillaspie
All rights reserved.

To

my wife

and family

Acknowledgements

I can't believe I'm finally finished. It seems like I made something that is difficult (getting a PHD) look nearly impossible. Without these people, it probably *would* have been impossible.

During the initial coursework and preliminary exam "era," I was very grateful to have JP Pierce, He Jian, Tolik Melechko, Andy Glenn, Khaled Mriziq, and Korey Sorge around. Due to the passage of time and the extreme difficulty of those years, I can't really remember too much about what I did and how I managed to get through, but I *did*, and I am sure I owe a lot of it to those guys.

After I passed the preliminary exams, I started working on ultrafast optical measurements of magnetic thin films, and my primary debt during this time is to Dr. Rüdiger Vollmer. I really wish that things could have worked out differently, so that I could have taken greater advantage of his expertise during his time in East Tennessee. I am also deeply saddened by his death in December, 2005.

Speaking of sad things, I am also deeply grateful to have spent time with Andrea Ross while she was a student in the group. Her death from cancer was a horrible tragedy.

On a happier note, after I stopped working on the ultrafast optics project, I was able to start on the projects that eventually resulted in this dissertation. I am very grateful to my chief advisor, Ward Plummer, since he never gave up on me through all the years of struggle and difficulty. I am glad that my sub-advisor, Jian Shen, was willing to be so generous with his time and allow me to work on all the projects listed in this dissertation as well as several others. Jianxing Ma, Jane Howe, Gyula Eres, Hans Christen, and Wei Wang were all vital to my work, either in preparation of samples, understanding techniques, or understanding the underlying physics. Hong-Ying Zhai and Zhixian Zhou were also always willing to lend a hand whenever I had too much work to do and not

enough hands to complete it. I am also grateful to Dr. N. J. Silva for his help with the distributed-moment nanoparticle data fitting procedure.

Over the years I have also tried to interact with all the other great people at ORNL, especially the other members of the Low Dimensional Materials by Design Group. Art Baddorf and John Wendelken were always very patient whenever I came to them with a foolish question, as were Anping Li and Sergei Kalinin. Outside the LDMD group, I also spent a lot of time talking with David Mandrus, Rongying Jin, Brian Sales, Peter Khalifah, Jay Jellison, and Gabe Veith.

In addition to the people who helped me professionally, I don't think that I could have gotten through all these years of struggle and heartache without Wednesday night basketball or Stonefingers softball.

I am also thankful to the other members of my committee, Bob Compton, Pengcheng Dai, and Philip Rack. They have been very kind and patient with me.

Finally, even though they were already mentioned in the Dedication, I am grateful for the love and support of my wife, family, and friends. I am not sure it's possible to say how much you all mean to me, so I'll just say that I love you and hope that you are proud of me.

Abstract

This dissertation is devoted to the study of the properties of transition metal oxides in both thin film and nanocrystalline forms.

The first section is devoted to the transport properties of manganese oxide thin film samples. The colossal magnetoresistance in these materials is usually explained using double-exchange, but this explanation is only partially correct. Recent theoretical and experimental work has shown that these compounds have a strong tendency towards phase-separation. The impact of strain on phase separation has been investigated by growing films of $La_{5/8-0.3}Pr_{0.3}Ca_{3/8}MnO_3$ on a variety of substrates. Very small changes in the induced strain cause large changes in the magnetic and magnetotransport properties of the film.

The second section is devoted to scanning tunneling microscopy studies of these same films at room temperature. In this case, small localized holes are observed at the Mn^{4+} ion sites. The distribution of holes is non-random and shows strong short range correlation.

The final section of this thesis is devoted to small particles of binary transition metal oxides. These oxides are antiferromagnetic in bulk samples, but when the dimensions of the particle are small (<50nm), they show an enhanced magnetic moment. Nanoparticles of α-Fe_2O_3 have been prepared and their magnetic properties have been measured, and an increase in particle moment versus temperature has been observed using standard analysis techniques. More advanced analysis techniques indicate that this increase is a result of a transition specific to the α-Fe_2O_3 system, and not the result of thermoinduced magnetization

Contents

List of Figures

Chapter 1 Introduction

There is a longstanding tradition in the physical sciences of "rediscovery." This means that fields that have long been dormant can be rediscovered, and startling new insights can be found. As an example, the recent discovery of the superconducting state in MgB_2 only occurred because someone chose to look at simple binary compounds again, even though the field had been extensively researched decades earlier.

Similarly, people can investigate old materials in new forms. Most of this dissertation can be classified this way. Through sophisticated preparation and careful measurement, some of the oldest and most familiar materials still have secrets to tell.

Hematite, the alpha phase of Fe_2O_3, has been part of the human experience since prehistoric times. Naturally occurring hematite powders are known as "ocher," and indigenous people still use them as a natural pigment. The dark, crystalline ore is known as "Alaska black diamond," and it is used in jewelry. Hematite nodules were also discovered on the surface of Mars by the Discovery rover, and this has been accepted as proof that there was once liquid water on the Martian surface. In fact, these hematite nodules are eerily similar to the hematite nanoparticles that form the final chapter of this dissertation. See Figure 1.1 for a comparison.

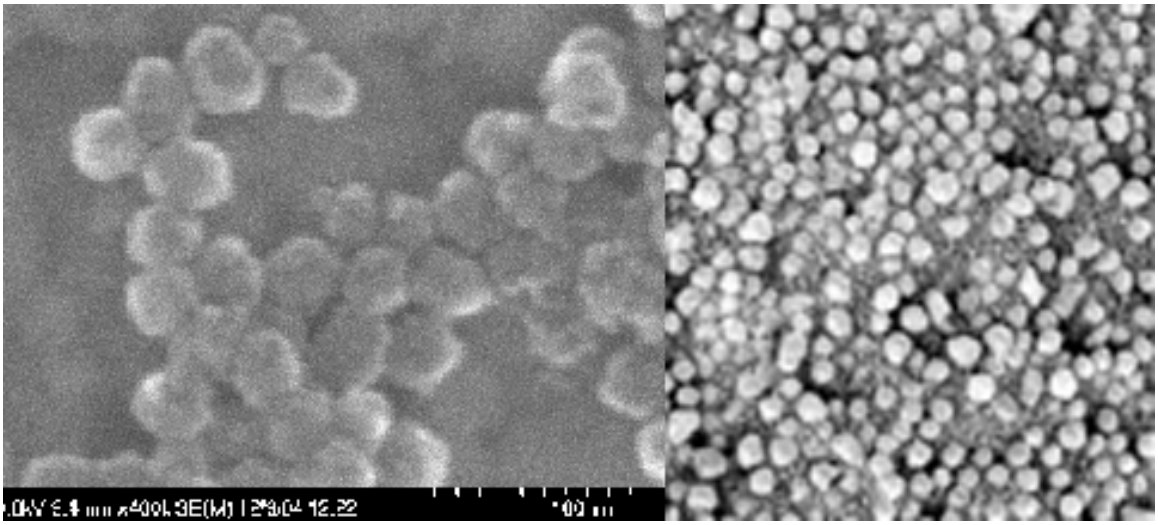

Figure 1.1: Combined image of hematite particles - Left side - nanometer sized particles in ORNL microscope. Right side - millimeter sized particles found by Spirit rover on Mars.

However, I have not *really* studied hematite. In a larger sense, hematite and the other materials I have studied were only tools. The *real* theme of this dissertation is the magnetic structure of transition metal oxides, and the shape and composition of the samples were chosen to help understand the underlying physics through the use of spatial confinement, broken symmetries, and strain.

The hematite nanoparticles were chosen in order to address one of the main topics in this dissertation, which is the anomalously large magnetic moment in antiferromagnetic nanoparticles. This has been studied for at least fifty years, and has been generally understood as being a consequence of uncompensated spins at the surface of the particles. This means that the overall magnetic moment of the particle is dominated by the imperfect surface moments as the size of the particle becomes comparable with the size of the magnetic unit cell. Figure 1.2 shows a simple schematic of this explanation.

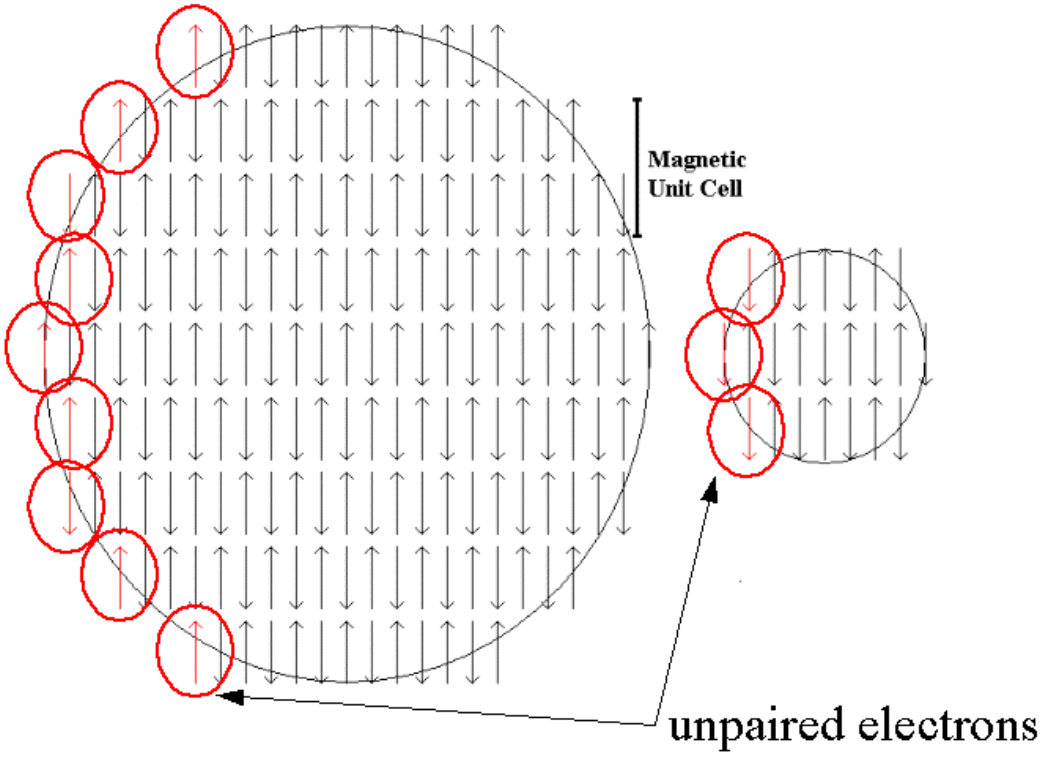

Figure 1.2: Antiferromagnetic particle schematic.

This simple explanation, first suggested by Néel[1], is intuitively satisfying and has long been treated as a complete explanation of the effect. However, recent studies have shown that the real magnetic structure is more complex, and that the Néel picture is at best a partial explanation[2-8]. In fact, the recent work by Mørup and Frandsen[6] attributes the anomalous moment to magnon excitations. More complicated Monte Carlo simulations have been performed by our collaborators at ORNL, and these simulations yield a third set of predictions[2], which will be discussed in Section 2.3.2. These three theories should be testable, and the measurements in the literature seem incomplete. Therefore, a careful study of real samples might help to resolve these issues.

The remainder of this dissertation is devoted to measurements of more complex manganite thin films. These compounds, made famous for their "colossal" magnetoresistance, have very complicated behavior. Take, as an example, the phase diagram for $La_{1-x}Ca_xMnO_3$ in Figure 1.3. Changing the amount of strontium causes dramatic changes in both resistivity and magnetic structure.

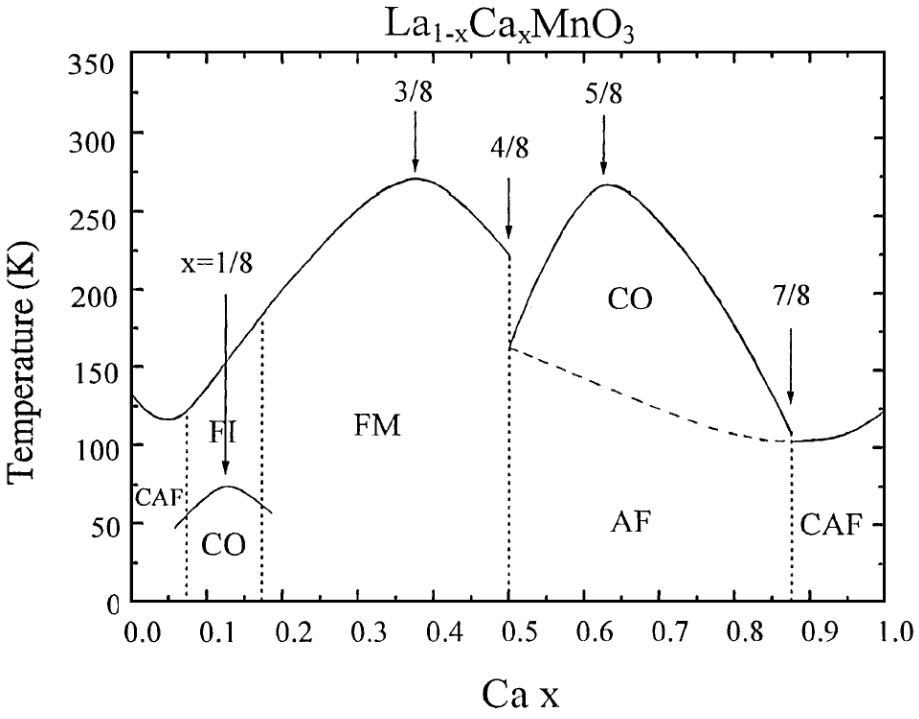

Figure 1.3: Phase diagram for $La_{1-x}Ca_xMnO_3$. FM: Ferromagnetic Mtal, FI: Ferromagnetic Insulator, AF: Antiferromagnetism, CAF: Canted AF, and CO: Charge/Orbital Ordering. FI and/or CAF could be a spatically inhomogeneous state with FM and AF coexistence.

Such complicated behavior naturally requires a complex theory (or two)[9, 10]. An important feature of many of the theories for these materials is phase separation. This implies that the transitions between the different phases listed in the above diagram are not sharp. For example, if the sample is chosen with a value of $x = 0.175$, there should be a transition from ferromagnetic metal at low temperature to paramagnetic metal at high temperature. During the transition, if there is phase separation, then there will be regions of the sample with each type of structure. Starting from high temperature, that would mean that there would be small high-conductivity metallic regions that would increase in size as the temperature is lowered. Eventually, these high-conductivity regions would start to overlap, and then there is a dramatic decrease in the sample resistance as these overlapping regions bridge the sample as a whole.

Chapter 2 Theoretical Background

2.1 Atomic Magnetism

Electromagnetism is the subject of many textbooks, from the excellent[11] to the good[12] to the canonical but pedagogically weak[13]. Unfortunately, these books are not able to give much attention to the field of magnetism in solids. This is partly due to the enormous breadth of material that the textbooks are forced to cover, but it is also due to the complexity of describing magnetism in condensed matter. In truth, most of the interesting magnetic effects in solids are quantum mechanical in nature, so "classical" textbooks cannot do justice to the subject.

For my purposes, it is best to start with the electron. In addition to the normal electrostatic field created by the electron's charge, there is also a magnetic field associated with the electron's spin. If the electron is in motion, there is also a magnetic field associated with its motion. If the electron happens to find itself bonded to an atom, there is also a magnetic field due to the orbital angular motion of the electron around the nucleus of the atom.

For a free atom or ion, the angular momentum and spin of each electron is arranged according to the semi-empirical Hund's rules. These are as follows:

First rule: The total spin quantum number $S = \left| \sum_i s_{iz} \right|$ *is maximized.*

Second rule: The total orbital angular momentum $L = \left| \sum_i l_{iz} \right|$ *is maximized, as long as rule number one is followed.*

Third rule: J=|L+S| if the shell is more than half full, or J=|L-S| if the shell is less than half full. The total magnetic moment of the ion or atom is then $\bar{M} = g\mu_B \bar{J}$.

Following these simple rules, it is then possible to calculate the magnetic moment without resorting to any particular knowledge of the individual atomic species for nearly all atoms. I have included Table 2.1 from Skomski and Coey[14] detailing the ground states of the 3d ions, which covers the magnetic species of all the compounds in this

Table 2.1: Ground States of 3d Ions[14]

	+2	+1	0	-1	-2	S	L	J	g	gJ	p_{eff}
$3d^1$, Ti^{3+}, V^{4+}	↓	-	-	-	-	1/2	2	3/2	4/5	6/5	1.73
$3d^2$, V^{3+}, Cr^{4+}	↓	↓	-	-	-	1	3	2	2/3	4/3	2.83
$3d^3$, Cr^{3+}, Mn^{4+}	↓	↓	↓	-	-	3/2	3	3/2	2/5	3/5	3.87
$3d^4$, Cr^{2+}, Mn^{3+}	↓	↓	↓	↓	-	2	2	0	-	0	4.90
$3d^5$, Mn^{2+}, Fe^{3+}	↓	↓	↓	↓	↓	5/2	0	5/2	2	5	5.92
$3d^6$, Fe^{2+}, Co^{3+}	↑↓	↑	↑	↑	↑	2	2	4	3/2	6	4.90
$3d^7$, Co^{2+}, Ni^{3+}	↑↓	↑↓	↑	↑	↑	3/2	3	9/2	4/3	6	3.87
$3d^8$, Ni^{2+}, Co^{+}	↑↓	↑↓	↑↓	↑	↑	1	3	4	5/4	5	2.83
$3d^9$, Cu^{2+}, Ni^{+}	↑↓	↑↓	↑↓	↑↓	↑	1/2	2	5/2	6/5	3	1.73

dissertation. The effective moment listed in the last column of Table 2.1 is the contribution due to the spin component only. This is the result of orbital-moment quenching which is common in the 3d compounds.

This quenching of the orbital angular momentum in 3d solids is due to the interaction of the d-orbitals with the crystal field formed by the surrounding lattice of ions. The crystal field leads to quenching by favoring the formation of superposition states with zero net magnetic moment. For example, consider a 3d ion in a cubic lattice. The wavefunctions of the electrons in the ion can be written in the usual way.

$$\psi = R_{nl}(r)\Theta_{lm}(\theta)\Phi_m(\phi) \tag{2.1}$$

Recall that the (r,θ,φ) system is defined with the r-coordinate measuring radial distance from the origin. The θ-coordinate measures the angle from the z-axis, and the φ-coordinate measures the equatorial angle from the x-axis. The R and Θ portions of the wavefunction are summarized in Ref. [14] , but they can also be found in any upper-level undergraduate quantum mechanics book.

For our discussion, the most important part of the wavefunction is the azimuthal (φ) part.

$$\Phi_m(\phi) = \frac{1}{\sqrt{2\pi}} e^{im\phi} \tag{2.2}$$

Consider a superposition of the m = ±2 states.

$$\Phi_2(\phi) = \frac{1}{\sqrt{2}\sqrt{2\pi}}(e^{i2\phi} + e^{-i2\phi}) = \frac{1}{\sqrt{\pi}}\cos 2\phi \qquad (2.3)$$

This superposition of wavefunctions puts most of the weight along the sides of the cube. Depending upon the nature of the nearest neighbor interaction, this can then become the lowest energy state. Since the wavefunction is an equal mix of m = ±2 states, there is no net angular momentum, so the magnetic moment is effectively quenched. Similar arguments will apply to almost all of the d-orbitals in the transition metals, so to first order J ≈ S. The saturation moment of 3d ions, measured in Bohr magnetons (μ_B), will then just be the number of unpaired electrons.

As an example, consider the Fe ions in magnetite, Fe_3O_4. Since each oxygen atom takes two electrons from the iron, this means that there will be two ferric (Fe^{3+}) ions and one ferrous (Fe^{2+}) ion. From Table 2.1 we can see that the ferric ions have $3d^5$ configurations, so all of the electrons are unpaired. This means that their moment should be approximately 5 μ_B each. Since the ferrous ion ($3d^4$) has one set of paired electrons and four unpaired electrons, its moment is $4\mu_B$. The moments of the two ferric ions are antiparallel, so their net contribution is zero. This means that we would predict a total moment per formula unit of 4 μ_B, which is quite close to the measured value of 4.1 μ_B.

2.2 Magnetism in Solids

2.2.1 Magnetic Ordering

Magnetism in solids is an extremely rich field, and it is not very easy to find a simple way to discuss it. The properties of a magnetic sample are determined by effects that occur at different length scales, and the behavior at each length scale depends upon those below it.

The magnetic response of materials is classified into four major groups: *diamagnetic*, *paramagnetic*, *ferromagnetic*, and *antiferromagnetic*. Diamagnetic materials have no net atomic moment at zero field, and as a field is applied the induced moment opposes the applied field. For noble gases and insulators, this induced moment comes from the Larmor precession of the orbital electrons induced by the applied field.

The induced moment in diamagnetic metals comes from the motion of conduction band electrons. Some common diamagnetic materials include copper, silver, gold, Al_2O_3, SiO_2, H_2O, and most plastics and biological materials. All materials have a diamagnetic component due to the effect of the applied magnetic field upon the inner closed electron shells. The diamagnetic response is usually linear in applied field and temperature-independent.

Paramagnetic materials have a weak collinear response to an applied magnetic field. This stems from the presence of atoms or ions with unpaired electrons but the lack of long-range order. The unpaired electrons yield a magnetic moment, but the interaction of the moments is too weak to overcome the demagnetizing influence of thermal motion. In fact, it is the influence of thermal motion that defines paramagnetism. At low fields, the approximate susceptibility of paramagnetic materials is given by the Curie law.

$$\vec{M} = \chi_C \vec{H} \tag{2.4}$$

$$\chi_C = \frac{NM^2}{3kT} \tag{2.5}$$

Figure 2.1 shows a qualitative graph of this behavior. Curie paramagnetism is common to paramagnetic insulators and oxides, but it is separate from Pauli paramagnetism seen in paramagnetic metals and alloys and orbital paramagnetism seen in non-quenched oxides. Pauli paramagnetism is proportional to the density of states at the Fermi level, which is much less dependent upon the temperature. Orbital paramagnetism is also not particularly temperature dependent. A further discussion of paramagnetism and a derivation of the Curie law as a low-field limit of Langevin paramagnetism is included in Appendix A.

Ferromagnetism is the simplest ordered magnetic state. The unpaired electrons are present, as in paramagnetic materials, but in this case there are interactions between the moments that serve to align them even if there is no applied magnetic field. Figure 2.2a shows a simple schematic. The most common examples of these materials are the 3d intermetallics: cobalt, nickel, and iron.

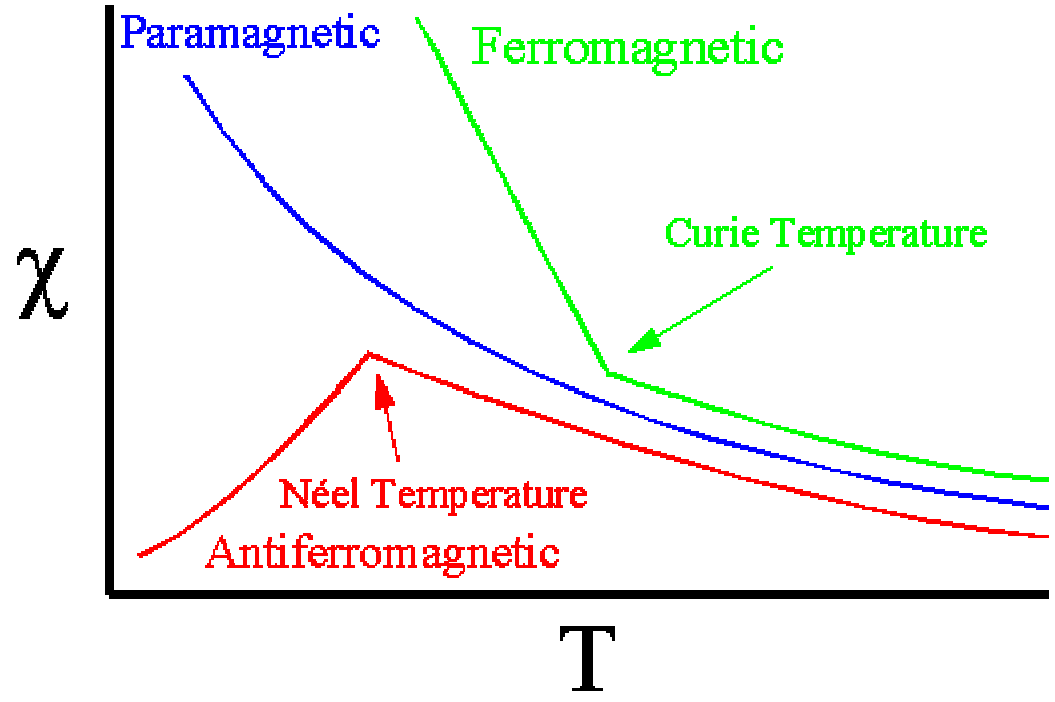

Figure 2.1: Magnetic susceptibilities for paramagnetic, ferromagnetic, and antiferromagnetic materials.

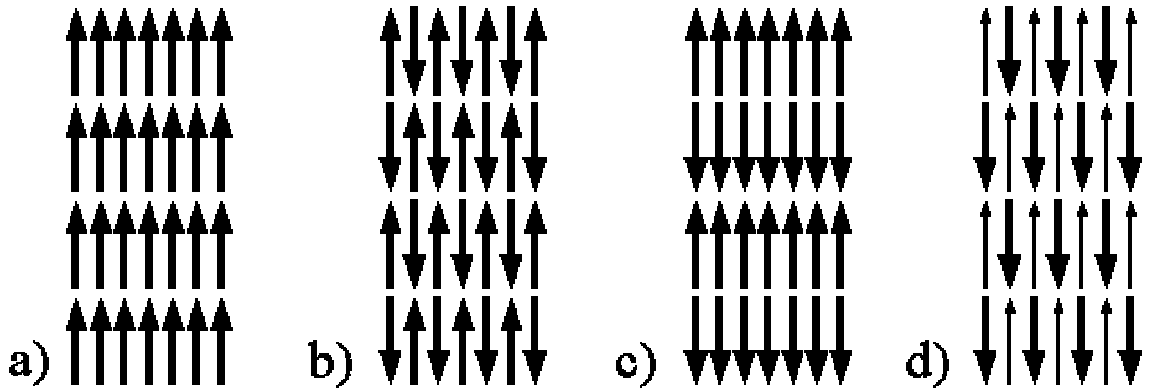

Figure 2.2: Simple magnetic structures - a) ferromagnetism b) and c) antiferromagnetism d) ferrimagnetism.

The interaction between local moments is strong in a ferromagnet, but it cannot counteract the disordering effects of temperature indefinitely. As the temperature is increased through the *Curie temperature* (T_C), the ordering is defeated and the material acts like a paramagnet. Above T_C, the susceptibility has the following *Curie-Weiss* form:

$$\chi = C/(T - T_C)$$

At T_C, the susceptibility diverges. The susceptibility below T_C is much more complicated and does not lend itself to simple analysis. It varies from material to material, sample to sample, and even experiment to experiment. The magnetic moment of the sample is a function not only of the applied magnetic field, but also of the past history of that sample.

This complex dependence upon past history is primarily due to the formation of magnetic domains, as shown in Fig. 2.3. The moments within each domain are ferromagnetically aligned, but the alignment between domains serves to minimize the total sample moment until a magnetic field is applied. As the field is initially applied, the net moment of the sample increases until all of the domains are aligned with the applied magnetic field. If the applied field is removed, the net magnetization will not vanish completely.

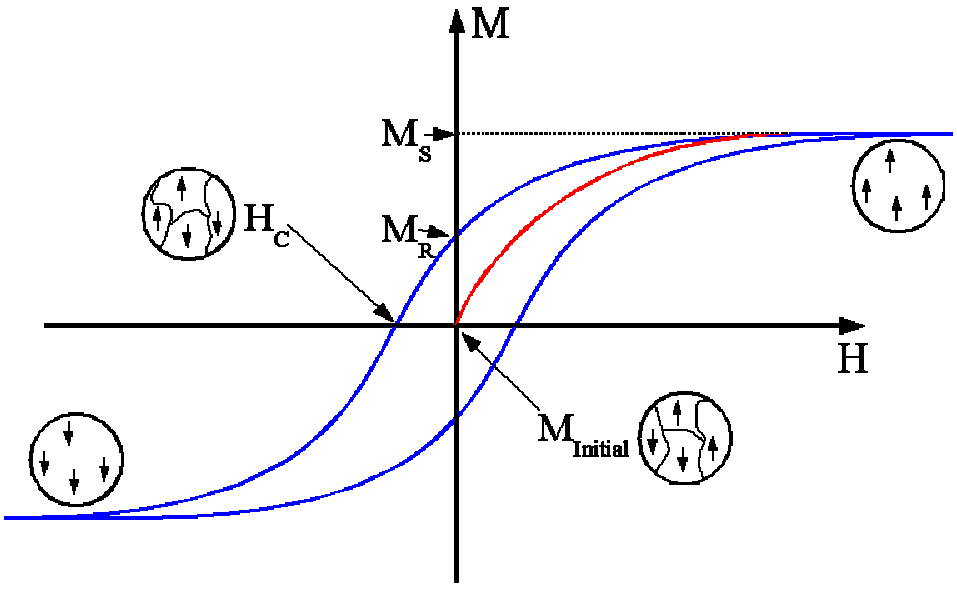

Figure 2.3: Hysteresis loop.

Instead, some of the processes of domain alignment (domain wall motion and domain rotation) are irreversible, and there will be a *remanent magnetization* (M_R). As the applied field is reversed, the net moment will again pass through zero at the *coercive field* point (H_C). If the process of sweeping the field is continued, eventually the graph of M(H) traces out a *hysteresis loop*. This loop contains information about the material that covers many length scales, from the microscopic interaction of individual moments to the micron-level behavior of domains to the overall size and shape of the sample.

Finally, the last major type of magnetic material is the antiferromagnet. In this case, the moments align such that the overall moment is zero. The easiest example is the antiparallel alignment of neighboring moments as shown in Fig. 2.2b. There are many other possible antiferromagnetic alignments, some of which will be discussed in later chapters. As with ferromagnets, the mechanism that causes the ordered alignment is strong, but it is still subject to the disordering effects of temperature. For the prototypical antiferromagnet the susceptibility versus temperature curve would resemble that shown in Fig. 2.1. Above the Néel temperature the behavior is paramagnetic. Below the Neel temperature the susceptibility decreases as the antiferromagnetic alignment increases. The susceptibility actually approaches zero for fields applied parallel to the ordering vector.

In addition to these simple magnetic subtypes, there are other more exotic types. If the magnitudes of the moments in an antiferromagnet are not equal, yielding a non-zero net magnetization, the compound is known as a *ferrimagnet*, as in Fig. 2.2d. There are also canted antiferromagnets, spin-density wave materials, spin glasses and many others.

2.2.2 Simple Exchange

The Heisenberg interaction Hamiltonian is often used to describe the interaction between individual moments in a magnetic material.

$$H = -\frac{1}{\hbar^2} J_{ij} \hat{S}_i \cdot \hat{S}_j \tag{2.6}$$

If J_{ij} is positive, the parallel alignment is favored, so the material is ferromagnetic. If Jij is negative, the result is an antiferromagnet. The Heisenberg Hamiltonian can be

used to model nearly any sort of interaction between spins, but it was originally put forth as a model for the direct exchange interaction.

Direct exchange can be viewed as a result of the Pauli exclusion principle. Consider two atoms which each have a single electron. As the two atoms are brought close enough that their orbitals interact and the electrons can move between them, the Pauli principle demands that the total wavefunction must be antisymmetric with respect to exchange of the electrons. Since the symmetry of the total wavefunction is a product of the spatial wavefunction and spin wavefunction, this means that one of them must be antisymmetric. An antisymmetric spatial wavefunction lowers the Coulomb energy of the system, which favors a ferromagnetic (symmetric) spin wavefunction. A more complete treatment of direct exchange can be found in Refs. [14, 15]

Indirect (or super-) exchange involves the interaction of spins when the ionic cores are separated by another ion such as O^{2-}, S^{2-}, Se^{2-}, Cl^{1-} or Br^{1-}. The 3d orbitals of the transition metal ion overlap with the p-orbitals of the oxygen. This overlap stabilizes an antiferromagnetic coupling between the 3d orbitals if the angle between the transition metal ions and the bridging oxygen is close to 180 degrees. As the angle decreases toward 90 degrees, the coupling becomes ferromagnetic. These are known as the *Goodenough-Kanamori* rules.

We can already see that the full microscopic description of magnetism in oxides is going to be quite involved. In section 2.4 the discussion will grow to include the double-exchange mechanism that is used to partially explain the colossal magnetoresistance effect in the manganites.

2.3 Magnetism in Small Particles

2.3.1 Superparamagnetism

When bulk magnetic materials are grown in confined dimensions, this can cause major changes in behavior that are not covered in the previous sections of this chapter. If the size of the system is comparable to one of the length scales of the magnetic coupling

at work in that system, then the behavior can be quite different from that of the bulk sample.

The first example is *superparamagnetism*, which emerges when the system is composed of small, independent crystals or crystallites. The atomic ordering of the crystallites is still preserved, so that the critical temperature for magnetic ordering is quite close to that of a bulk sample. However, since the particles are small, the direction of each moment is not rigidly confined. The crystalline anisotropy energy (also covered in references [14] and [15]) is reduced as the size of the crystallite decreases. Therefore, the net effect is that each crystallite moment is relatively free to move between any of the easy axes in response to an applied field, and thermal effects rapidly destabilize any overall moment in the sample as the applied field is removed. In other words, the sample starts to act a lot like the paramagnet listed in section 2.2.

There are marked differences, however. The regime of paramagnetic behavior extends from the Curie (or Néel) temperature down to the so-called *blocking temperature*. Below the blocking temperature, hysteresis reappears as the moment of each particle is no longer able to switch between easy axes. In a moment vs. temperature plot, the blocking temperature is seen as the point where the zero-field cooled curves and field-cooled curves diverge. The rigorous definition of a blocking temperature for any particular sample is somewhat difficult, since the onset of blocking depends upon the time scale of the measurement.

A general derivation goes something like this. Consider a small particle with a single domain and a single easy axis. If a magnetic field is applied to the particle at an angle θ to the easy axis, the energy is given as

$$F = E_a \sin^2 \theta \tag{2.7}$$

Where V is the particle volume and Ka is the anisotropy energy density. This energy barrier between the easy axis state and the aligned state can be overcome by thermal excitations with an expected time constant τ given by Arrhenius' Law.

$$\tau = \tau_0 \exp(\frac{\Delta E_a}{k_B T}) \tag{2.8}$$

ΔE_a is the difference in energy between the easy axis state and the aligned state.

$$\Delta E_a = K_a V (1 - \frac{H}{H_K})^2 \quad (2.9)$$

Where K_a is the anisotropy constant, V is the crystallite volume, and H_k is the anisotropy field, $H_k = 2K_a/Ms$, where M_s is the saturation magnetic moment.

Taking equations 2.3.1 and 2.3.2, we can see that the time constant for transitions between the two states is exponentially dependant upon the particle volume. For very small particles, the moment is relatively free to align with the applied field. In larger particles, τ diverges, implying that the particle moment will not spontaneously move away from the easy axis. Of course for a ferromagnetic particle, once a certain volume is reached, the overall alignment will break down as individual domains are formed.

Finally, the blocking temperature, T_B, can be estimated with the following equation:

$$T_B(H) = \frac{K_a V}{k_B \ln(\tau_m / \tau_0)} (1 - \frac{H}{H_K}) \quad (2.10)$$

Figure 2.4 shows an example of hysteresis loops taken above and below the blocking temperature for one of our hematite samples. Below the blocking temperature, the sample is clearly hysteretic with an open loop, and above the blocking temperature the sample is superparamagnetic.

2.3.2 Ferromagnetism in Small Antiferromagnet Particle

When antiferromagnetic compounds are prepared as small particles, either by initial growth or by grinding of bulk samples, it has been noted [16] that as the size of the particle decreases, a ferrimagnetic component to the total magnetization appears. This behavior has historically been explained through a number of mechanisms. Néel [1] suggested that uncompensated spins should appear at the surfaces of the particles. These uncompensated atomic spins would still be linked to the underlying order due to exchange interactions with neighboring atoms, but these interactions should be weakened by the lower coordination of surface atoms. In addition to surface uncompensated spins, there should be bulk uncompensated spins due to defects.

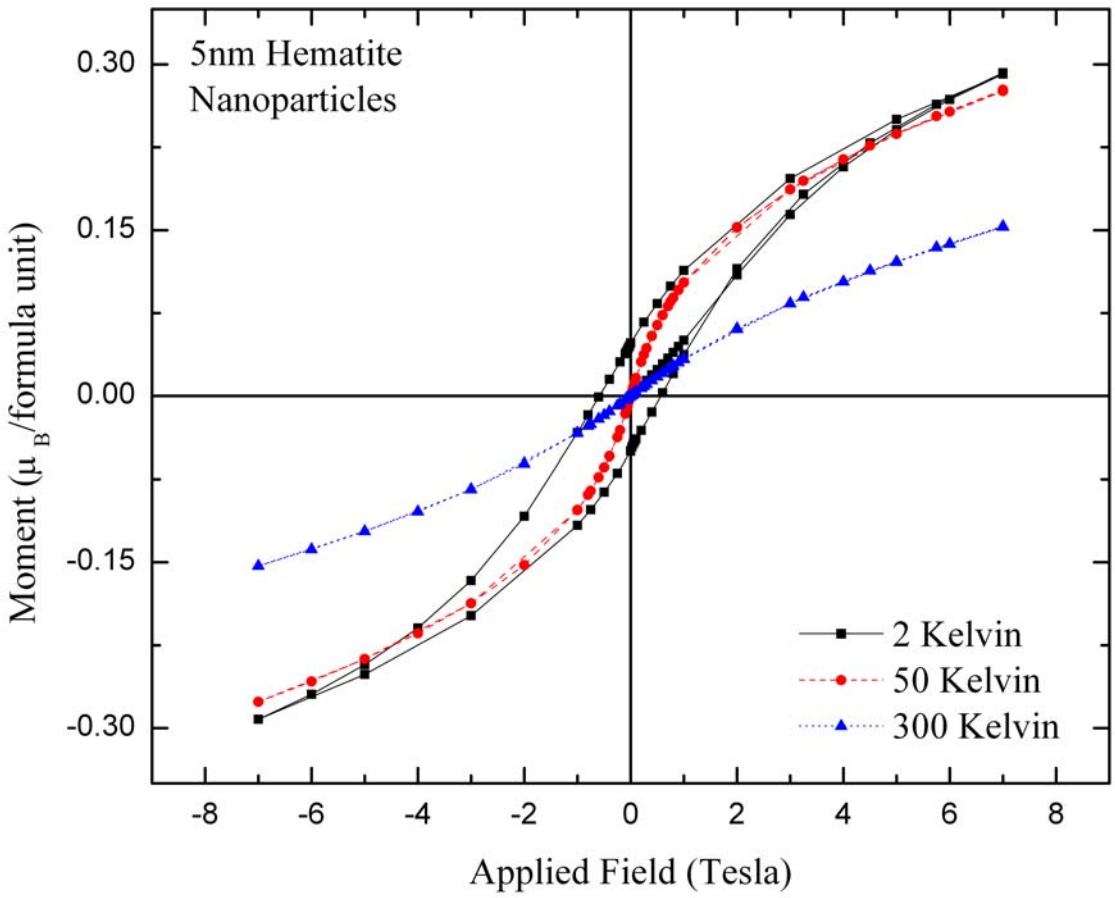

Figure 2.4: Example of evidence of blocking behavior. Note that the 2 Kelvin loop is open.

For all of the above cases, there should be a ferrimagnetic (or ferromagnetic) component added to the overall magnetic behavior of the system. This means that there are at least three different components contributing to the overall moment in antiferromagnetic particles. The first is the small diamagnetic component present in all materials. The second is the usual antiferromagnetic component, which was covered in Section 2.2. Finally, there is the ferrimagnetic component. Intuitively, the Curie temperature for the ferrimagnet should coincide with the Néel temperature for the antiferromagnet. If the exchange coupling between the bulk moments and the uncompensated moments is strong, we might expect that the ferrimagnetic moment should decrease with decreasing temperature, as in the antiferromagnet. If the exchange coupling is more complicated, then the behavior should be more akin to that of the ferromagnets, where the total moment increases as the temperature decreases. In the simplest approximation, the temperature dependence for the (sublattice) magnetization should be

$$M(T) = M_0(1 - BT^{\alpha}) \tag{2.11}$$

where α=3/2 for a ferromagnet and α=2 for an antiferromagnet.

In contrast to the above arguments, there have recently been several theoretical papers that propose a thermoinduced magnetic moment in antiferromagnetic nanoparticles. The first, by Morup et al [6, 7], is based on the asymmetry of spin wave excitations in nanoparticles.

Fig. 2.5 shows a schematic of a spin wave. The moments are no longer completely collinear, but instead each spin is slightly canted and precesses around the principle axis. The energy of the spin wave is determined by the wavelength, with long wavelength waves having the lowest energy. The lowest excitation is the uniform precession mode where all spins have the same angle and precess in phase with one another. This excitation has infinite wavelength and zero wavevector ($\mathbf{q}$=0). According to Morup, these low-lying uniform modes will be preferentially populated in nanoparticles. The wavevector is limited to values where $\mathbf{q}=n\pi/d$, where n is an integer and d is the diameter of the particle. Since the energy of the spin wave is proportional to q^2, then the energy of the nonzero wavevector spin waves increases rapidly. If the spin

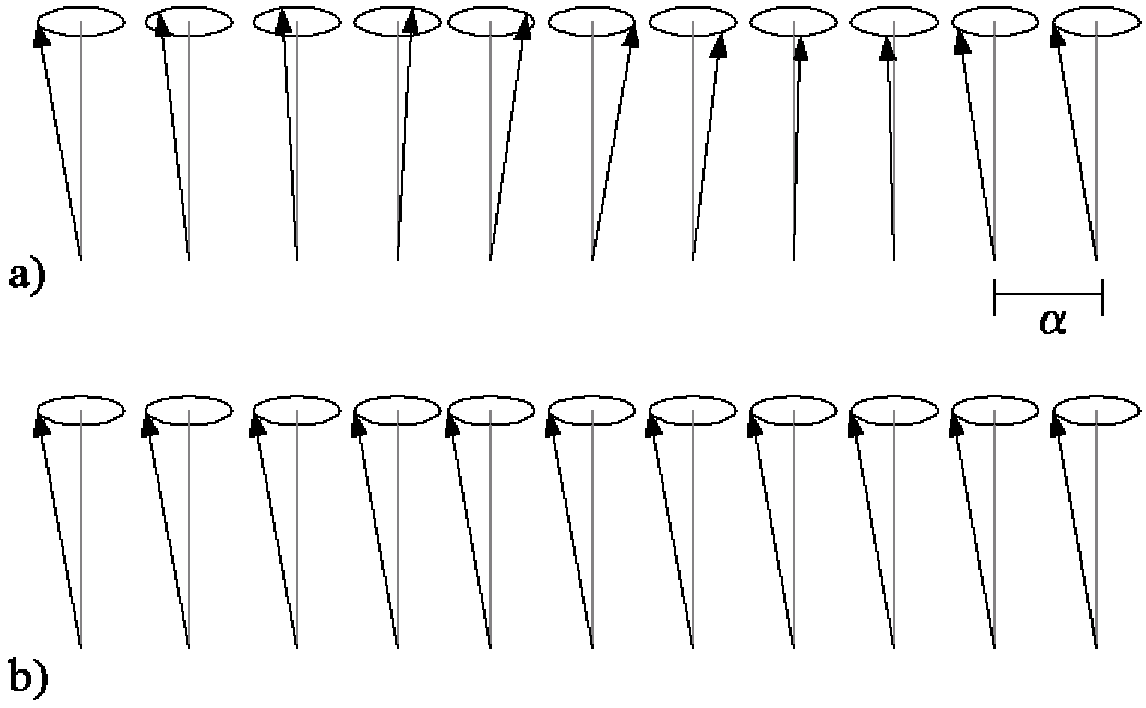

Figure 2.5: Spin wave excitations - a) $q = 2\pi/10\alpha$ b) q=0.

waves are only created through thermal excitations, then the population of q≠0 should rapidly decrease as temperature decreases. Note that the q=0 mode is the lowest energy mode in the spin wave spectrum, but the energy of the different excitations within the q=0 mode is determined by the canting angle.

The next important detail is the asymmetry in the canting angle for the two sublattices in the antiferromagnetic structure. Figure 2.6 shows a schematic of the two angles as they precess around the easy axis of magnetization. If the material is uniaxial, then the energy for the two angles is

$$E(\theta_{A,B}) = KV \sin^2 \theta_{A,B} \tag{2.12}$$

If there is no applied field, the symmetry is not spontaneously broken and the two angles are equal. If the angles are equal, their projections along the z-axis are also equal and there is no net moment. However, if an applied field is present, then the symmetry is broken. If the exchange field B_E is much larger than the anisotropy field $B_A \equiv K/M_S$, where M_S is the saturation magnetization, then the following approximation should be

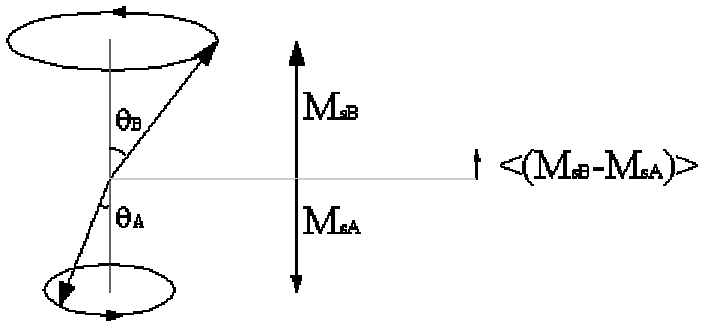

Figure 2.6: Anomalous moment from asymmetric spin wave excitation.

valid [6]

$$\frac{\sin\theta_A}{\sin\theta_B} \approx 1+\delta \tag{2.13}$$

where

$$\delta = \pm\sqrt{2\frac{B_A}{B_E}}\,. \tag{2.14}$$

Since the timescale of these precessions is quite rapid ($\omega_0 \sim 10^{12} s^{-1}$), the small asymmetry in the precession angle of the two sublattices will be evident as a small net magnetic moment. This should then lead to a thermal average moment of

$$\left\langle \left| \mu_{AF} \right| \right\rangle \cong 2g\mu_B \frac{k_B T}{\hbar\omega_0}. \tag{2.16}$$

Note that there is no volume dependence in the above expression. This is markedly different from the predictions of the Neel model. Note also that the moment *increases* linearly with temperature, reaching approximately $200\mu_B$ at 300 Kelvin.

The second thermoinduced magnetization idea is based upon Monte Carlo simulations of antiferromagnetic particles done by Brown et al.[2] Using a relatively simple Hamiltonian

$$H = -\sum_{<i,j>} J\hat{s}_i \cdot \hat{s}_j - \sum_i K(\hat{s}_i \cdot \hat{z})^2 \tag{2.15}$$

on a cube of Heisenberg (3-dimensional) spins, they observed a thermoinduced moment. As with most Monte Carlo simulations, the results are not easily stated in simple, closed form. However, they did make a number of predictions. First, the thermoinduced moment per spin increases as particle size decreases. Second, in the low temperature ($kT<<J$) regime, the net moment per particle *increases* linearly with temperature with approximately zero net moment at zero temperature. Third, the volume dependence of the susceptibility depends strongly on the anisotropy of the system, but for low anisotropies the volume dependence converges to the result published by Morup et al.

2.4 Complex Oxide Magnetism and Transport

2.4.1 History

As one might expect, the properties of multi-element oxides are more complex than those of simple oxides. There are many examples, from the high-temperature superconducting copper oxides to the colossal magnetoresistive cobaltites and manganites. This last example is the subject of the first two thirds of this dissertation.

The earliest hints of the complex physics of the manganites appear in the work of Jonker and van Santen in 1950.[17] They produced mixed crystals of $LaMnO_3$ doped with varying amounts of Ca, Sr or Ba substituted for La. Jonker and van Santen observed that these crystals form in the "perovskite" structure, as shown in Figure 2.7.

The A-site of the perovskite contains a large ion, such as La^{3+}, Ca^{2+}, or Sr^{2+}. The B-site contains the small ion, in this case Mn^{3+} or Mn^{4+}. The B-site ion is surrounded by an octahedral cage of O^{2-}. The undoped or "parent" compounds, such as $LaMnO_3$ and $CaMnO_3$, are all antiferromagnetic insulators. In the doped crystals, there were broad composition ranges where the crystals were ferromagnetic metals or semiconductors.

Van Santen and Jonker also measured the resistance of their crystals and published the results in a very short paper in 1950.[18] They noticed that the samples with the strongest ferromagnetism also had the lowest resistance. They also noticed anomalies in the data that occurred at the Curie temperature, but oddly enough they failed to measure the magnetoresistance. This was done a few years later by Volger.[19] He found substantial magnetoresistance, up to 15% at 77K as shown in Figure 2.8, but the

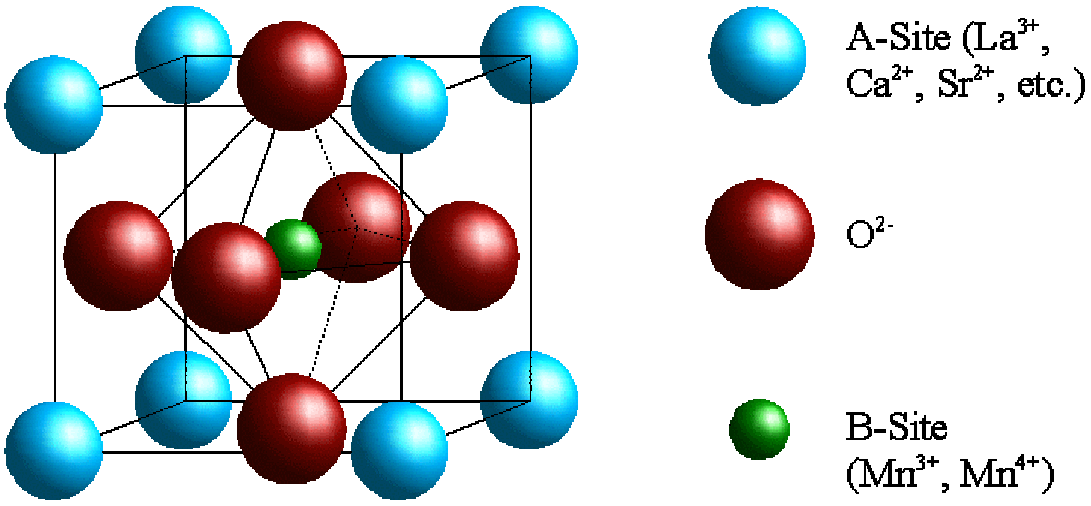

Figure 2.7: Perovskite structure.

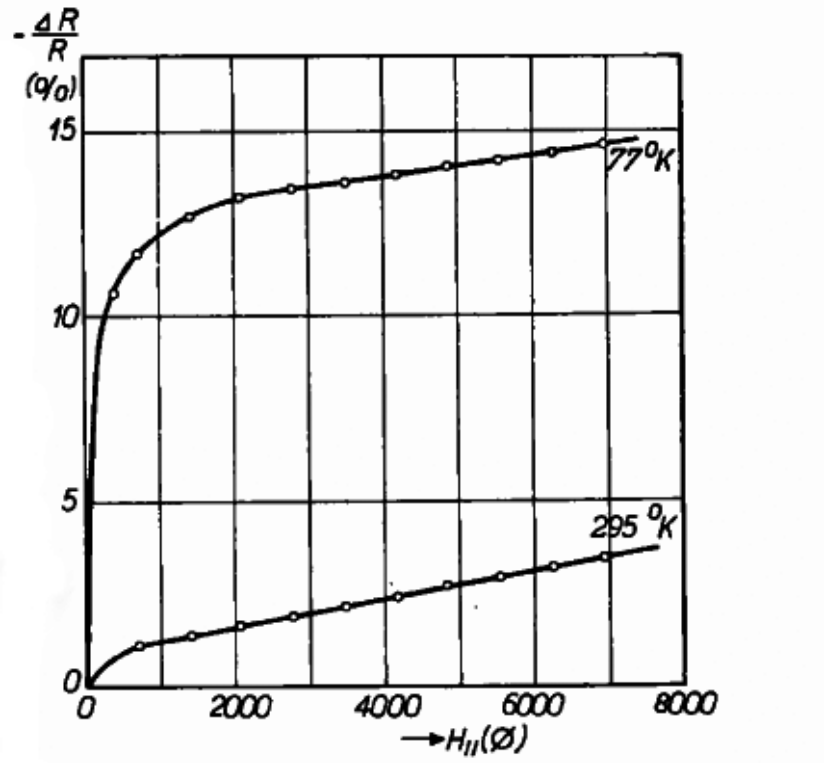

Figure 2.8: Change in resistance as a function of temperature for a long ceramic rod of $La_{0.7}Sr_{0.3}MnO_3$.

crystals were of comparatively poor quality and the magnetic fields were small.

During the next five years or so, many of the important theories were developed to explain these effects, with much of the work done by Zener in 1951. From February to July he published three papers [20-22]which explained the magnetic properties of the transition metals in terms of the behavior of the d-orbitals. In order to explain the earlier results of Jonker and van Santen, he postulated the existence of a "double exchange" mechanism, as will be discussed later. This double exchange was given substantial theoretical consideration for the next half-decade, with the work of Anderson and Hasegawa[23] serving as something of an end-marker. Important discoveries regarding the antiferromagnetic ordering structure of $La_{1-x}Ca_xMnO_3$ were made by Wollan and Koehler.[24] Interest in these oxides waned for the next several decades.

In the early 1990s, two research groups grew manganese oxide samples with magnetoresistance values that were larger than those of the "giant" magnetoresistance found in metallic multilayers.[25, 26] In 1994 Jin et al grew thin films with truly "colossal" magnetoresistance, with magnetoresistance values as high as ~100,000% at 77K.[27]

In the ensuing decade and a half the study of the transition metal oxides has exploded. The initial theories from the 1950s have proven to be only partially correct at best. There have been many corrections to the basic ideas, which will be presented shortly. More in depth explanations of the various theories can be found in any of the prominent review articles and monographs. These include several works by Dagotto[10, 28], Ramirez[29], and others[30, 31].

2.4.2 Double Exchange

The rich theoretical landscape comes from the novelty of the behavior of the manganites system. Most oxides are antiferromagnetic due to the *superexchange* interaction, as discussed in the previous section. The overlap of the metallic ion orbitals with those of the oxygen ions leads to antiferromagnetic ordering, but there is not enough overlap for any appreciable electron conduction to occur. In some cases the transition metal oxides are ferrimagnetic, as in many of the iron oxides.

True ferromagnetism is a relatively special case, mostly limited to the metallic systems dominated by direct exchange and some alloy systems where the *RKKY interaction* is important. In the case of RKKY exchange, the localized moments of a magnetic species in an alloy interact with the conduction electrons in the surrounding metal. The strength and sign of the RKKY interaction varies with distance, so it can cause ferromagnetic or antiferromagnetic ordering.

In the manganites, it was surprising to find a true ferromagnetic state in an oxide. This ferromagnetic state occurred while the resistance was relatively low and had a metallic temperature dependence.

All of the data pointed to a strong link between charge transport and ferromagnetic ordering. The foundation for much of our understanding of the manganites comes from Zener's proposal of a double-exchange mechanism that links conduction and magnetism in the manganites. Figure 2.9a is a simplified diagram of the effect. When a Ca^{2+} ion is substituted for a La^{3+} ion one of the Mn^{3+} must lose an electron and become Mn^{4+} in order to conserve charge. In the simplified diagram, if a Mn^{4+} and Mn^{3+} share a bridging oxygen ion, the extra electron can be transferred from the Mn^{3+} to the Mn^{4+} through the oxygen orbitals. The ferromagnetism occurs because the magnetic moment of the ion core is linked through a strong Hund's coupling to that of the moving electron,

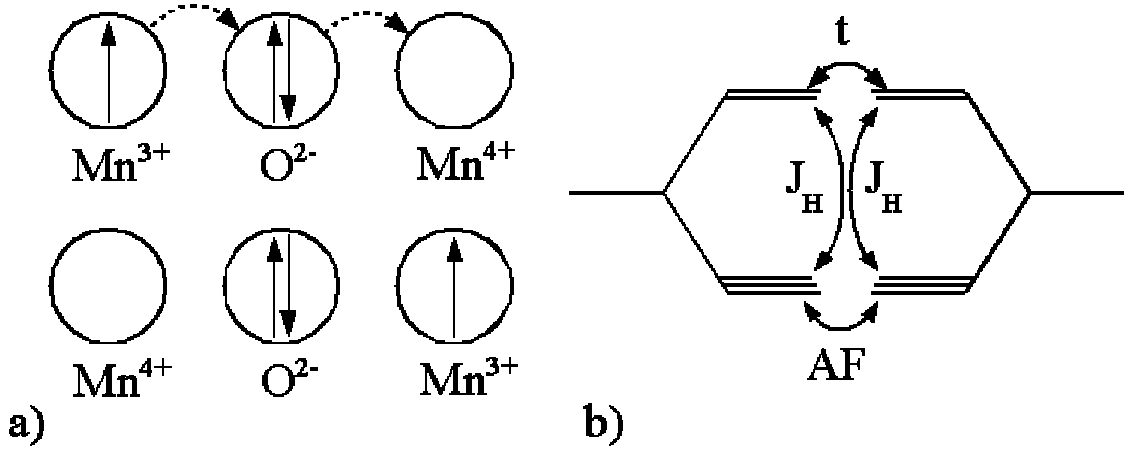

Figure 2.9: a) double exchange picture b) coupling terms in double-exchange interaction: t – hopping kinetic energy, J_H – Hund's rule coupling between e_g and t_{2g} electrons, AF – weak antiferromagnetic term from super-exchange between t_{2g} orbitals.

and the bandwidth of the moving electron is maximized when the moments of the ion cores are also aligned.

In more exact terms, the argument is as follows. In the Mn^{3+} ion, the d-band has four electrons. In a free atom, these levels are degenerate. Once the ion is placed in the oxygen octahedron, as in the perovskite structure, the degeneracy is lifted. For an unperturbed octahedron, the levels are split into a doublet and triplet, called the e_g and t_{2g} respectively, as shown in Figures 2.9b and 2.10. Dr. Dagotto includes an excellent derivation of this level splitting in Chapter 4.2 of his book[10].

The t_{2g} electrons are lower in energy and their orbitals have relatively little overlap with the surrounding oxygen orbitals. Therefore, they are immobile and contribute little to the conductivity of the sample. According to Hund's rules, the overall

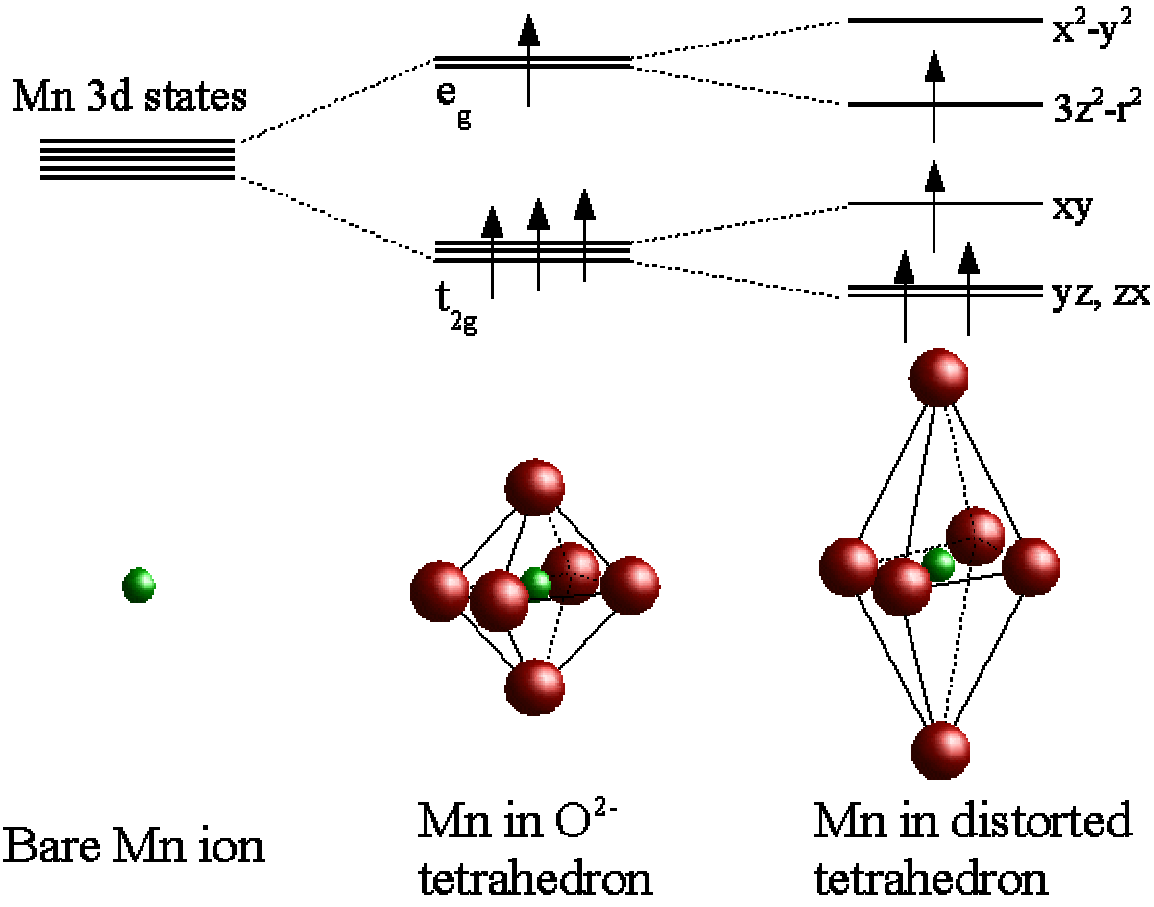

Figure 2.10: Jahn-Teller coupling of structure to electron energy levels.

spin of the electrons is maximized, which means that the total spin of the t_{2g} electrons is $3/2\mu_B$. The mobile e_g electron is also linked to the interior through the net spin maximization from Hund's rule, so during its residency on a specific ion, it is strongly energetically favorable for it to align with the t_{2g} electrons. In order to maximize the hopping amplitude, this means that the moments of the t_{2g} electrons of nearest-neighbor Mn atoms tend to align.

In Zener's original paper, his "double-exchange" argument used the analogy of a common ionic solid, NaCl. Imagine a $Na\text{-}Cl^{-}\text{-}Na^{+}$ system, where there is an extra electron on the first Na. This is degenerate with an equivalent system with the electron on the last Na. In terms of wave functions, it could be written as

$$\psi_1: \text{Na } Cl^{-}Na^{+}$$

$$\psi_2: Na^{+}Cl^{-}Na$$

Since ψ_1 and ψ_2 are degenerate, it is more useful to take the linear combinations:

$$\psi_{+} = \psi_1 + \psi_2$$

$$\psi_{-} = \psi_1 - \psi_2$$

These two combinations will differ in energy by 2ε. Therefore, the electron will oscillate between the two Na ions with a frequency $\nu=2\varepsilon/h$. Zener argued that it was this type of motion that would account for the conductivity of the manganite compounds. He also argued that, based on a semi-explicit continuation of the above arguments, that the actual mechanism of the electron transfer was the simultaneous transfer of an electron from the first Na atom to the Cl ion and another electron from the Cl ion to the Na ion. This is where the term "double-exchange" originates. Oddly enough, this argument makes no explicit reference to spin alignment. It was only realized later that this mechanism would align the spins, as detailed above. In the ensuing decades, the idea of a simultaneous double transfer of electrons has fallen out of favor, but the "double-exchange" terminology is still used. It is also sometimes called "Zener ferromagnetism."

After Zener's original work, Anderson and Hasegawa studied the mechanism in more detail. The most important consequence of their work is the explicit statement of the effective hopping term, $t_{eff} = t \cos(\theta/2)$, where θ is the angle between the core t_{2g} spins of two Mn ions sharing a common oxygen. Thus, the carrier mobility (electron or

hole) is maximized when the t_{2g} spins are aligned. If an applied magnetic field is strong enough to align the Mn ions, then the conductivity should increase.

These simple arguments gave a qualitative explanation for the ferromagnetic regimes in most of the manganites oxides, but they have dramatic failings. They do not predict any of the more exotic phases, such as charge-ordered, orbital-ordered, antiferromagnetic, or ferromagnetic insulating. The greatest sin of the "double-exchange" framework is that it was not able to predict the colossal magnetoresistance seen in the manganites. The cosine in the effective hopping term predicts a change in resistance as a function of field of approximately 30%, but it is impossible to get a 100,000% change in resistance from a simple cosine term.

Of course, the fifty years since the original statement of the double-exchange interaction have allowed for many expansions of the theory. The double exchange interaction is a good starting point, but there are many other elements necessary for a full understanding of the manganites.

On the ionic level, there are still several more terms that would have to be part of any realistic description. According to Reference [28], a good starting Hamiltonian would contain the following:

$$H = H_{kin} + H_{Hund} + H_{AFM} + H_{el-ph} + H_{el-el} \tag{2.16}$$

The H_{kin} and H_{Hund} terms contain the important elements of the double-exchange interaction and basically allow ferromagnetic ordering.

The H_{AFM} term comes from super-exchange. The Goodenough-Kanamori rules summarizing the super-exchange interaction in Section 2.2 should still be valid in the manganites. This means that there is an antiferromagnetic term that can be important, depending upon the orientation of the manganese orbitals and the e_g electron density. In general treatments, this is considered to be the weakest interaction.

$H_{el\text{-}ph}$ contains the interactions between the e_g electrons and the lattice, or more accurately, between the e_g electrons and the MnO_6 octahedra. Figure 2.10 shows how the energy of the e_g electron can be lowered by the distortion of the octahedron along the z-axis. These *Jahn-Teller* distortions can be static or dynamic.

Finally, $H_{el\text{-}el}$ would contain the Coulomb repulsion between the e_g electrons. As is usually the case, there would be some screening of the bare charge of the electron due to the surrounding lattice. This term is the strongest, but its primary effect is forbidding double-occupancy of e_g electrons on a single site.

Even though it is relatively easy to state a fairly complete model Hamiltonian, it is essentially unsolvable without significant simplification. The various tweaks and modifications necessary to produce a tractable answer have filled the literature. However, the many advances in atomic-level understanding have still not been able to completely explain the colossal magnetoresistance effect. There is a growing body of evidence that an important missing piece is phase separation, as is discussed in the next section.

2.4.3 Phase Separation

The role of phase separation in colossal magnetoresistance is still a matter of considerable interest. There have been both direct and indirect observations of regions with different magnetic or conductive properties occurring simultaneously in a sample that is relatively far removed from a global phase transition. For example, an $La_{1-x-y}Pr_yCa_xMnO_3$ (LPCMO) sample might be at a certain temperature and field where the global behavior might be ferromagnetic and metallic, but there are substantial charge-ordered antiferromagnetic insulating regions. The results in Section 4.2 hint at such behavior.

Figures 2.11 and 2.12 show two famous examples of direct observation of phase separation. These offer indisputable proof that, at least in those particular samples, there are separate regions with different conductivities even below the Curie temperature. Fig 2.11 shows a long length-scale phase separation between conducting and insulating regions in $La_{1-x-y}Pr_yCa_xMnO_3$ observed using transmission electron microscopy

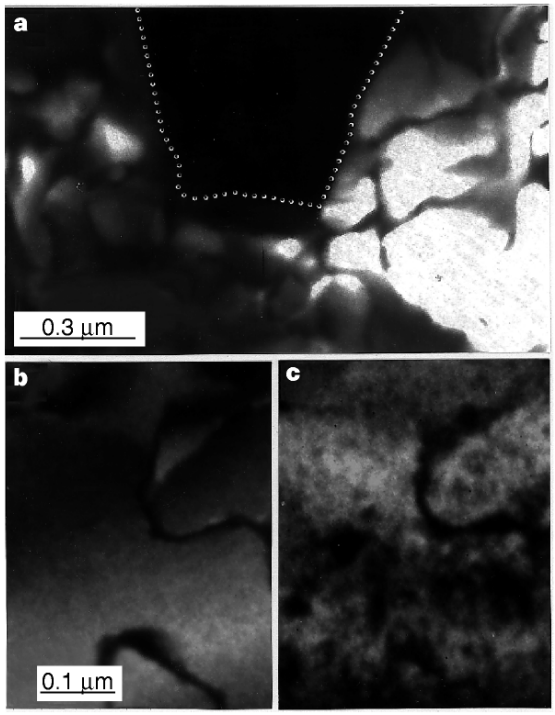

Figure 2.11: Sub-micron phase separation in LPCMO. Reprinted with permission from [32]. Copyright 1999 by the Nature Publishing Group.

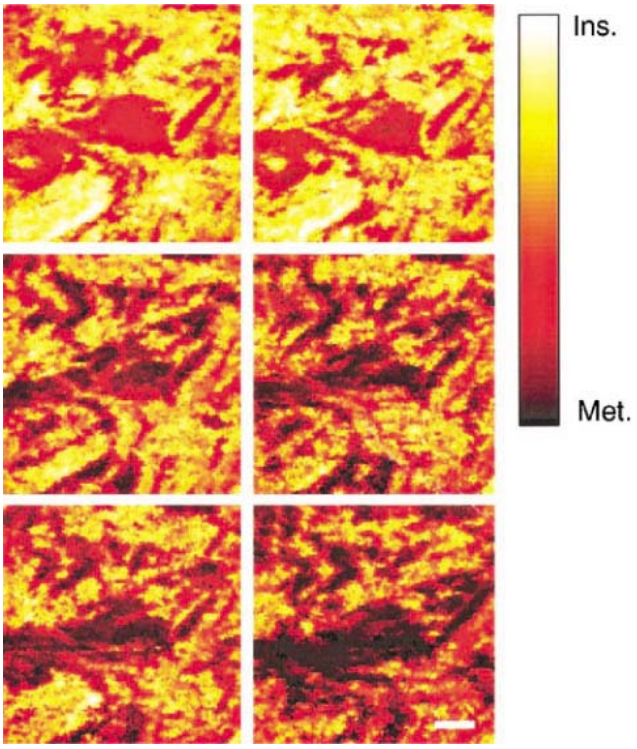

Figure 2.12: Nanometer-scale phase separation in LCMO. Reprinted with permission from [33]. Copyright 1999 by The American Academy for the Advancement of Science.

(TEM)[32]. The images in Fig 2.12 were obtained using scanning tunneling spectroscopy (STS) on $La_{1-x}Ca_xMnO_3$, which means that the image shows the local conductivity at every pixel[33]. The separate regions are much smaller than those observed by Uehara in LPCMO. However, these images show a stronger link between magnetism and transport, as the applied magnetic field increases the size of the metallic domains at the expense of the insulating domains.

There are also many other experimental methods which imply that something akin to phase separation is occurring. Nuclear magnetic resonance experiments [34] have shown the simultaneous coexistence of ferromagnetic and antiferromagnetic regions in $La_{1-x}Ca_xMnO_3$. An anomalous diffusive peak observed at zero energy in elastic neutron scattering experiments is consistent with phase coexistence.[35] Optical conductivity, X-ray scattering, and heat capacity measurements summarized in [10] have also shown some evidence of separate phases.

With so much evidence, both direct and circumstantial, the question is no longer *whether* phase separation occurs in the manganites, but *how* and *why* it occurs and *what role* it plays in colossal magnetoresistance.

The answer to *what role* phase separation plays in magnetoresistance is the easiest to address. One of the long-standing issues with the double-exchange model is that it does not make accurate predictions about the size of the colossal magnetoresistance effect. However, if there are multiple phases in a given sample, it is much easier to see how a large change in resistance can occur with only a small change in applied field or temperature. The answer is *percolation*. As the volume and number of metallic regions in an insulating sample increases, the DC resistance is largely unchanged until a critical concentration is reached, after which the resistance decreases rapidly.

The subject of percolation theory is far broader than can be presented in this work. More thorough treatments are available in Refs [10, 36]. However, there are a number of important results from the literature that can be stated relatively quickly.

First, the critical concentration ($p_c \equiv$ conducting sites / total sites) necessary for percolation decreases as the dimensionality of the problem increases. Simulations have been performed for many different model system configurations from one-dimensional

chains to 3-dimensional lattices, and the critical concentration (p_c) necessary for percolative transport decreases from $p_c = 1$ (all links conducting) for a 1D chain to $p_c = 0.5$ for a 2D square lattice to $p_c \sim 0.25$ for a 3D cubic lattice.

Second, at the critical concentration the percolating pathway seems to become *scale-free*. This means that the size of the percolating pathway diverges rapidly, and there is roughness on many length scales. In this sense, the percolating pathway has a fractal nature, and this is the reason for the swift increase in conductivity. At conductivity onset, the first pathway is likely to be long and convoluted with many thin sections. As the number of conduction sites increases, the pathway gets shorter and wider very rapidly.

The deeper questions of *how* and *why* large-scale phase separation should occur in the manganites are much more controversial. Due to the different carrier concentrations in CO and FM regimes, the coexistence of large domains is not favored due to Coulomb repulsion. According to the view championed by Dagotto[10], the large scale phase separation is a result of "quenched disorder." This means that the short-scale electronic phase separation is disrupted on a local level by the disorder inherent in the doped manganite compounds. Even the variation of the A-site atoms in $La_{1-x}Ca_xMnO_3$ should be sufficient to create trapping centers for the mobile e_g electrons. In $La_{1-x-y}Pr_yCa_xMnO_3$ the additional disorder from the size difference between La and Pr ions should also change the local phase structure. A simple schematic of this idea would look something like Figure 2.13.

More advanced simulations have been performed by many researchers. It is not practical to incorporate all of the known features of the manganites into a single model that is tractable without unlimited computer resources. Even so, simpler "toy models" can yield serviceable results.

For instance, in a paper by Burgy et al[36], a simple "toy model" Monte Carlo simulation was done with a very simple Ising-type Hamiltonian. After the Monte Carlo simulation was finished, the resulting map of spins was translated into the FM/CO framework and the equivalent resistance was calculated. Figure 2.14 shows the results of this simulation. Note that 2.14b and 2.14c both bear a strong resemblance to the behavior

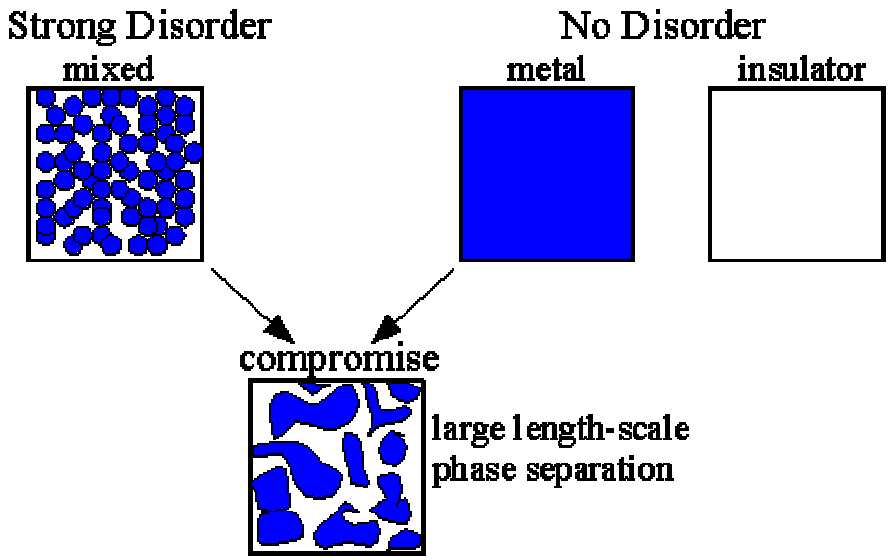

Figure 2.13: Schematic of "quenched disorder" mechanism.

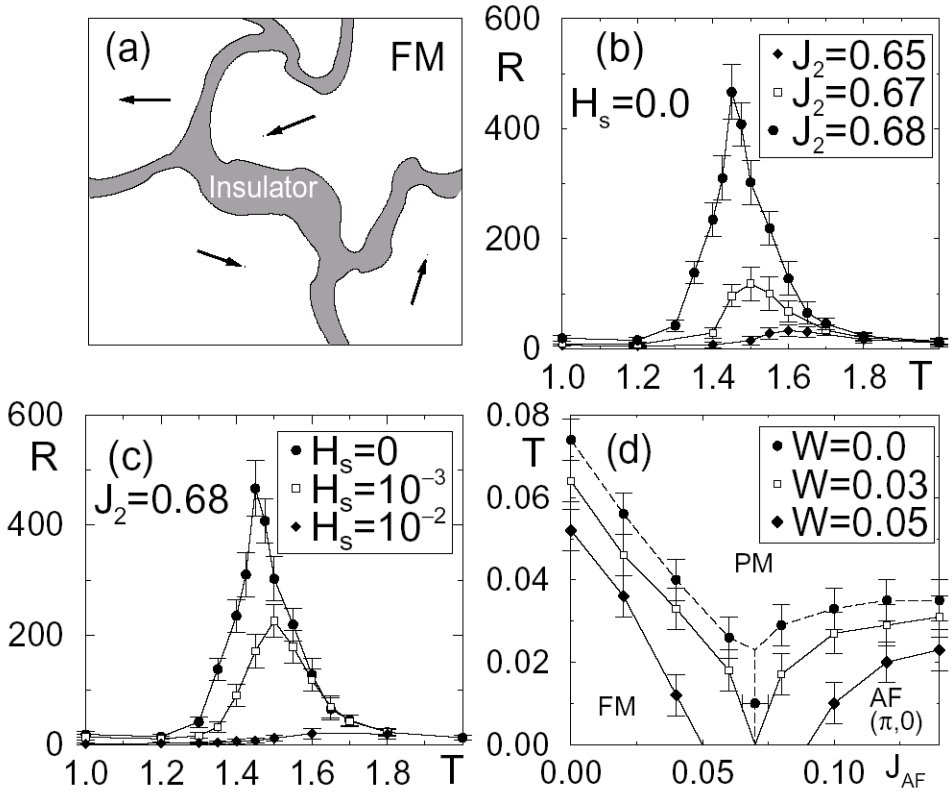

Figure 2.14: (a) Schematic of phase separation in model. (b) resistance of toy network at zero applied field with variable Ising coupling J2. (c) resistance of toy model with variable applied field HS. (d) Phase diagram of model system. Reprinted with permission from [36]. Copyright 2001 by the American Physical Society.

of CMR manganites. At high temperatures, the resistance is relatively low. As the temperature decreases, the resistance increases rapidly, peaks, and then decreases to a level lower than that of the high temperature phase. 2.14d gives the resulting phase diagram for their model system as a function of the Ising coupling strength (J_{AF}) and disorder level (W).

Another major theory, as set forth by K. Ahn et al[9], holds that the effects of strain are more important to large-scale phase separation. It is already quite clear that there is a strong electron-lattice coupling in the manganites, as shown in Figure 2.10. In their work, they were able to create phase separation in their model without resorting to any parameters beyond the strength of the electron-lattice coupling. The local density of states (DOS) was calculated for each type of region, and a gap in the density of states was observed for the distorted regions, as shown in Figure 2.15. The phase separation is entirely spontaneous and not dependent upon disorder.

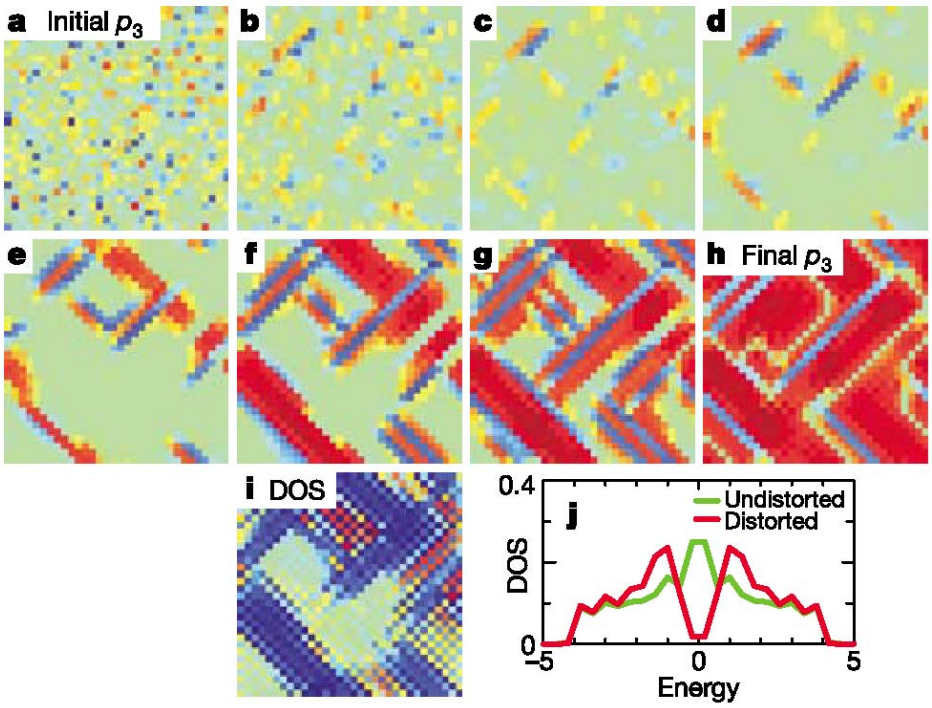

Figure 2.15: Results of the simulations performed by K. Ahn. Pictures a - h represent a time sequence in the simulation. Picture i is the local density of states generated for f. j represents typical DOS for both distorted and undistorted regions with a small "pseudogap" visible for the distorted regions. Reprinted from [9] with permission. Copyright 1999 by the Nature Publishing Group.

Chapter 3 Experimental Methods

3.1 Sample Growth

3.1.1 Thin Film Growth

One of the primary issues in studying the characteristics of the transition metal oxides is the growth of clean, well-structured samples. Using solution-based methods, it is possible to grow and characterize nanostructures of simple oxides of transition metals. This includes the various phases of iron oxide discussed in later sections of this chapter.

However, it is not so simple to grow nanostructured samples of more complex oxides. If we want to test the behavior of complex materials in reduced dimensionalities, then a good way to start is by growing them as a thin film. For our purposes, laser molecular beam epitaxy is the best way to grow transition metal oxide thin films. Laser MBE is essentially a sub-category of the larger technique of pulsed laser deposition. Pulsed laser deposition occurs when a powerful pulsed laser is used to ablate a plume of material from a target so that the material is deposited on a substrate. See Figure 3.1 for a simple schematic, and see Reference [37] for a detailed review of the key details in the pulsed laser deposition process.

Laser MBE is a more carefully controlled version of pulsed laser deposition. The schematic is the same, but the deposition occurs in a vacuum chamber with a base pressure lower than $1x10^{-10}$ torr, and the process parameters are chosen such that the film grows epitaxially on the substrate. A Reflection High Energy Electron Diffraction (RHEED) system is used to monitor the growth during deposition. The intensity of the diffraction spots on the RHEED screen is monitored. Under optimal growth conditions, the intensity oscillates with a period of one monolayer.

The targets are composed of compressed, annealed powders prepared with the proper ratios of the necessary elements. The growth chamber contains a target carousel, which will allow for oxide heterostructures to be grown. The targets are degassed after they are inserted into the chamber. The sample substrate is mounted on a specially designed sample holder, which is placed directly above the target. The sample holder and

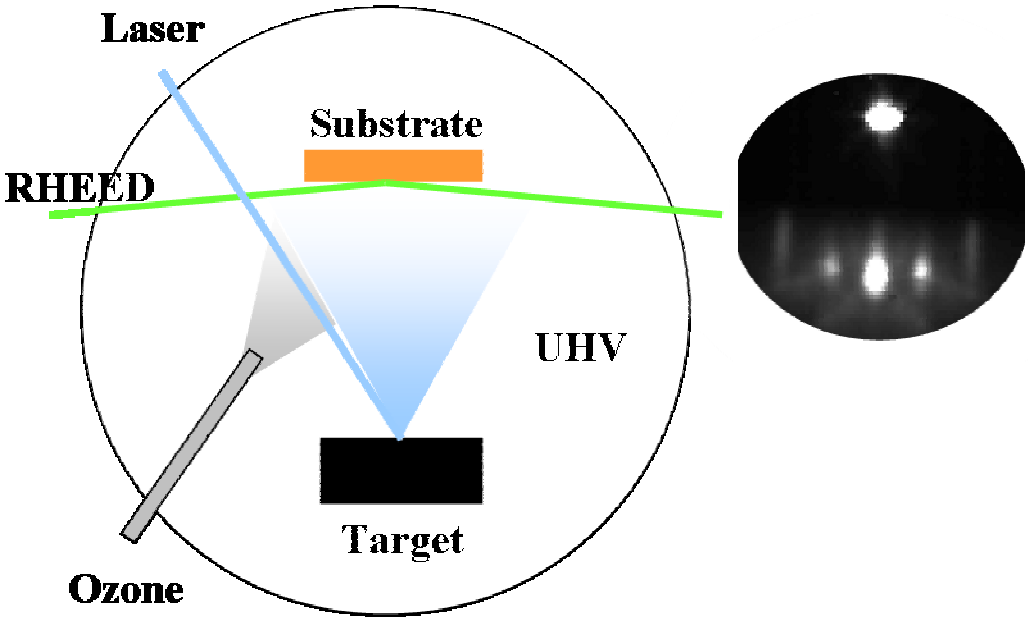

Figure 3.1: Laser Molecular Beam Epitaxy schematic.

heater assembly are shown in Figure 3.2. The bottom plate is a standard molybdenum sample holder. The tantalum heater wire is encased in a UHV compatible, high temperature ceramic called Ceramabond 569 produced by Aremco Products. It is actually not trivial to find vacuum-compatible components that are capable of withstanding the high temperatures and oxidizing atmosphere during the deposition process. The top stainless steel faceplate holds the substrate(s) in direct contact with the heater during the deposition. The temperature of the substrate is measured using an infrared thermometer outside the chamber.

A small gas feedthrough projects into the sample space, with the end of the tube mounted as close to the sample as possible without interfering with the deposition plume. During deposition, this tube is used to flood oxygen (8% ozone) into the chamber, so that the local environment of the sample is oxygen-rich. This is used to correct for the oxygen depletion that tends to occur when transition metal oxides are heated in a vacuum. Even with this local enhancement, the films are somewhat oxygen deficient.

The sample is annealed *in situ* with flowing oxygen, and then allowed to cool. If no *in situ* techniques are going to be used, then the sample is removed and re-annealed in flowing oxygen at atmospheric pressure in order to fill all of the oxygen vacancies.

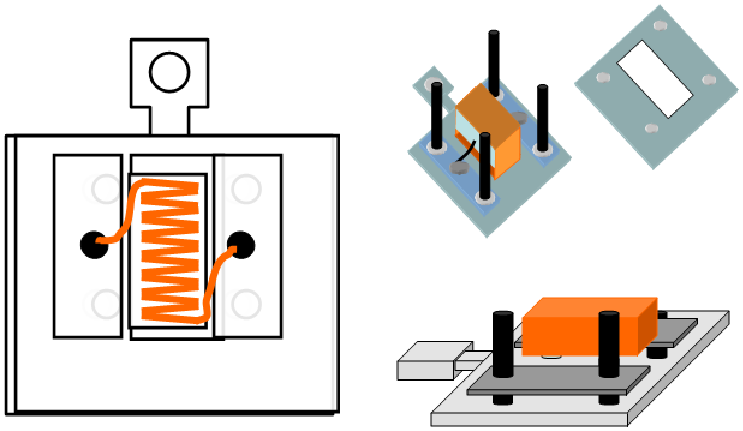

Figure 3.2: Sample heater assembly.

Samples grown using the procedure listed above are generally quite satisfactory with good stoichiometry and epitaxy. The only real issue with laser-MBE samples is the tendency for droplet formation on the sample surface. A particularly bad example is shown in Fig. 3.3. These droplets are usually the result of inhomogeneous local heating in the target, which allows some of the target material to be ejected in droplet form rather than as neutral atoms or ions. With careful target preparation and operator control during growth, the density of these droplets can be minimized but they can never be completely eliminated. Figure 3.4 shows a particularly good example with no visible droplets.

Following the deposition, x-ray diffraction and atomic force microscopy are performed on the sample. X-ray diffraction gives such vital information as the crystallinity and epitaxy of the sample. If one of the more advanced diffractometers is used, it is also possible to analyze the epitaxial strain in the sample

3.1.2 Nanoparticle Growth

The hematite nanoparticles were grown using a forced hydrolysis process.[38] An aqueous solution of $FeCl_3$ and HCl is prepared and then aged at elevated temperature for tens of hours, and then quenched to room temperature. The particle suspension is then put into a semipermeable membrane bag and dialyzed with deionized water. The water is changed once a day until no Fe^{3+} and Cl^- ions can be detected in the dialyzite. The final particle size is determined by the initial concentration of $FeCl_3$, with higher

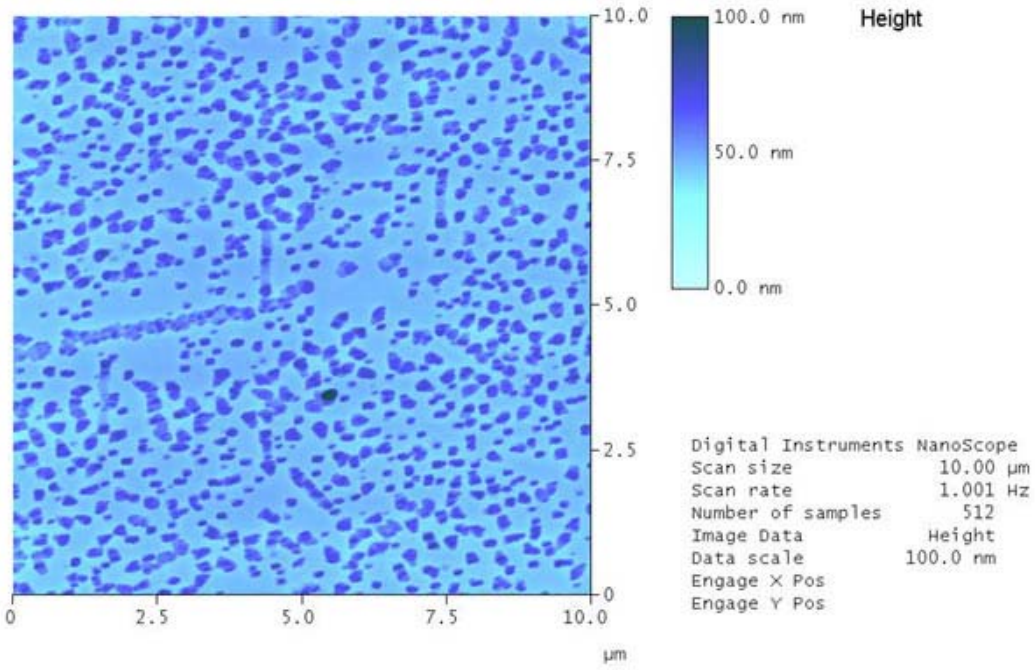

Figure 3.3: Example of poor surface morphology.

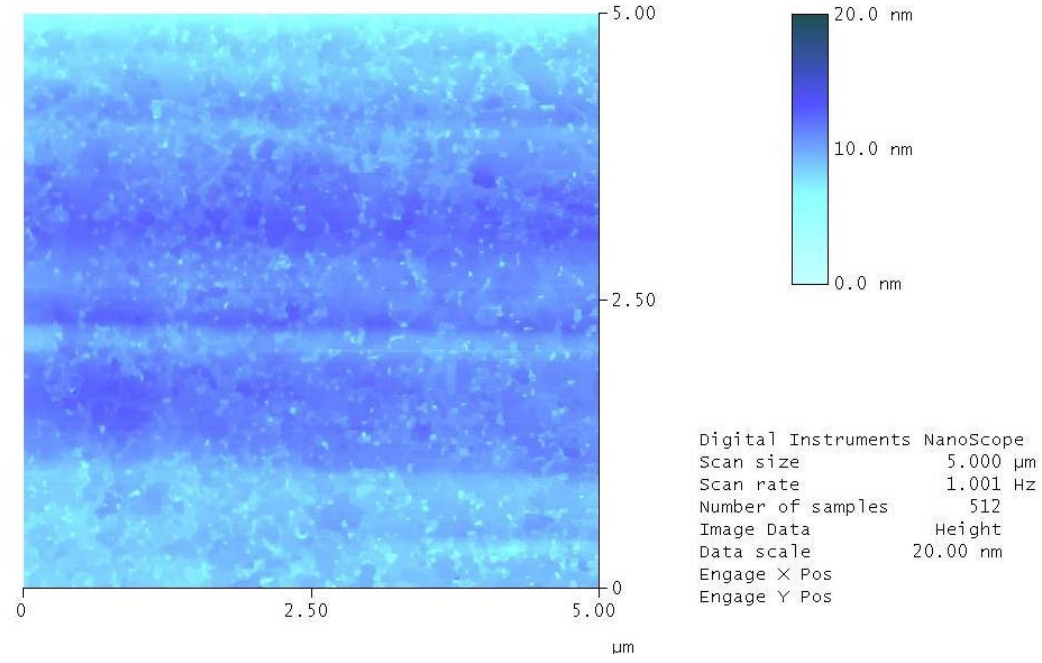

Figure 3.4: No visible droplets.

initial concentrations yielding larger particles. The amount of aging determines the number and quality of the resulting crystallites. The particles are believed to pass through an unstable β-FeOOH stage during aging. The unstable equilibrium between free Fe ions and β-FeOOH particles seems to be a key reason that the resulting particles are quite uniform in size. For improved size-selection, it is also possible to centrifuge the resulting suspension and pour off the smallest particles.

3.2 Microscopy

Since the samples in these experiments come in many different sizes and shapes, I have had to use many different types of microscopy. Optical microscopy is always the easiest and cheapest, but the ultimate resolution for the very best optical microscopes is not much smaller than one micron, and for most microscopes it is difficult to even approach that limit.

The next best solution is *scanning electron microscopy* (SEM). The SEM works by scanning a collimated beam of medium-energy electrons across the sample, and then detecting the emitted electrons, as shown in the schematic in Figure 3.5a.

With beam energies from 0.1 – 50 kV, the electron wavelength varies from 1.2 Å – 0.05 Å. In theory, this means that the resolution of the microscope should be on the order of the electron wavelength. In practice, the resolution is much worse than this. As the incident electrons penetrate and scatter within the sample, they fill what is known as the *interaction volume*, as shown in Figure 3.6. Some of the incident electrons scatter elastically from the nuclear cores of the sample atoms and are reflected back out of the sample. The rest of the incident electrons lose energy through inelastic collisions with the orbital electrons in the sample. Some of these inelastic events produce *secondary electrons* which leave the sample and are collected in the electron detector, forming the bulk of the detected electrons in most scanning geometries.

Since these secondary electrons are low energy (3-5eV), they have a relatively shallow escape depth. It is for this reason that they yield the highest resolution images. As the electron beam sweeps across the sample, the detector collects all of the electrons produced at a given instant. Secondary electrons are produced throughout the entire

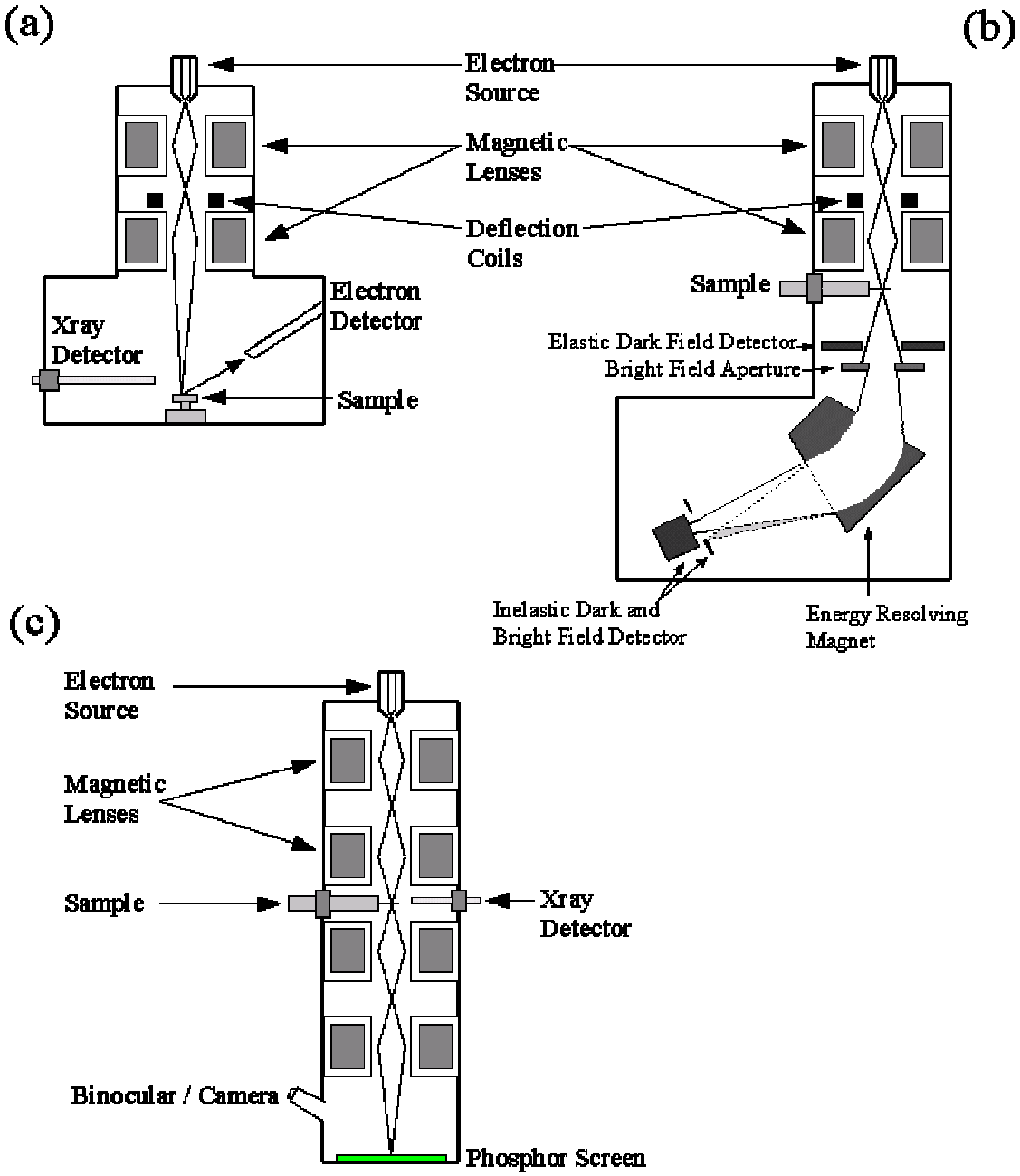

Figure 3.5: Electron microscopes - a) Scanning Electron Micrsocope b) Scanning Transmission Electron Microscope c) Transmission Electron Microscope.

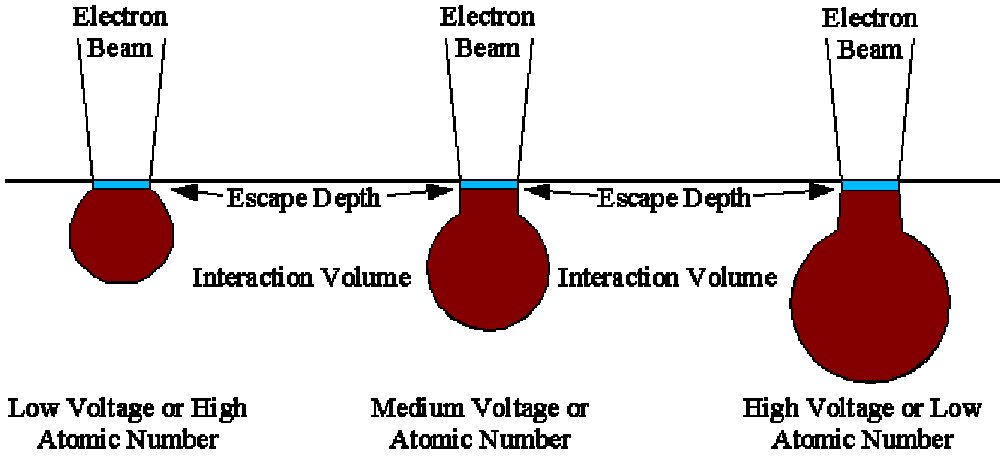

Figure 3.6: Interaction volume and escape depth as a function of accelerating voltage and atomic number.

interaction volume, but only the electrons produced close to the surface are able to escape. This means that the detected electrons originate from a relatively small volume, which yields the highest resolution images.

Some of the electrons undergo a number of elastic scattering events and leave the sample with their energy unchanged. They are called *backscattered electrons*. The number of backscattered electrons that are produced depends heavily on the atomic number of the atoms within the interaction volume. An image formed from the backscattered electrons will then show the differences in atomic number as changes in contrast, even if the topography of the sample is unchanged. Since the electrons emerge from the entire interaction volume, the resolution of backscattered electron images is not as high as for secondary electron images. The Hitachi S-4700 used in our experiments has detectors for both types of electrons. Its rated maximum resolution is 1.5nm, but we were never able to achieve that in practice since most of our samples are poor conductors and therefore the images are distorted due to charging effects.

The SEM also has several other benefits. Due to the geometry of the electron beam and aperture system on most SEMs, the depth of field in most images is quite long. This means that for samples with high aspect ratios, like patterned samples and nanocrystals, the foreground and background are both in focus.

Another substantial benefit of the Hitachi S-4700 is that it has an attached X ray detector for energy-dispersive spectroscopy (EDS). When the incident electron knocks loose one of the inner orbital electrons from an atom in the sample, an electron from a higher orbital can fill the resulting hole through the emission of an X ray. Since both the initial and final orbital energies are element-specific, the resulting X ray will have a characteristic energy. With proper detection equipment and software, the energy spectrum can then give an estimate of the chemical makeup of the sample. Extrinsic factors can cause changes in the indicated composition of the sample, so the results should always be compared with those from other techniques.

I have also used *Transmission Electron Microscopy* (TEM) during my research. In TEM, the electron beam is not scanned, but instead shines through the sample and is collected by electron optics onto the detection screen, as shown in Figure 3.5c. The accelerating voltage is much higher, so the electron wavelength is shorter. This increases the resolution, compared to the SEM. With accelerating voltages from 20keV to 1MeV, the resolution ranges from 4 to 1Å. Since the TEM uses transmitted electrons for imaging, it can only be used on extremely thin samples or for particles suspended on imaging grids. For thicker samples a higher voltage TEM or scanning transmission electron microscope (STEM) is required. The sample thickness for a conventional TEM can be as large as 100 – 120nm. As the accelerating voltage of the microscope increases, the sample thickness can increase to as high as 1 mm for a 1 MeV microscope. Most TEMs also have the capability to perform Xray spectroscopy, with the added benefit of increased accuracy due to the lack of a substrate.

Finally, I have also used Atomic Force Microscopy (AFM) and Scanning Tunneling Microscopy (STM). These are two of the most prominent examples of the broader class of scanning probe microscopies. This large class of microscopies got their start with the invention of the STM by Binnig and Rohrer in 1981, although a precursor instrument called the “topografiner” was created in the early Seventies by Russell Young.

All scanning probe microscopes have a number of common features. First, they all utilize a sharp tip, which is scanned across the surface of interest. Second, the

interaction between the tip and surface is measured, which provides the information necessary to create an image.

In the STM, the tip is a sharp piece of wire, usually Pt-Ir or W, which is controlled with a piezoelectric stack. A bias voltage is applied between tip and sample, which causes a tunneling current to flow when the tip is brought within a few nanometers of the sample surface. This current is exponentially dependant upon the sample-tip distance, which makes it relatively easy to measure and control the tip height. Images can be collected in either topographic (constant-current) mode or constant-height mode. The most critical thing to remember about STM images is that they reflect the electronic structure of the sample, which can be different from the underlying physical structure.

In contrast to the STM, the other types of scanning probe microscopy don't have the luxury of an exponential behavior in the sample-tip interaction. Atomic force microscopy (AFM), as shown in Figure 3.7, relies on the Van-der-Waals force between

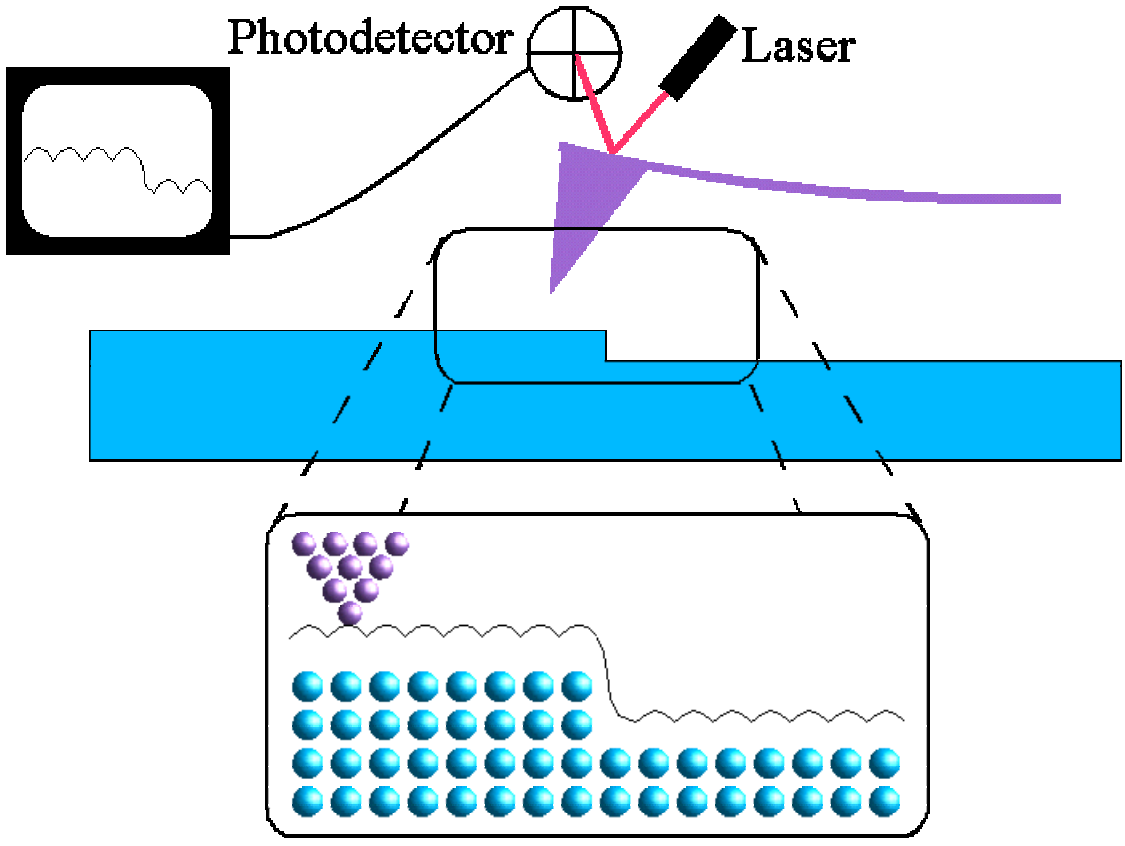

Figure 3.7: Atomic Force Microscopy.

the tip and the sample. The Van-der-Waals interaction is repulsive at short distance, attractive at intermediate distance, and asymptotically zero at large distances. Since the interaction is smaller, most modern microscopes do not use the deflection of the tip as a direct measure of the tip-sample distance. Instead, the tip is driven to oscillate close to its resonant frequency. When the tip interacts with the sample, the force gradient causes the frequency of the oscillation to change. This shift is easily detected with a lock-in amplifier so that it can be used as a feedback signal. This detection methodology is so flexible that it can be used for almost all possible tip-sample interactions. In addition to the van der Waals force that is always present, microscopes have also been created to measure impedance, capacitance, and magnetic information. The primary difficulty comes from the fact that the force measured by the tip is a combination of all of these forces. It is not trivial to separate the individual components of the force in order to form an image. Since my primary interest is measuring surface morphology, I have not had to resort to anything beyond tapping-mode atomic force microscopy using a Dimension 2100. Tapping-mode imaging occurs when the tip is in intermittent contact with the substrate as the tip oscillates. This a compromise between the excessive tip wear of full-contact imaging and the low resolution of non-contact imaging. Scanning probe techniques are extremely powerful, as evidenced by References [39, 40].

3.4 X-ray Diffraction

One of the most powerful techniques for characterizing solid samples is x-ray diffraction (XRD). It has been used to help understand everything from perfectly ordered inorganic bulk crystals to amorphous glassy materials.[41] It is capable of giving useful crystallographic information even for extremely small crystals of complex organic molecules, such as those needed by the pharmaceutical industry.[42]

Part of the reason for the utility of XRD is that the diffraction pattern contains a lot of information about the sample, and it is not particularly easy to squeeze out all of that information.[42-44] However, for the purposes of this work, a relatively simple understanding is more than sufficient.

X-rays are the part of the electromagnetic spectrum with a photon energy between 100 eV and 100 keV. For the purposes of diffraction, the "hard x-rays" are used, which have an energy between 1 keV and 100 keV, which implies a wavelength of approximately 0.1 – 2 Å. This is crucial, since the atomic size and lattice spacing are in this range, which allows diffraction effects to occur.

Consider the situation shown in Figure 3.8. A monochromatic X-ray source is incident upon a perfectly ordered, monatomic crystal. If each plane of atoms reflects a small portion of the incident radiation, then this will lead to constructive and destructive interference in the outgoing light. The angular position of these constructive peaks in intensity will depend upon the x-ray wavelength (λ) and the distance between the planes (d). This dependence is called *Bragg's Law*,

$$2d \sin\theta = n\lambda \tag{3.1}$$

where n is an integer, referring to the order of the diffracted beam. Of course, this result is completely general and holds true for any set of atomic planes in the sample, not just those parallel to the surface.

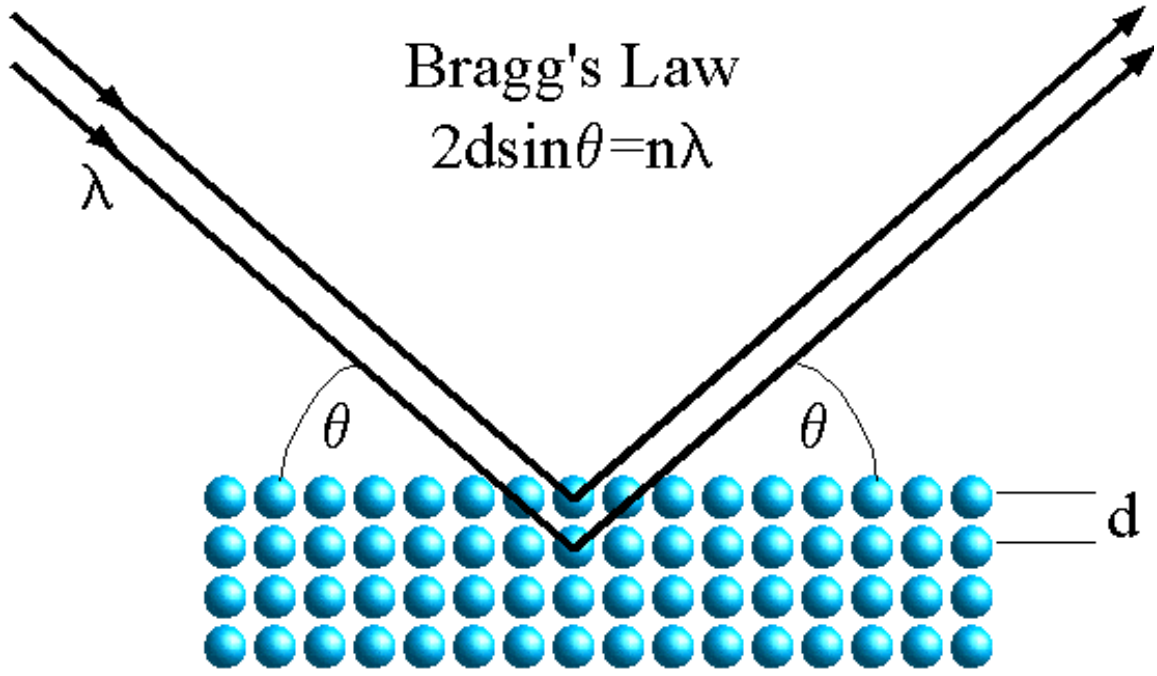

Figure 3.8: Bragg's Law.

If the detector in an XRD machine is scanned along θ for an unknown sample, the resulting graph of intensity versus angle can then be used to determine the lattice spacing. In our case, for thin films on top of substrates with a known crystalline substrate, the lattice spacing of the film can be determined. Since we are primarily interested in knowing the out-of-plane lattice spacing of our thin films, the scan can be limited to two peaks, one for the substrate and one for the film. This is shown in Figure 3.9. The substrate peak can be used to determine any instrumental parameters that can cause an angular offset in the diffracted beams. The position of the thin film diffraction peak is then used to determine the true lattice spacing of the thin film.

Figure 3.10 shows a representative example of the intensity versus angle scan for one of our samples. The peaks on the left are from the substrate, and the single peak on the right is the thin film peak. The x-rays are produced by a polychromatic source with high intensity at two neighboring wavelengths. In the case of our source, these are referred to as the $K_{\alpha 1}$ and $K_{\alpha 2}$ lines. This is the reason for the splitting in the substrate peak. Note that the substrate peaks are two orders of magnitude more intense than the

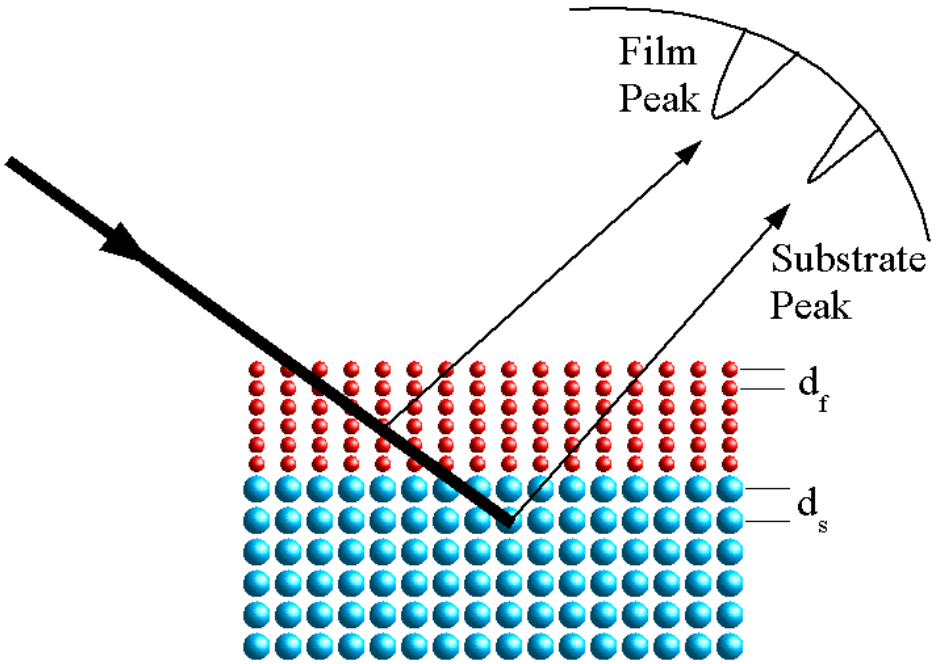

Figure 3.9: Diffraction for a thin film. Note that the difference in lattice spacing between the film (d_f) and substrate (d_s) leads to different angular positions for the diffraction peaks.

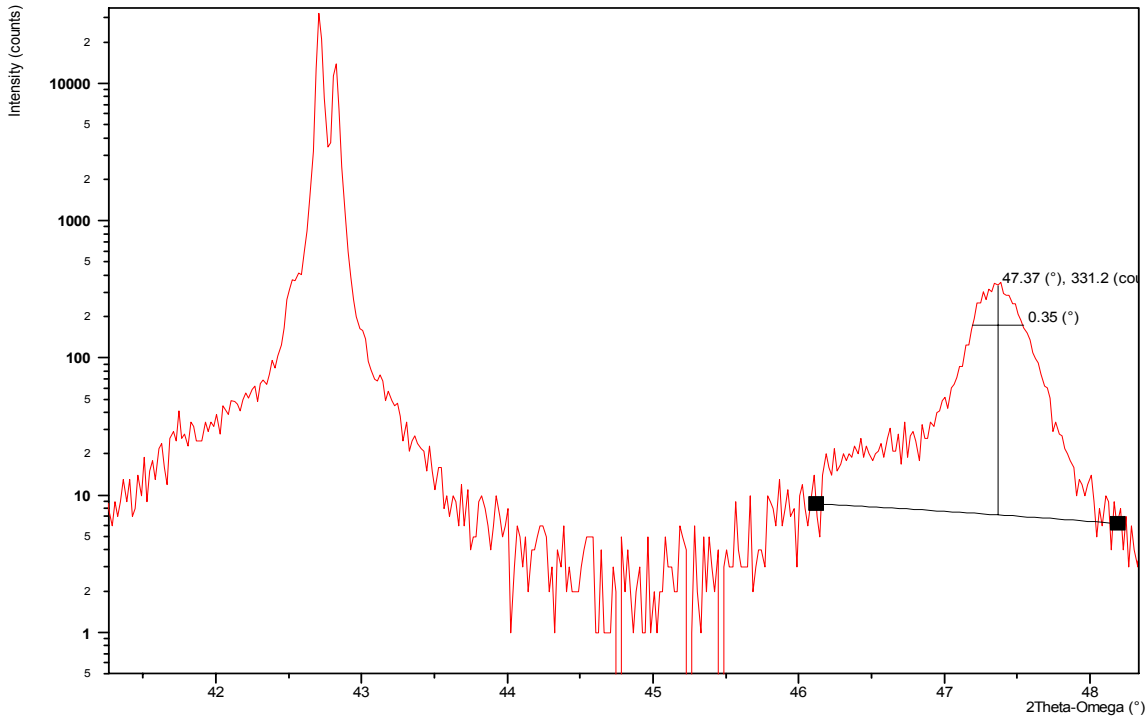

Figure 3.10: Example of XRD scan.

film peak. This is primarily the result of the thinness of the film. The sharpness of a diffraction spot is directly related to the amount of diffracting material, so the spot from a film that is tens of nanometers thick will naturally be much less intense than that from a substrate that is several millimeters thick. The film peak is also made more diffuse by any defects in the crystallinity of the film. These effects are strong enough that only a single film peak is observed, rather than a split peak like that of the substrate. Since the film peak is not completely resolved, we will have to make a slight correction for this effect when the peak positions are analyzed.

In the example above, since the wavelengths of the $K_{\alpha 1}$ and $K_{\alpha 2}$ lines are known (1.54056 and 1.54439 Å), as are the d-spacing of the substrate, the order of these particular diffraction spots, according to Bragg's Law we can calculate where the substrate peaks *should* be. The difference between where the substrate peaks should be and where they are is then the offset, which we can call θ_{off}.

$$\theta_{off} = 2Arc\sin(\frac{n\lambda}{2d_{substrate}}) \tag{3.2}$$

Note that the first factor of two comes from the experimental setup. The peak positions are measured as a function of 2θ, rather than θ.

This offset angle is then subtracted from the film angle when the lattice spacing is calculated. However, we still need to correct for the smearing of the film peak. We can make a rough correction for this by calculating an "effective wavelength" for the incident x-ray.

$$\lambda_{eff} = \frac{2\lambda_{\alpha 1} + \lambda_{\alpha 2}}{3} \tag{3.3}$$

The out-of-plane lattice parameter can then be calculated for the film.

$$d_{film} = \frac{n\lambda_{eff}}{2\sin(\theta - \theta_{off})} \tag{3.4}$$

3.3 SQUID Magnetometry

Magnetometry has played a central role in all of the research covered in this dissertation. Although there are many different magnetometers available, the only suitable device for my measurements is the SQUID magnetometer.[45] In this case, the specific device is the Quantum Design MPMS XL. It combines extremely high sensitivity with a large field and temperature range.

SQUID stands for Superconducting QUantum Interference Device. The SQUID magnetometer uses a DC SQUID, which consists of a pair of Josephson junctions connected in parallel in a superconducting loop, as shown in Fig 3.11a. The Josephson junctions are simply "weak links" in the superconductor through which the supercurrent of the superconductors can move, but where the critical current is reduced compared to the rest of the superconductor. In this way, the superconducting wavefunctions of the halves of the loop are linked by a phase relationship. The useful result of these linked superconducting states is that the magnetic flux Φ through the loop is allowed to change, but only in integer multiples of the flux quantum, $\Phi_0 = h/2e = 2 \times 10^{-7}$ G cm^2. At a constant bias current I_B, the voltage drop across the SQUID is then periodic in Φ with a step of Φ_0, as shown in Figure 3.11b. In a more advanced treatment of the physics of the SQUID device, it can be seen that these oscillations are in fact interference patterns

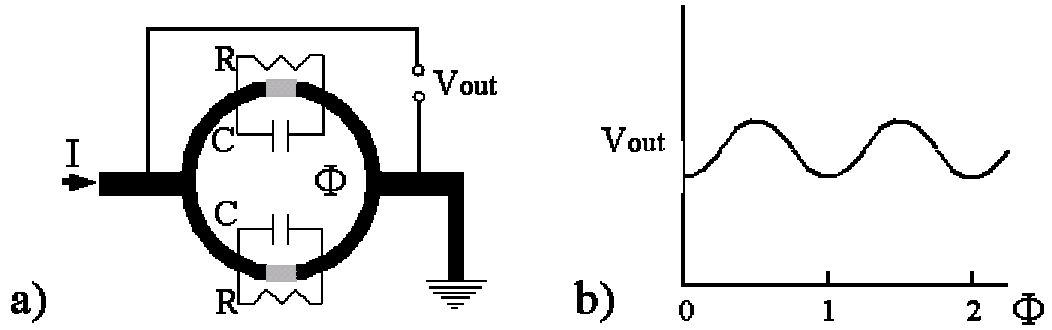

Figure 3.11: Basic operation of SQUID as a flux measuring device. a) Simple SQUID schematic b) Change in output voltage versus magnetic flux.

resulting from the interference of superconducting states in each half of the loop. This is the QUantum Interference referred to in the acronym.

This periodic dependence on the magnetic flux means that the DC SQUID is already useful as a flux measuring device. One could simply count the number of voltage oscillations and multiply by the flux quantum to get the total change in flux. Since the flux quantum is relatively small, then the device would already be fairly useful. However, with some relatively simple improvements, the sensitivity can be improved by several orders of magnitude.

The first modification is that the SQUID is used in *flux-locked* mode. This means that a secondary flux is applied to the SQUID by a separate inductor as part of a feedback circuit. The circuit is designed to keep the total flux through the SQUID constant. The applied current is then proportional to the external flux that we are trying to measure. This modification allows the measurement of external fluxes that are much smaller than the flux quantum. Current technology allows measurements with an accuracy of better than $10^{-4}\ \Phi_0$.

The second modification is that the SQUID is not used as a measurement device directly. The SQUID is coupled to the sample chamber through a continuous superconducting wire called a *flux transformer*. Since there are no Josephson junctions in the flux transformer, the flux through the loop formed by the flux transformer is a constant due to the Meissner effect. This means that if an inducting loop is wound over the SQUID, with a search coil wound at the other end, any changes in flux through the

search coil will be transferred to the SQUID by the loop. A simple schematic is shown in Fig 3.12a.

The third major modification is the use of a *second-derivative coil*, rather than a simple search coil. This is shown in Fig 3.12c. A second derivative coil consists of four coil loops formed in three distinct sections. The top and bottom loops turn in the clockwise direction, whereas the two middle loops turn counter-clockwise. With this geometry, the coils are insensitive to constant fields and to fields with a constant gradient. In order to understand this more easily, please consider the progression from the simple magnetometer in Fig 3.12a to the first-derivative gradiometer in Fig 3.12b. The magnetometer measures the total flux through the loop. The first-derivative gradiometer is essentially two matched magnetometers in series, turned head-to-head. If they are placed in a field with no gradient, the flux through the top loop will be exactly cancelled by the same flux through the bottom loop. When the fluxes no longer cancel, then the SQUID will see the gradient in the field. In the same sense, the second-derivative gradiometer is just two first-derivative gradiometers, turned head-to-head. Now fields with constant gradients will no longer register, but those with a changing gradient will register.

The second-derivative gradiometer is used in the Quantum Design MPMS XL in the following way. The gradiometer is mounted inside the bore of a cylindrical superconducting magnet. The sample is mounted to the sample holder rod, which is moved downward through the coils of the gradiometer in a controlled manner, with the

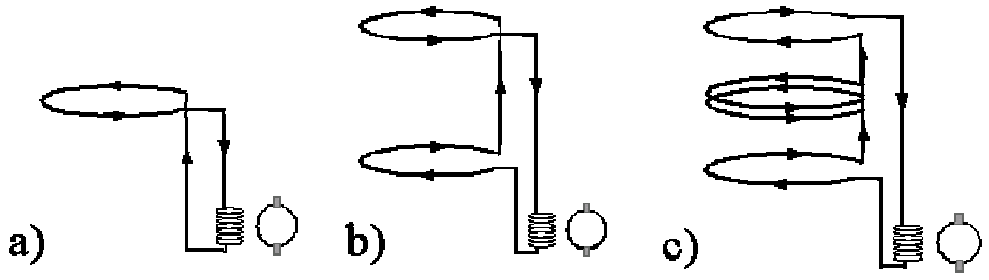

Figure 3.12: Different search coil types a) flux magnetometer b) flux gradiometer c) second-derivative flux gradiometer.

SQUID voltage measured at several points along the sample travel. Since the magnetic field inside a cylindrical superconducting magnet is quite uniform **and** the gradiometer is insensitive to the magnetic field and its first derivative, the applied field does not influence the measurement. The flux changes from the sample form the bulk of the measured signal. A simple representation of the measured data is shown in Figure 3.13b. This measured voltage vs. position curve is then fitted with the theoretical curve from a point dipole traveling through the same coil geometry. This theoretical fitting yields the measured magnetic dipole moment of the sample. The fitting procedure is not perfect, of course, and the measured moment can be influenced by such factors as imperfections in the sample holder and the geometry of the sample. Samples are usually mounted on a quartz rod or inside a plastic straw. Since the straw or rod is longer than the search coils, the flux from magnetic moments induced in the rod usually has very little second derivative. However, imperfections in the straw or rod that are shorter than the length of the search coils will have a second derivative and will show up in the measured moment. The geometry of the sample can also change the measured moment. If the sample is long and thin, the measured moment will be reduced compared to that of a short sample, even if the true moment is the same. For our samples, this was not particularly important, since for each family of samples (thin film or powder) the sample geometry does not change very much.

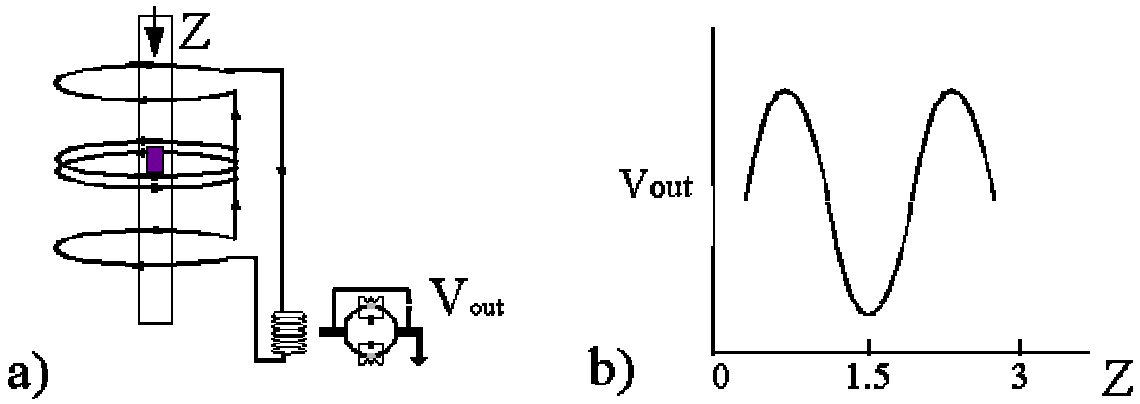

Figure 3.13: Quantum Design MPMS magnetometry a) Schematic of flux coils b) Output voltage from flux-locked SQUID.

3.5 Transport Measurements

For the CMR manganite materials, transport measurements are very important. The mechanisms responsible for the CMR effect are still poorly understood, and the resistances of the samples must be measured. In general, we would like to be able to measure the resistance of the sample as a function of temperature and applied magnetic field. If possible, it is also useful to measure the Hall voltage in the sample. After several months of effort, we perfected the following procedure.

First, metallic contacts are evaporated onto the sample, as shown in Figure 3.14. The contacts generally consist of a 30nm titanium adhesion layer covered with a 30nm gold layer. Gold is chosen for its durability and excellent conductivity. Unfortunately, gold does not adhere well to the oxide film, so the titanium adhesion layer is used. The titanium probably scavenges oxygen from the underlying film to form a titanium oxide layer, but this does not seem to cause any problems in the transport measurements. Other measurements like x-ray diffraction and magnetometry can be performed after the contacts are deposited if necessary, but it is preferable for transport measurements to the very last measurements performed on any given sample. It is also useful to measure the dimensions and spacing of the contacts on each sample for later reference.

In the second step, the samples are affixed to the measurement puck and then aluminum wire is used to connect the sample contacts to the puck contacts. Since the

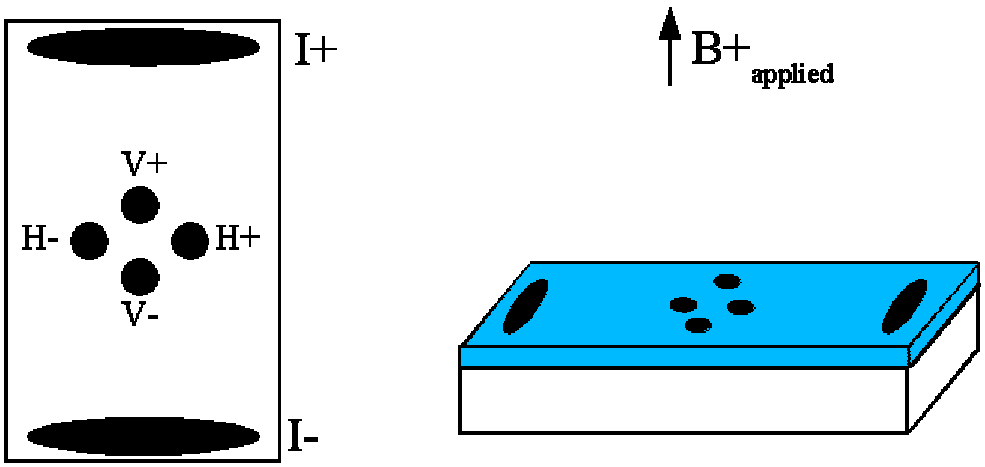

Figure 3.14: Transport contacts for resistance and Hall measurements.

thin films are generally quite small, with the electrodes even smaller, we were forced to use a wire bonder to make the contacts on the electrodes and puck contacts. Our primary measurement system is the Quantum Design Physical Property Measurement System (PPMS). The PPMS can measure DC and AC transport, thermal conductivity and heat capacity with available temperatures of 1.9 – 400K and magnetic fields up to 14 Tesla. For our samples, we were only interested in using the DC transport function.

Finally, the pucks are installed into the PPMS system and the measurements are performed. Unfortunately, we have not found a way to perform Hall measurements and normal transport measurements simultaneously. The samples must be removed from the PPMS chamber and the wires must be removed and new wires must be connected from the puck contacts to the sample contacts.

Chapter 4 Experimental Results

4.1 $La_{5/8-0.3}Pr_{0.3}Ca_{3/8}MnO_3$ Thin Film Magnetism and Transport

As detailed in Section 2.4, even after five decades of research, the physics of the manganites is still somewhat unresolved. Some loose consensus seems to exist over the presence of phase separation and its general role in conductance, but the underlying mechanisms are still debated.

In this chapter, I am taking advantage of the close interplay between the structural, electronic, and magnetic degrees of freedom in manganites in order to try and gain more information about the underlying physics. By growing similar manganite thin films epitaxially on a variety of substrates, we can alter the lattice strain of the thin film.[46] In this way, we can observe how relatively small structural changes can cause large changes in the electronic and magnetic properties of the film.

We have prepared films of $La_{5/8-0.3}Pr_{0.3}Ca_{3/8}MnO_3$ on $SrTiO_3$ (STO), $LaAlO_3$ (LAO), $NdGaO_3$ (NGO), and $SrLaGaO_4$ (SLGO) substrates. The relevant properties of the substrates are summarized in Table 4.1. The substrate-induced strain within the films is tensile for the STO and NGO substrates and compressive for the LAO substrates. Films on SLGO should be nearly strain free. We have chosen a calcium concentration of x=3/8 which maximizes the Curie temperature for the parent compound, bulk $La_{1-x}Ca_xMnO_3$. A praseodymium concentration of y=0.3 was chosen as a compromise between having a robust charge-ordered state and a reasonable peak resistance.

Table 4.1: Crystal properties of substrates and films[47]

	Crystal Type	Lattice Constant a-axis (Å)	Nominal Lattice Misfit	Lattice Constant c-axis (Å)	Density (g/cm^3)	Melting Point (C)	Exp. Coeff 10^{-6}
LPCMO	**Perovskite**	**3.84**	**--**	**3.84**	**6.023**	**--**	**--**
$LaAlO_3$	**Rhomb.**	**3.790**	**-1.30%**	**13.11**	**6.51**	**2180**	**9.2**
$SrLaGaO_4$	**Tetragonal**	**3.84**	**~0%**	**12.68**	**--**	**1238**	**6.0**
$NdGaO_3$	**Orthorhomb.**	**5.43**	**~0%**	**7.71**	**7.57**	**1600**	**4.5**
$SrTiO_3$	**Cubic**	**3.905**	**+1.7%**	**3.905**	**5.12**	**2080**	**10.3**
MgO	**Cubic**	**4.216**	**+9.8%**	**4.216**	**3.58**	**2800**	**12.8**

4.1.1 Sample Preparation

The samples were grown using laser molecular-beam epitaxy (laser MBE) as introduced in section 3.1.1. A KrF excimer laser with a wavelength of 248nm, a repetition rate of 2-5 Hz was used, with an energy density at the target of 1-2 J/cm^2. The substrates were cleaned and annealed before being inserted into the growth chamber. The substrate temperature during deposition was 820 °C, and the flowing oxygen (8% ozone) was introduced into the chamber through a nozzle approximately 15 mm from the substrate. The background oxygen pressure was 0.5 mtorr, with a local pressure near the substrate estimated to be an order of magnitude higher. The substrates were *in situ* annealed for 30 minutes before deposition at the same temperature and oxygen pressure. Deposition was monitored *in situ* using reflection high-energy electron diffraction (RHEED). No reconstructions due to oxygen deficiencies were observed. After deposition, the samples were *in situ* annealed for 15 minutes and cooled to room temperature at the same oxygen pressure. The resulting films were *ex situ* annealed in flowing oxygen (1 atmosphere) at 870 °C for 5 hours to further reduce bulk oxygen vacancies.

4.1.2 Sample Characterization

The surface morphology of the resulting films was examined using atomic force microscopy (AFM). The resulting images are consistent with good epitaxial growth and have relatively few droplets.

The epitaxial quality and relative strain were examined using x-ray diffraction (XRD). Four-circle x-ray diffraction reveals slightly broadened peaks consistent with a gradual relaxation of strain through the film thickness. For all samples, the diffraction data were consistent with the simplified assumption of a tetragonal structure having an in-plane lattice parameter a=b and a formula unit volume of ~(3.84A).[48] The corresponding c-axis parameter (a_c) is given in the third column of Table 4.1, and the θ-2θ curves are shown in Figures 4.1 – 4.4. Note that the a_c values are essentially unchanged as a function of thickness for each substrate type. Similarly, an increase in a_c shows that LAO films are under compressive strain, while the small change in a_c for

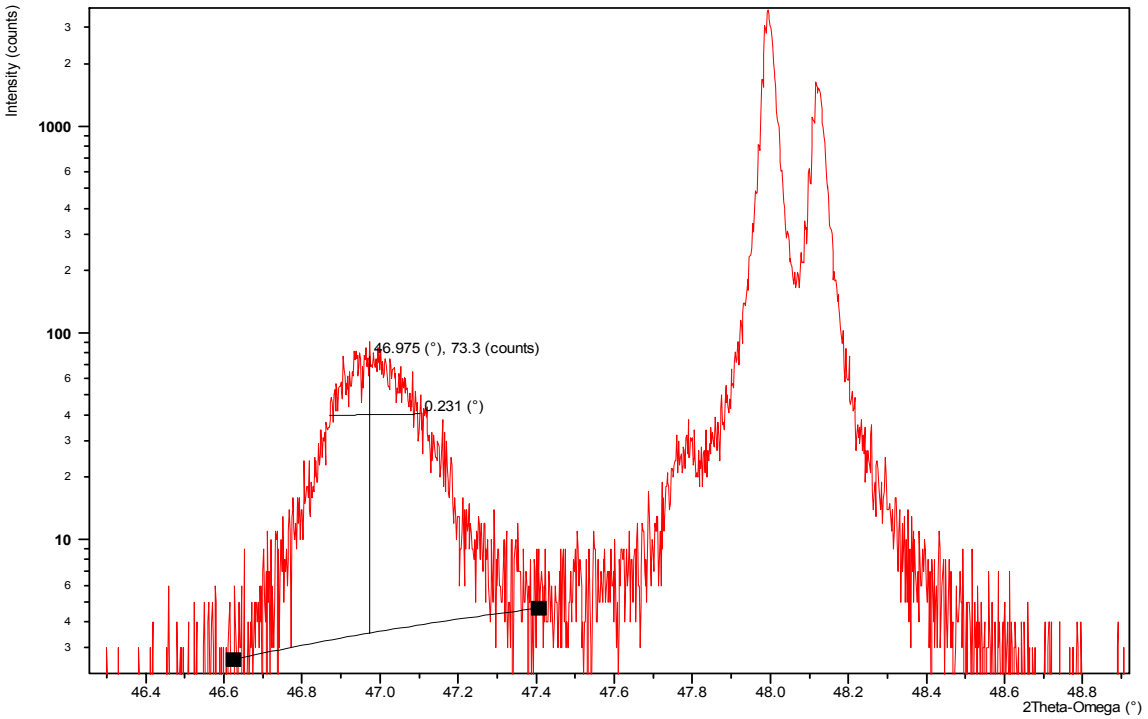

Figure 4.1: 90nm thick LPCMO on LAO.

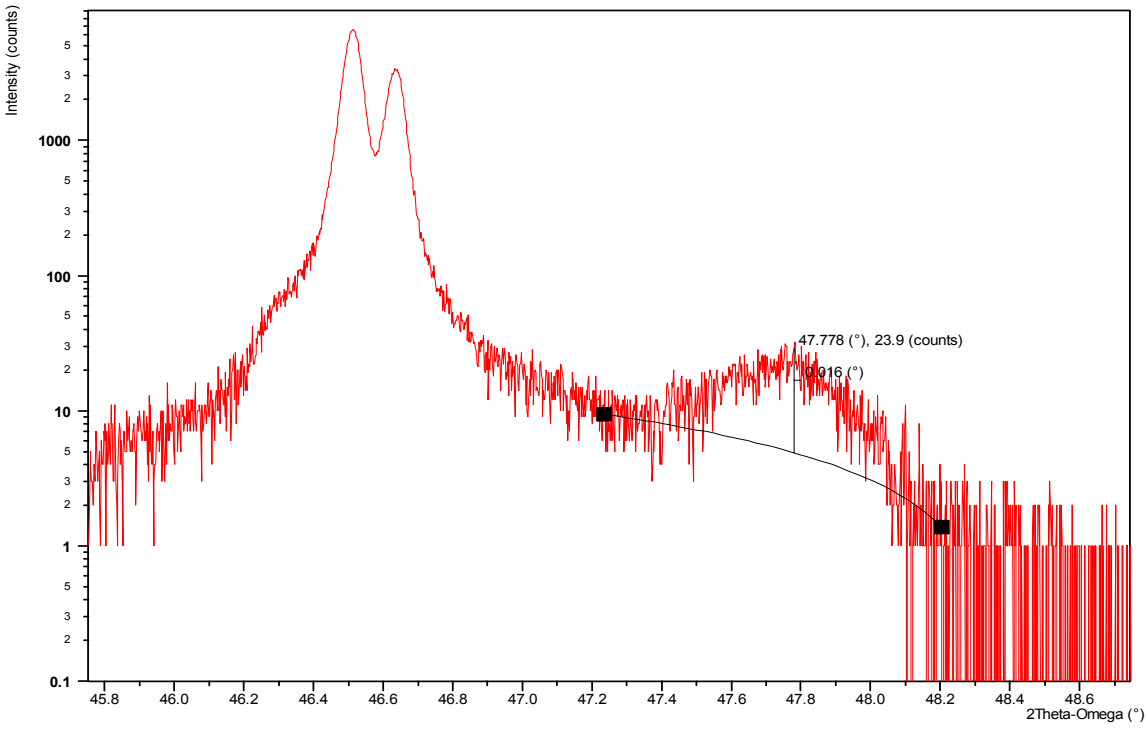

Figure 4.2: 90nm thick LPCMO on STO.

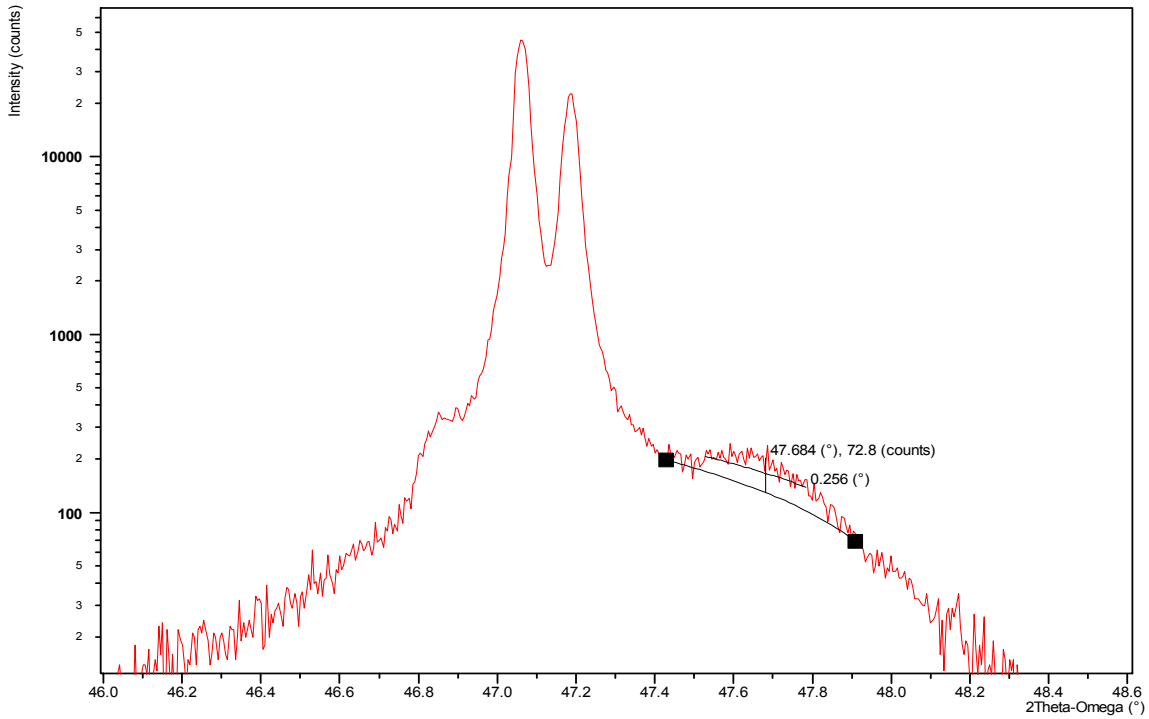

Figure 4.3: 30nm thick LPCMO on NGO.

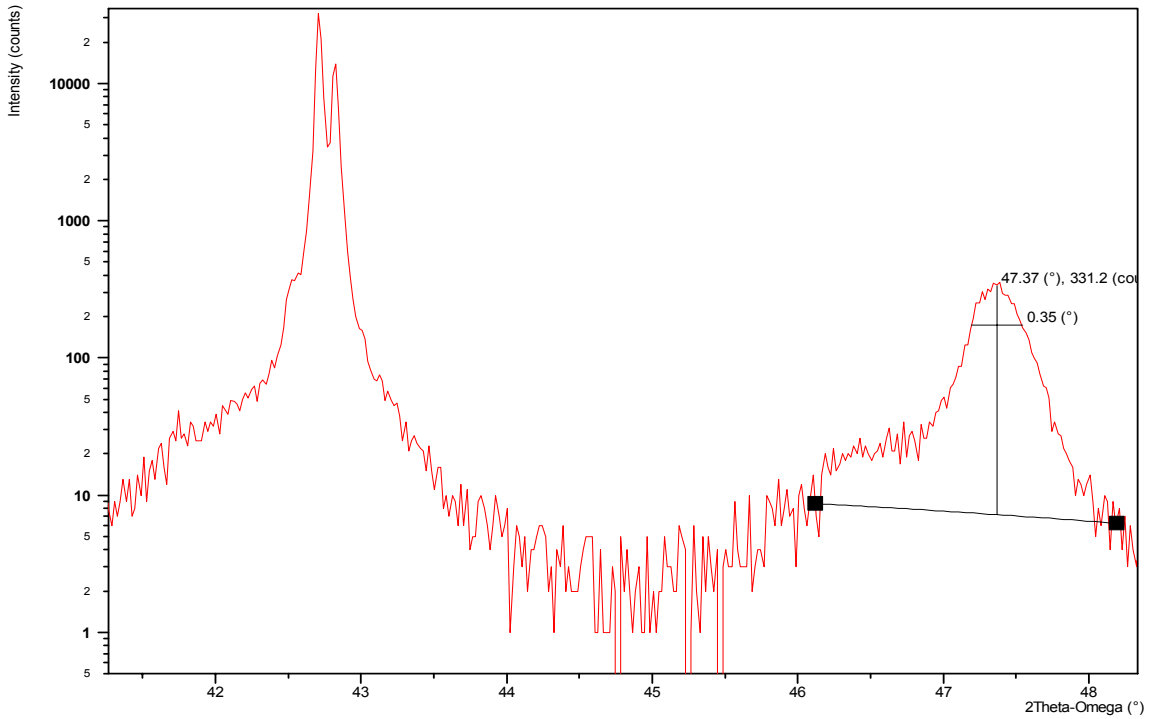

Figure 4.4: 66nm thick LPCMO on SLGO.

films on SLGO means that they are almost strain free.

One major ongoing problem exists with the LAO substrates, however. At 544 °C LAO undergoes a transition from a cubic high-temperature phase to the rhombohedral low-temperature phase. This means that all deposition occurs on cubic substrates, but all measurements occur on rhombohedral substrates. In addition, the rhombohedral distortion induces the formation of twinned domains.[49] These domains give the samples a streaky appearance and make x-ray diffraction much more difficult.

The samples of primary interest fall into two thickness regimes. We have grown 30-nm-thick samples for all substrates, and 90-nm-thick films on STO, LAO, and SLGO. The 30-nm films should be well below any sort of strain-relieving transitions, where defects and dislocations can form to release the strain energy. The 90nm films were believed to be above this strain-relief limit, but the x-ray diffraction data shows no obvious signs of defect formation.

After characterizing the film quality, all samples are mounted in the Quantum Design SQUID magnetometer for measurement. Unfortunately, the NGO substrate is paramagnetic and the magnetic response of the substrate overwhelms that of the thin film for the method employed here.[50] The magnetoresistance data were taken using a Quantum Design physical property measurement system (PPMS). In order to minimize the effects of contact resistance, gold contacts were patterned in a four-point configuration, as shown in Section 3.5.

Figure 4.5 shows the temperature dependence of the magnetic moment for 90-nm-thick films through a full cooling-warming cycle. Hysteresis appears below 210K for all samples. This coincides with the onset of short-range ferromagnetic (FM) and charge-ordered (CO) ordering. Upon further cooling, another transition occurs, coinciding with the development of long-range FM and CO phases. The bump at 43K is observed for all samples due to residual oxygen in the SQUID chamber. (Solid oxygen undergoes a diamagnetic-paramagnetic transition at ~43K, so the observed moment increases dramatically even for a small amount of oxygen.) When the temperature of the sample is increased, the FM phase is frozen, yielding and increased moment relative to the cooling curve. The inset in Figure 4.5 shows the field dependence of the magnetization M(H)

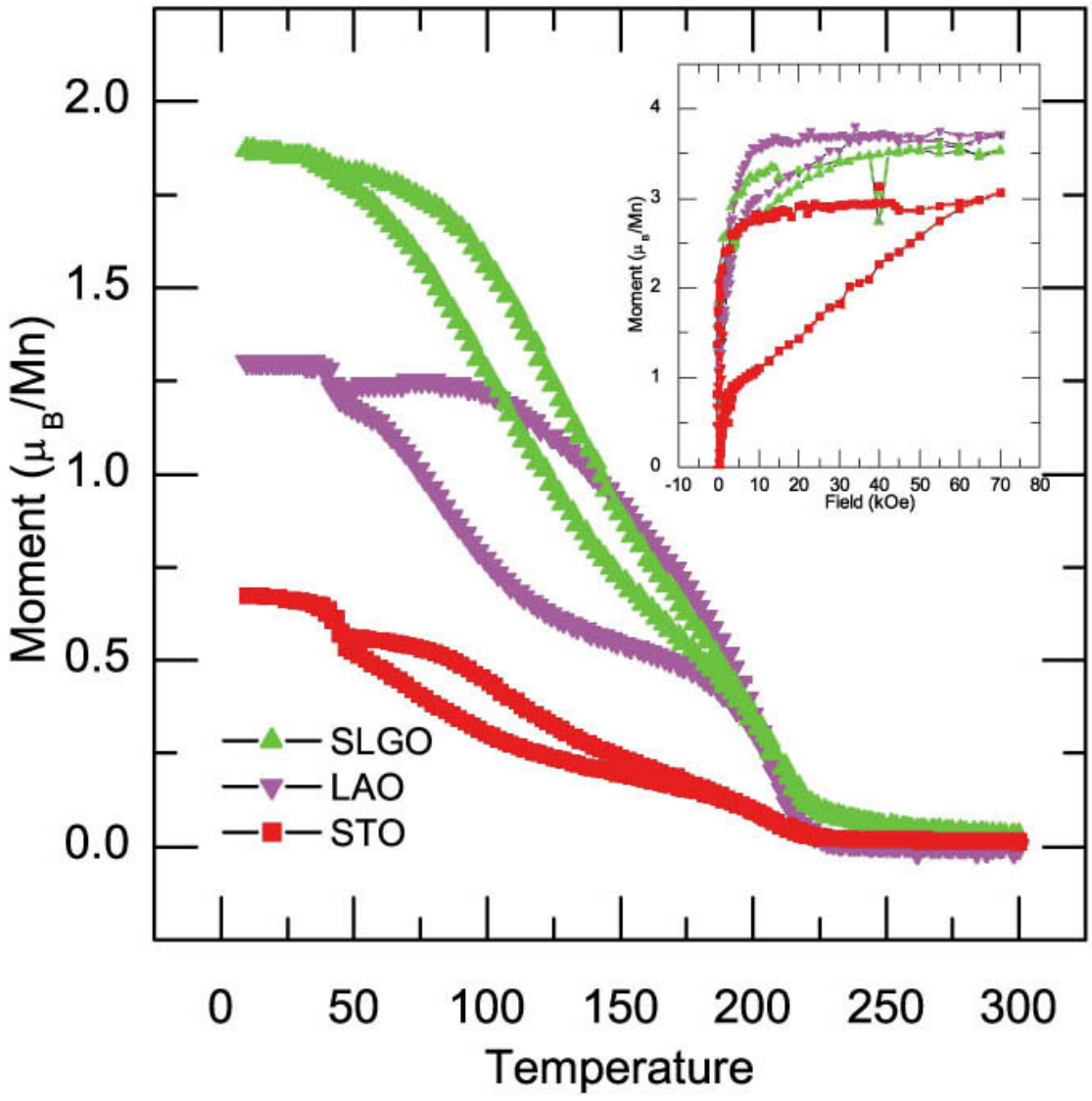

Figure 4.5: Magnetic data for 90-nm-thick LPCMO films on STO, SLGO, and LAO substrates. The applied field is 500 Oe. The inset shows magnetic moment versus applied filed for the same three samples at 5 K.

measured at 5K. During the initial magnetization, the magnetic moment increases rapidly until the ferromagnetic domains are aligned at 5 kOe. Increasing the magnetic field causes the irreversible transformation of the CO phase into the FM phase. M(H) saturates at 35 kOe for films on LAO and SLGO. The saturation magnetic moment is 3.6 mB, which is very close to the ideal FM saturation value of 3.625 mB for bulk LPCMO. For films on STO the magnetic moment does not saturate, even with the maximum available field of 70 kOe. The saturation moments are 2.8 mB and 3 mB for the 30nm and 90 nm films on STO, respectively. This demonstrates that the CO state is more stable in tensile strained films.

The transport properties were measured as a function of field and temperature. Figure 4.6 shows the temperature dependence of resistance for 90-nm-thick samples at zero field and 35 kOe. The first transition, defined as the most rapid change in resistance versus temperature, is visible at 210 K for all samples. This is consistent with the magnetic measurements. Films on compressively strained LAO and strain-free SLGO show a metal-insulator transition, while the film on STO shows insulating behavior. This indicates that the percolation threshold is not reached due to the enhancement of the CO phase. The charge-ordered phase is partially melted with an applied magnetic field of 35 kOe. The behavior of the 30-nm-thick films, as shown in Figure 4.7, is similar to that of the thicker films, with the exception that the metal-insulator transition occurs at higher applied field for the film on STO. The 30-nm-thick film on NGO also has a field-induced metal-insulator transition. The FM transition temperature (T_C), estimated from the maximal slope of the resistance versus temperature curves, also shows substrate-induced changes. For compressively strained films on LAO, T_C = 80 and 90K for the 30 and 90nm samples, respectively. In the strain-free films on SLGO the corresponding T_C are 137 and 145K.

These results demonstrate that for tensile strained films, the CO state is enhanced due to the in-plane expansion and out-of-plane contraction of the film. In order to understand this, please recall the Jahn-Teller distortions in Figure 2.9. Note that the energy of the electron is lowered when the oxygen octahedron is extended, which serves to trap the electron at that site. When the film is strained in the xy-plane, the octahedra

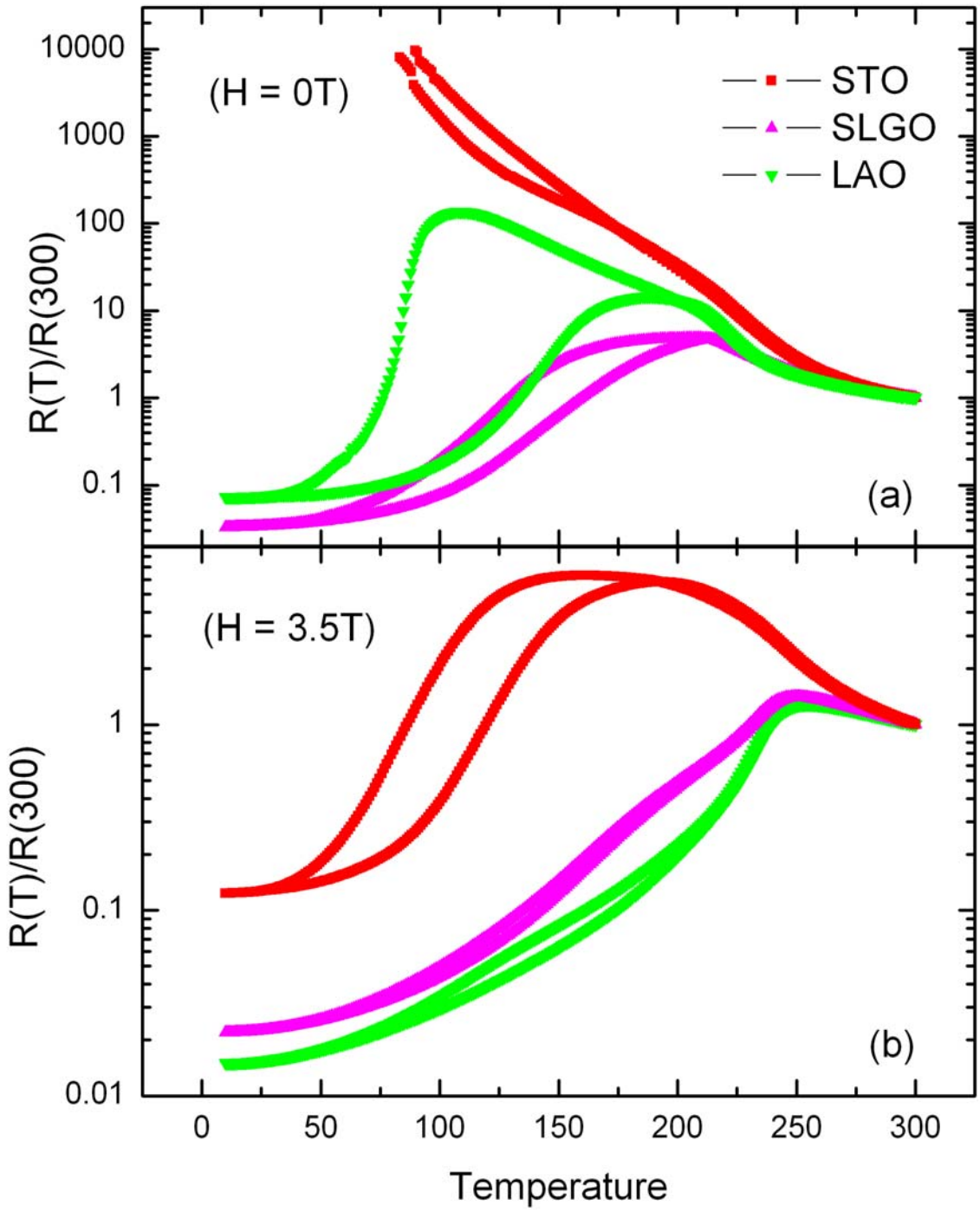

Figure 4.6: Normalized four-point resistance for 90nm LPCMO films on STO, SLGO, and LAO substrates. (a) zero applied field (b) 35 kOe applied field.

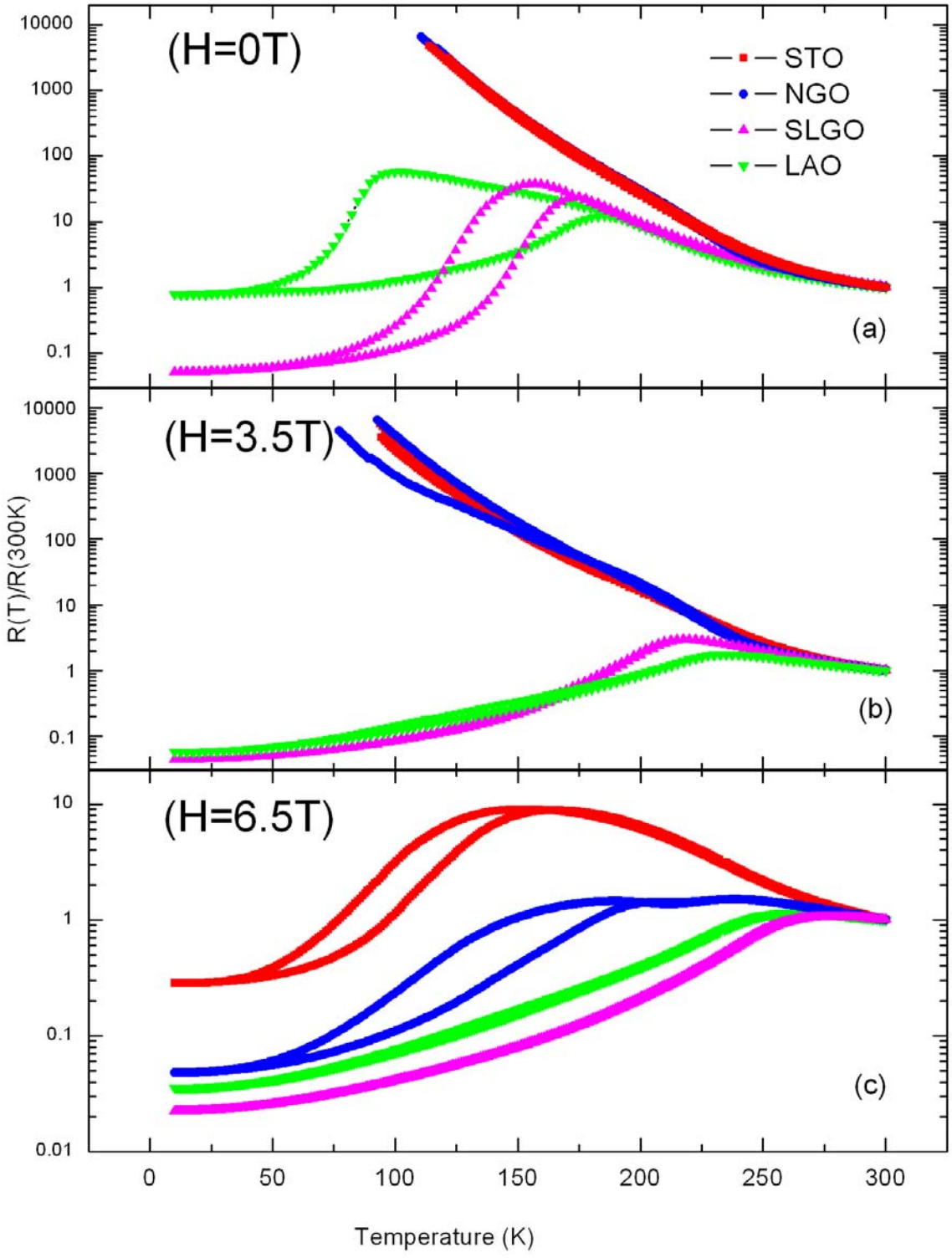

Figure 4.7: Normalized four-point resistance for 30nm LPCMO films on STO, NGO, SLGO, and LAO. (a) Zero applied field (b) 35 kOe applied field (c) 65 kOe applied field.

will tend to be extended in the xy-plane. Since each octahedron is linked with six other octahedra, these effects will be cooperative, which should favor extended charge-ordered regions in the plane. In this sense, we can say that tensile strain favors the long-range CO state. Conversely, for the compressively strained films the long-range in-plane charge-ordering should be suppressed. However, it appears that the short-range FM/CO phase separation is enhanced, as characterized by the sharp metal-insulator transition and pronounced hysteresis.

4.2 Visualization of Localized Holes in LPCMO Thin Films

As discussed in the previous section, perovskite manganites are characterized by physical complexity resulting from the coexistence and competition among different kinds of order involving charge, orbital, lattice, and spin degrees of freedom. It has been proposed that the strong electron-lattice coupling leads to formation of polarons when manganites are doped with holes. In this section, the results of imaging studies on hole-doped manganites thin films using scanning tunneling microscopy are given, and the results are discussed in the context of polarons and phase separation.

4.2.1 Sample Preparation

Epitaxial LPCMO thin films were grown on Nb-doped, (001)-oriented $SrTiO_3$ (STO) single crystal substrates using laser MBE. The general parameters of the growth were the same as those given in the last section. The STO substrates were chemically etched and *in situ* annealed for 30 minutes at 820 °C before growth. The substrate temperature was kept at 820 °C to allow step-flow growth, produces a thin film with minimal oxygen deficiency and other defects. After growth, the samples were immediately cooled down to room temperature and transferred to the STM chamber. Samples prepared in this way do not exhibit oxygen deficiency-induced surface reconstruction.

When the STO substrates are prepared as stated, the result is a Ti-terminated surface. On such a surface, unit cell by unit cell epitaxy of the manganite thin film should lead to a Mn-O terminated surface. Figure 4.8 shows typical STM topographic

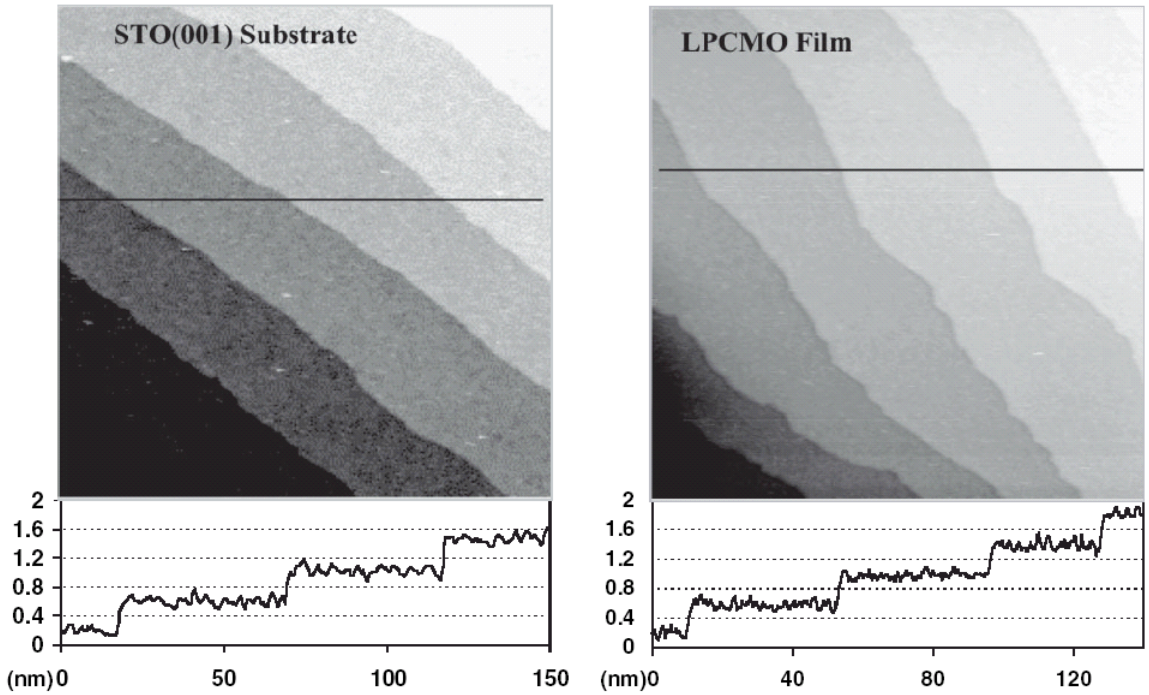

Figure 4.8: Typical topographical images of (a) a chemically etched and *in situ* annealed STO (001) substrate and (b) a 120 nm-thick LPCMO thin film. The line profiles indicate that the steps of both the substrate and the thin film are unit-cell high.

images of a STO substrate and a thin film (120 nm) grown in the step-flow mode. All steps on the substrate and the films have a height of a single unit cell (~4 Å), indicating that only one kind of termination layer dominates the surface. Occasionally, we have observed a small area of the surface with another type of termination layer near the step edges (not shown). Our observation is consistent with previous studies, which confirmed the Mn-O termination in manganites thin films grown on Ti-O terminated STO substrates.

4.2.2 STM Imaging of Localized Holes

All STM images were acquired with mechanically cut Pt-Ir tips at pressures better than 1 x 10^{-10} torr. A bias voltage is applied to the tip, and the sample is grounded, which means that positive and negative bias images reveal occupied and unoccupied states, respectively. As with the films in the last section, Figure 4.9 shows that these films confirmed all the essential features of ferromagnetic-charge ordering (FM-CO) phase separation, as indicated by the thermal hysteresis behavior in the temperature- and field-

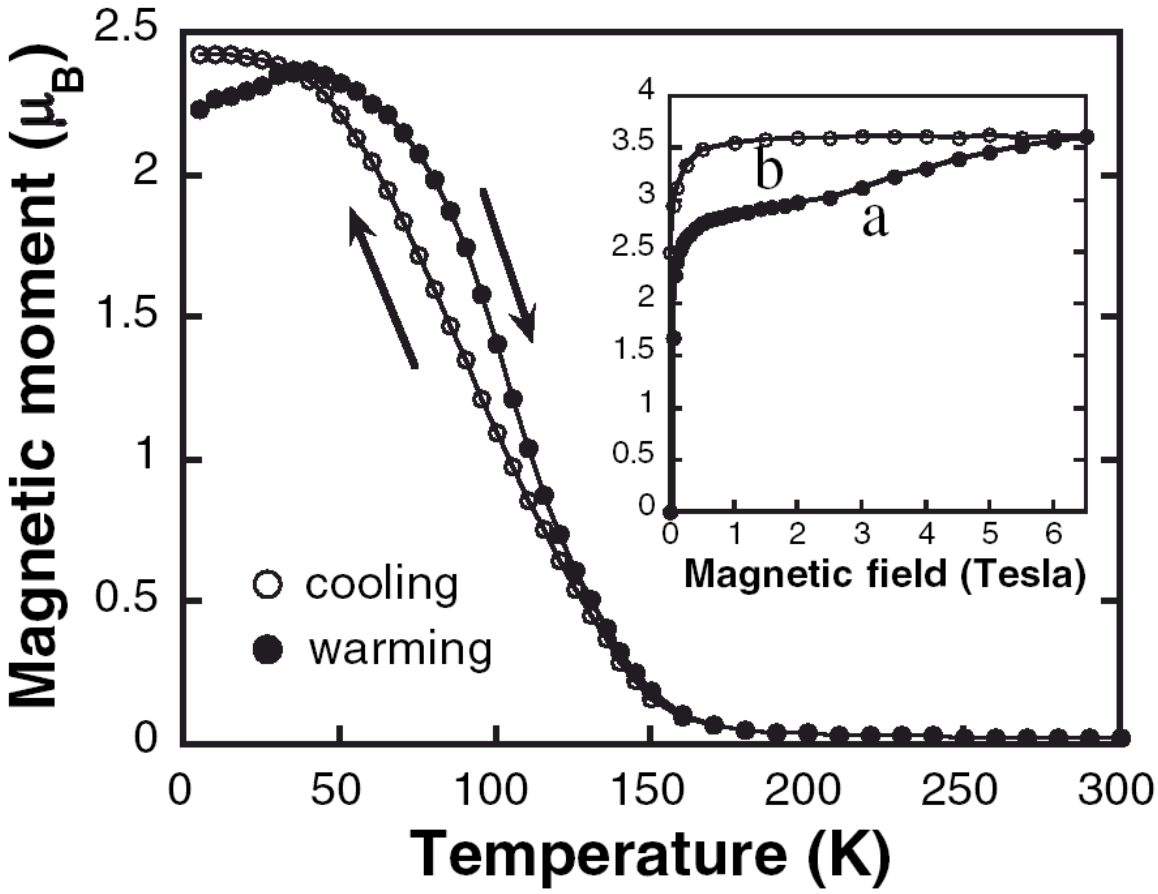

Figure 4.9: Temperature dependence of the magnetic moment of LPCMO thin film measured at 0.1 T. Hysteresis is visible in the cooling and warming curves below 160 K due to the coexistence of FM and CO phases. Inset shows the field dependence of the magnetic moment measured at 5 K. Curve "a" and "b" represent initial magnetization and subsequent field decrease. Above 2T, the CO state starts to transform irreversibly into the FM state and is fully transformed at 6.5 T.

dependent magnetization measurements.

With the STM in dual bias mode at room temperature, localized holes in the Mn-O surface layer can be imaged directly with atomic resolution. Figure 4.10 shows 20 nm x 10 nm dual bias STM images obtained simultaneously in the same area at room temperature. A regular square lattice (lattice constant 4 Å) oriented along <100> directions is clearly visible in both (a) occupied and (b) unoccupied state images. In both images, there are two types of lattice sites with different height contrast. This is best shown in Figure 4.10c by the marked line profiles taken from the same surface location of the occupied-state (red) and unoccupied-state (black) images. The height difference between the bright and dark sites is particularly large in the unoccupied-state image, which is about 1.0 Å as compared with 0.3 Å in the occupied-state image. Interestingly, the bright sites in the unoccupied-state image become dark sites in the occupied-state image, which is a strong indication that the contrast has an electronic origin. Recalling the fact that the surface is terminated with a Mn-O plane, it is reasonable to claim that the two types of lattice sites are associated with Mn^{3+} and Mn^{4+} ions. In the unoccupied-state image, the brighter sites should correspond to the locations of the Mn^{4+} ions (localized holes), which have a high-density unoccupied e_g state just above the Fermi level that gives rise to a larger tunneling current. The contrast between the Mn^{3+} and Mn^{4+} sites is reversed and becomes weaker in the occupied-state image, since Mn^{3+} has four (three t_{2g} and one e_g) electrons and Mn^{4+} only has three (t_{2g}) electrons below the Fermi level that can contribute to the tunneling current under the experimental bias voltage.

We estimated the ratio between the Mn^{4+} and Mn^{3+} sites to be about 0.45, which is somewhat lower than the nominal ratio of 0.6 for 3/8 Ca doping. Intrinsically, there are three likely causes for the reduction of the effective level of hole doping. First, for the Mn-O terminated surface, the hole doping is provided only from below the surface. Second, the e_g electrons are partially localized through their interaction with lattice, as was shown in Figure 2.10, which in turn would lead to a reduction of the localized holes in STM images because our STM cannot visualize the dynamic holes. Hall measurements to look for the dynamic holes are discussed in the next section. Finally, the polar surface, without being accommodated by surface reconstruction, may be

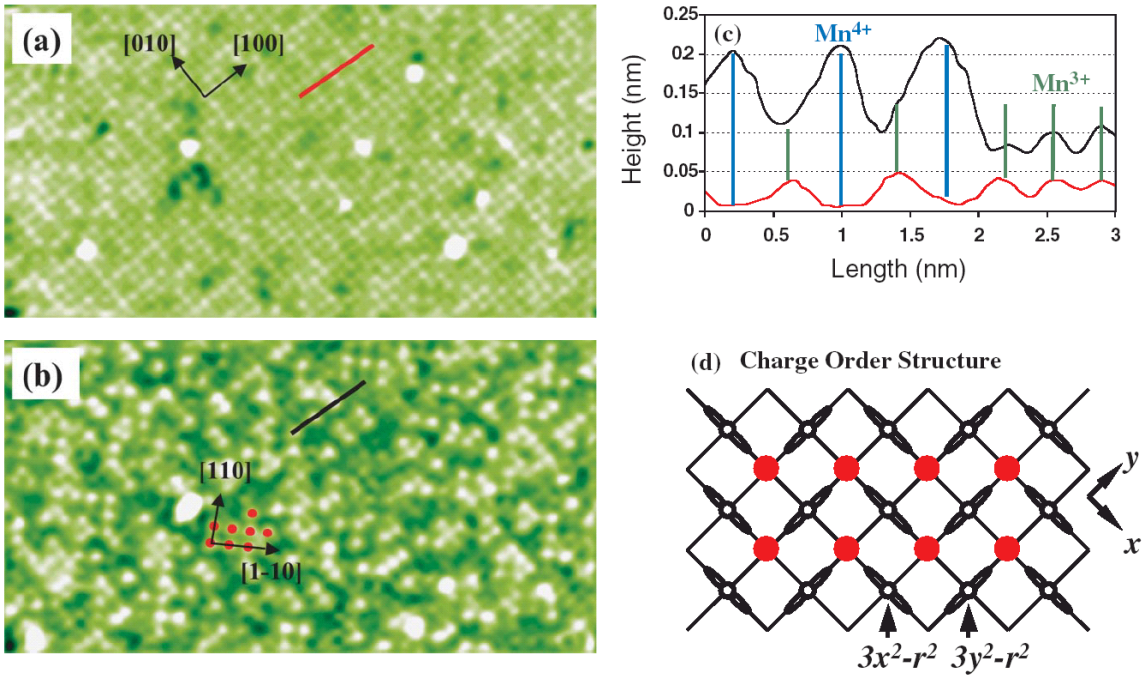

Figure 4.10: 20 nm x 10 nm dual bias STM images obtained simultaneously in the same area at paramagnetic state of a 120 nm LPCMO film. (a) Occupied-state image (V_{bias} =1.5 V, I_t = 0.020 nA) and (b) unoccupied state image (V_{bias} =-2.0 V, I_t = 0.050 nA). Both (a) and (b) reveal the same square lattice of Mn ions. In the unoccupied-state image, the brighter and darker lattice sites correspond to Mn^{4+} (localized hole) and Mn^{3+} ions, respectively. The relative contrast between Mn^{4+} and Mn^{3+} ions is reversed in the occupied-state image. (c) Marked line profiles showing the relative contrast between Mn^{4+} (indicated by blue lines) and Mn^{3+} (indicated by green lines) ions. The CE-type CO cluster is indicated by the red spots in the unoccupied-state image, with a schematic picture shown in (d).

energetically more favorable to adopt a different hole concentration. In addition, the conducting state at the surface could be affected by the broken symmetry effect on the competition between double and super-exchange interactions.[51, 52] The actual mechanism remains to be investigated further. At this stage, we cannot completely rule out the possibility that there is a variation of Ca concentration near the surface of the LPCMO film, although one would expect an increase of the Mn^{4+} versus Mn^{3+} ratio based on a previous study showing that Ca concentration increased near the surface of a $La_{1-x}Ca_xMnO_3$ thin film[53].

Knowing the spatial distribution of the doped holes at the surface, we can now discuss the correlation of the doped holes as compared to a random distribution. We define hole-hole correlation as CO-type and non-CO-type. Those holes occupying neighboring sites along the [110] and/or [$1\bar{1}0$] directions are viewed as CE-type CO clusters as indicated (red dots) in Figure 4.10 b and shown schematically in Figure 4.10d. Neighboring holes along the [100] and/or [010] directions are viewed as non-CO clusters. Figure 4.11 shows the statistical distribution of the non-CO and CO clusters obtained from Figure 4.10b, which is compared with that of a two-dimensional random distribution (2DRD) with the same doping level. The 2DRD model is generated in two steps. First, a random distribution of holes is generated on a 500 x 500 grid. The number of hole clusters of each size is then collected and stored. Then, 20 subsets of the larger grid are taken and the size distributions are generated for each subset to generate the standard distribution. The distribution of localized holes in Figure 4.10b is distinctly different from that of the 2DRD. In particular, the experimental data show a strong preference of forming small sized non-CO clusters. The average size of the non-CO cluster sizes obtained from Figure 4.10b is1.9 holes, which is considerably smaller than the 2.6 hole average of the 2DRD. This observation indicates a strong short-range hole-hole correlation, and the formation of larger clusters is energetically unfavorable in the paramagnetic state. In addition, the number of CE-like CO clusters obtained from the STM data is distinctly higher than that of the random distribution. These differences, however, should reflect only the behavior of the static doped holes, since our STM is not sensitive to the motion of dynamic holes. Our results demonstrate that for LPCMO, CO

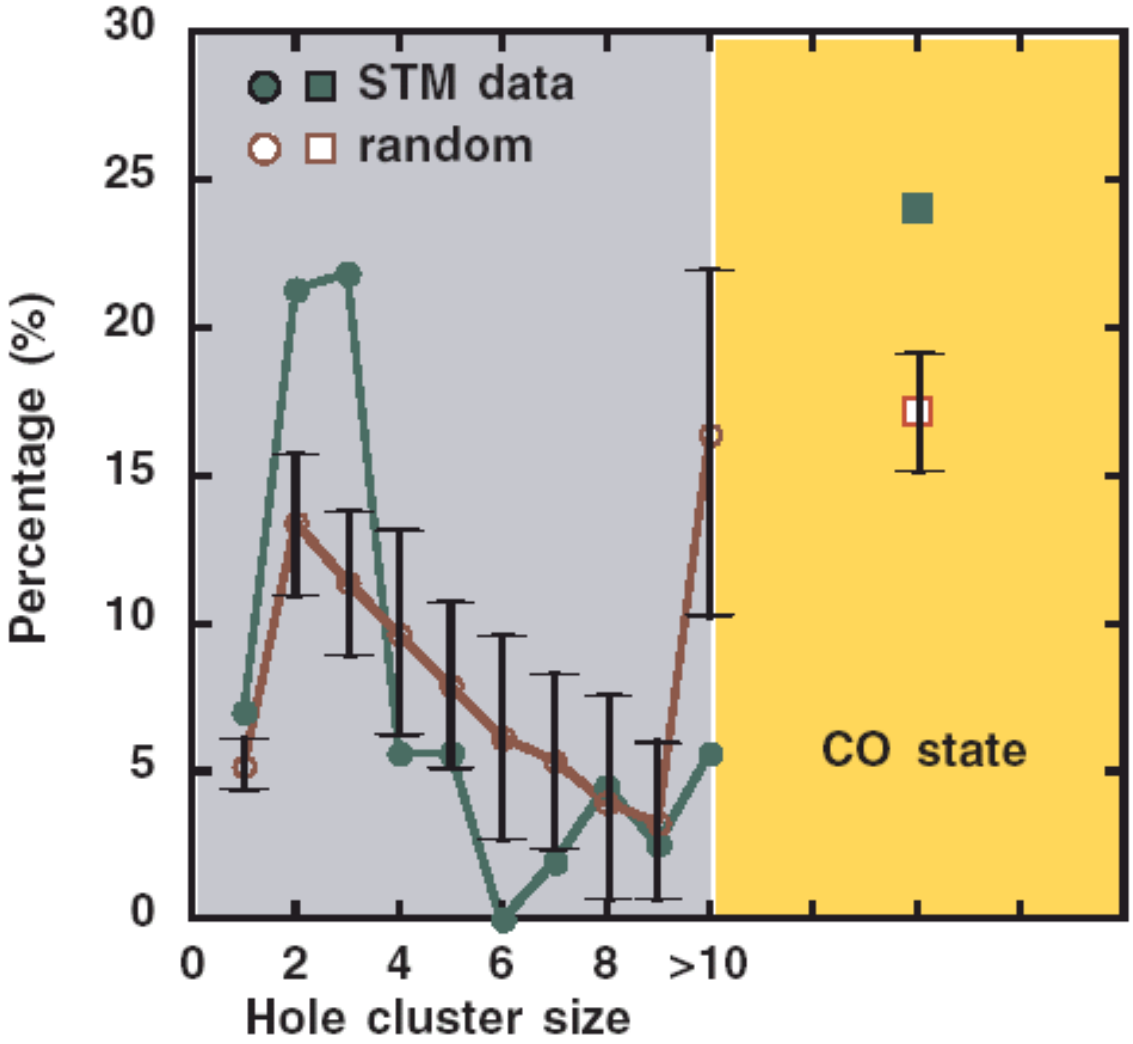

Figure 4.11: Distribution of holes forming the non-CO (left panel) and CO (right panel) clusters (normalized by total number of holes) obtained from Figure 4.10b, which is compared with that of a 2DRD with the same doping level. The error bars represent the standard deviations for the random distribution when using the same number of holes from the experimental data. In comparison to the random distribution, the localized holes show strong short-range correlation and a clear preference of forming nanoscale CE-type charge-order-like clusters.

clusters are preserved even in the paramagnetic state at a temperature that is well above the CO transition temperature, which is consistent with the previous x-ray scattering studies of manganites.[54] As a consequence of the hole localization, the hole mobility of the LPCMO film is very low, as will be described in the next section. An unanswered question remains as to whether the hole localization and the electronic inhomogeneity in the LPCMO film is spatially correlated to the doped divalent cations (Ca). This issue could be addressed by controlling the termination layer of the film.

4.2.3 Hole Mobility Measurement

It is important to confirm the presence of hole-based transport and the carrier density in the above film. To that end, we have performed a series of conductivity and Hall measurements on a similar film.

The Nb-doped STO substrate used in the STM measurements has a lower resistance than the LPCMO film, so it is impossible to measure the transport properties of those films directly. Instead, we have grown films on undoped STO with the same thickness under the same growth conditions. These films are then prepared for measurement in the PPMS system as discussed in Section 3.5.

The PPMS software is not specifically designed for performing Hall measurements, so a few minor tricks are necessary. The PPMS is configured for DC resistance measurements, with the sample mounted so that the current wires are connected to the outer I+ and I- electrodes shown in Figure 3.19. The output from the voltage sensing electrodes is read as a resistance, so the number must be multiplied by the excitation current to get the nominal Hall voltage.

As stated in Kittel[55], the Hall coefficient is then defined as

$$R_H \equiv \frac{E_y}{j_x B} = \frac{V_y}{D_y j_x B} \tag{4.1}$$

where B is the applied magnetic field, E_y is the transverse electric field, j_x is the excitation current density, V_y is the Hall voltage, and D_y is the distance between the Hall electrodes.

In terms of the full experimental parameters from the PPMS system, this simplifies to

$$R_H = \frac{R_y \cdot t \cdot D_x}{B \cdot D_y} \tag{4.2}$$

where R_y is the resistance in Ohms measured by the PPMS in the Hall configuration, t is the thickness of the film, D_x is the width of the film, and D_y is the distance between the Hall electrodes. Alternately, the slope from the resistance versus applied field can be substituted for R_y/B, as shown in Fig 4.12.

If a single carrier type is present, as in this case with the hole-doped manganites films, then the carrier concentration is given by

$$n = -\frac{1}{e \cdot R_H} \tag{4.3}$$

After performing this analysis for the 120nm LPCMO film at 300K, the observed carrier concentration is ~0.09 holes per Mn atom. This is an intriguing result, when

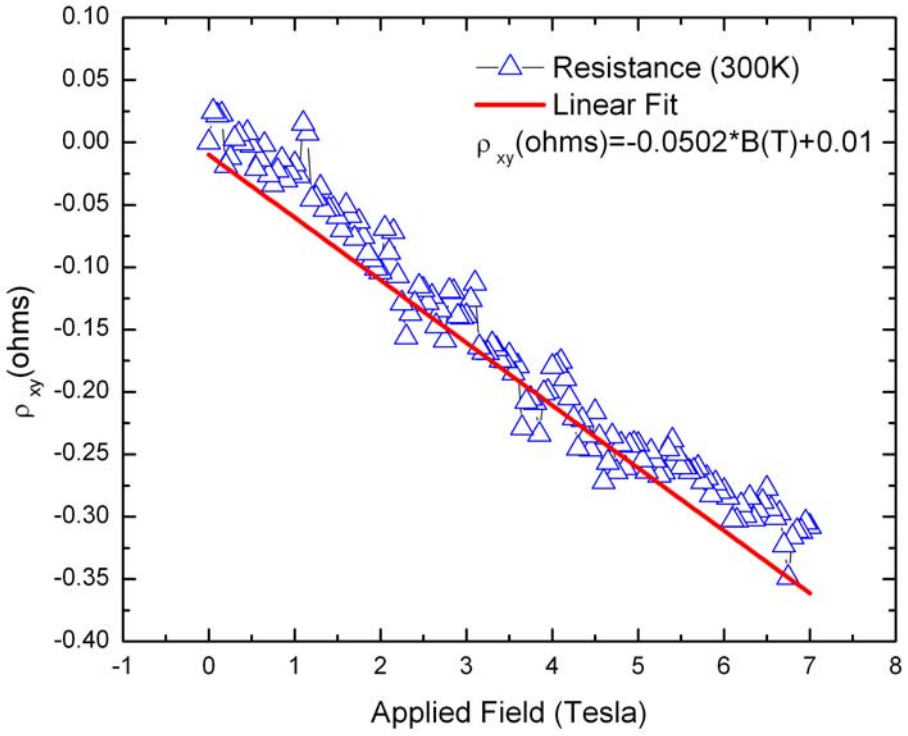

Figure 4.12: Hall resistance versus applied field for LPCMO thin film

viewed in combination with the results from the STM studies. Since the STM is able to resolve holes which are relatively static. The observed ratio of Mn^{4+}/Mn^{3+} was 0.45, which implies a static hole concentration of 0.31 holes per Mn atom, compared to the nominal doping level of 0.375 holes per Mn. If the missing holes are then assumed to be mobile and therefore observable by Hall measurements, then it is gratifying that the observed concentration of mobile holes correlates well with the missing holes from the STM images. Future studies can investigate this effect in greater detail.

4.3 Hematite Nanoparticles

As discussed in Section 2.3, the topic of antiferromagnetic nanoparticle magnetism is still the subject of some debate. There are several competing theories that seek to explain the behavior of the relatively large moment that is present in these samples. In this section, I will discuss our efforts to understand these effects.

4.3.1 Nanoparticle Growth

The specifics of the hematite particle growth are quite close to the general outline offered in Section 3.1.2. Both anhydrous ferric chloride (≥98%) and hydrochloric acid (GR) were purchased from EM Sciences. A stock solution containing 1.0M $FeCl_3$ and 0.2M HCl was prepared and used for all experiments. Therefore, all experiments were performed at fixed $FeCl_3$/HCl molar ratio 5:1. The particle size and shape are controlled by initial Fe^{3+} concentrations, reaction temperature and aging time. Hydrolysis experiments were performed in Teflon autoclaves (Parr acid digestion bomb) in static conditions. Two different nucleation processes were applied in the synthesis. For the slow nucleation process, the stock solution was diluted by deionized water to the desired Fe^{3+} concentration, then the solution was transferred into autoclave and placed in oven at set temperature. For the fast nucleation process, the stock solution was quickly poured into boiling water with vigorous stirring, and then the reaction mixture was rapidly transferred into autoclave and put into the oven at preset temperature. After the reaction is completed the particles were collected by centrifuge.

4.3.2 Characterization

The first issue in measuring the properties of antiferromagnetic nanoparticles is obtaining samples of sufficient quantity and quality to measure. Quantity is important since the SQUID magnetometer is a very sensitive instrument, but it still requires several milligrams of hematite powder to make a good measurement. Although significant advancements have been made during the last decade, there are relatively few antiferromagnetic materials that can be produced in nanometer-size samples.

The antiferromagnetic oxides are attractive candidates for measurement, since they are generally stable in air and can be grown as nanocrystals. The properties of the most common antiferromagnetic oxides are summarized in Table 4.2.

The primary antiferromagnetic nanoparticles to be properly synthesized and characterized for this project were hematite (α-Fe_2O_3). As discussed in Chapter 1, this is a common compound made from readily available components. It is quite inert and safe to handle. Growing small crystals is not trivial, but the necessary equipment and knowledge are well established. Some electron microscope images of the resulting particles are shown in Figures 4.13 through 4.15.

The first thing to notice in Figure 4.13 is the obvious faceting on the larger crystals in the bottom figure. This implies that they are single-crystals, which is confirmed by Figure 4.14, which is a transmission electron microscope (TEM) image of one of the crystallites. The lattice spacing and structure from Figure 4.14 correspond well with the literature values for hematite, which can be indexed as rhombohedral or hexagonal, with a = 5.04 Å and c = 13.72 Å.

Table 4.2: Common antiferromagnetic materials[56]

Compound	Crystal Symmetry	Néel Temperature	Moment Per Atom (μ_B)
CoO	Tetragonal	291	3.8
Cr_2O_3	Rhombohedral	307	3.0
FeO	Rhombohedral	198	3.32
α-Fe_2O_3	Rhombohedral	953	5.0
MnO	Rhombohedral	122	5.0
NiO	Rhombohedral	533-650	2.0
Mn	Cubic	95	

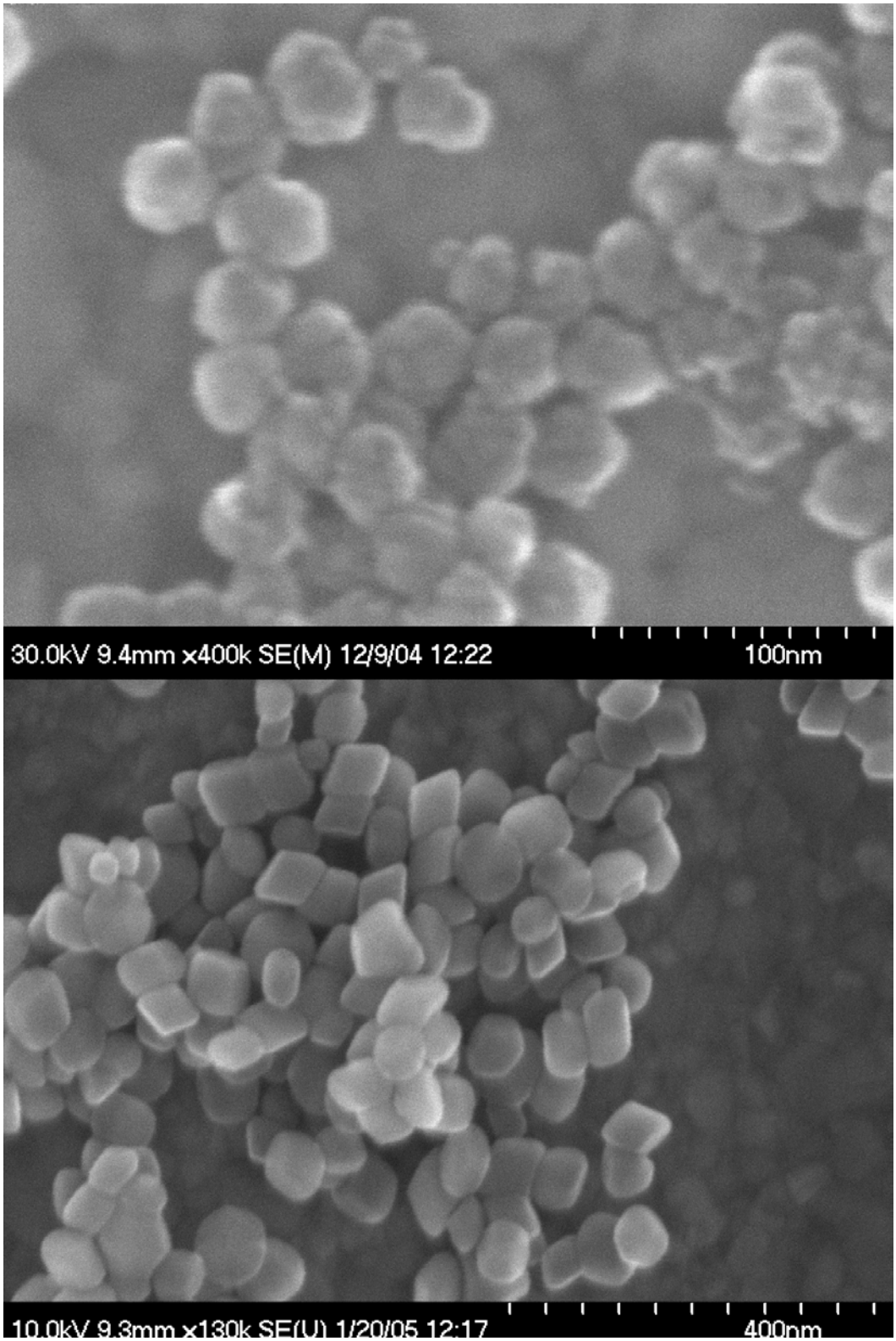

Figure 4.13: Hematite nanocrystals.

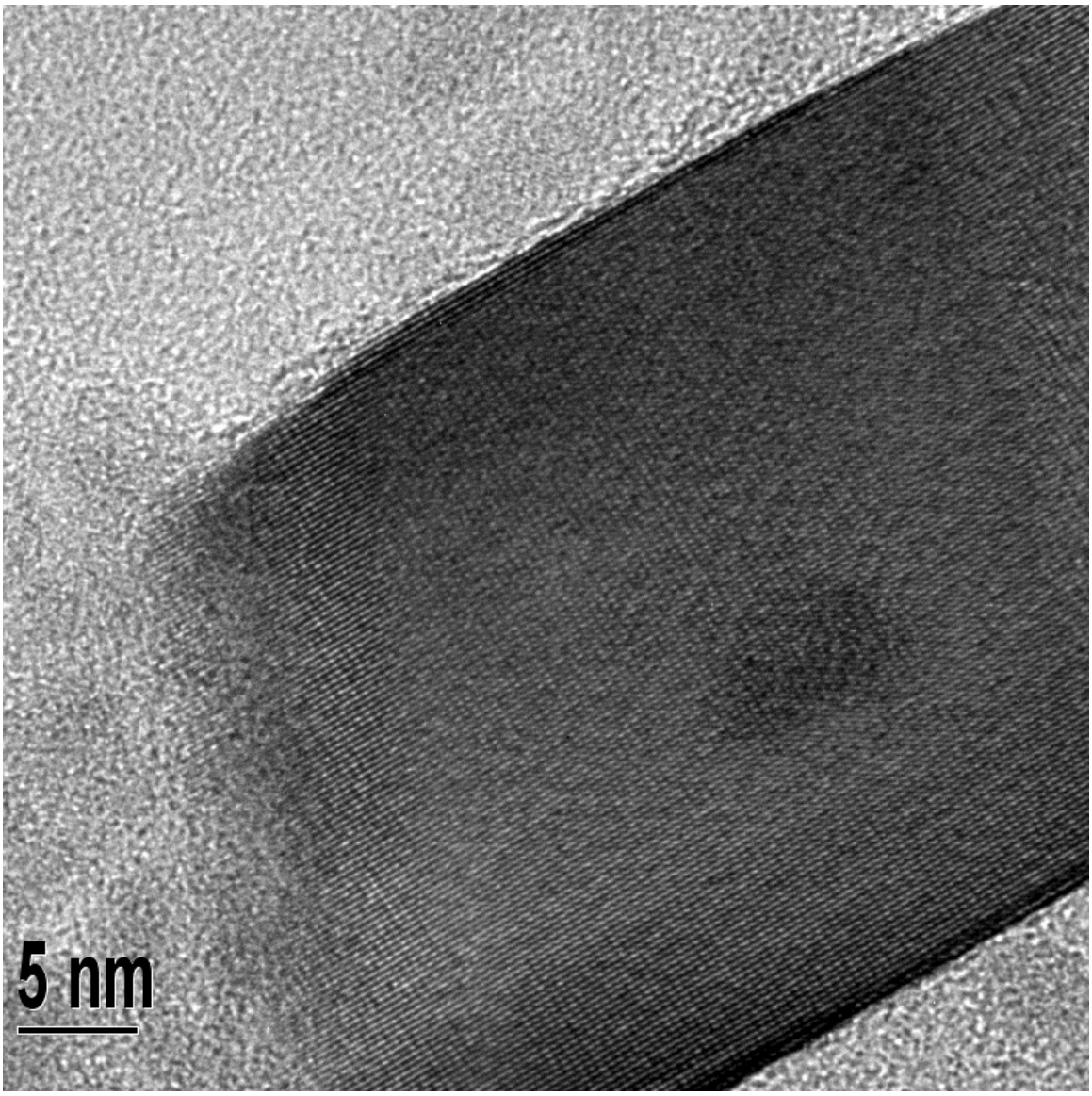

Figure 4.14: TEM image of 56nm hematite particle.

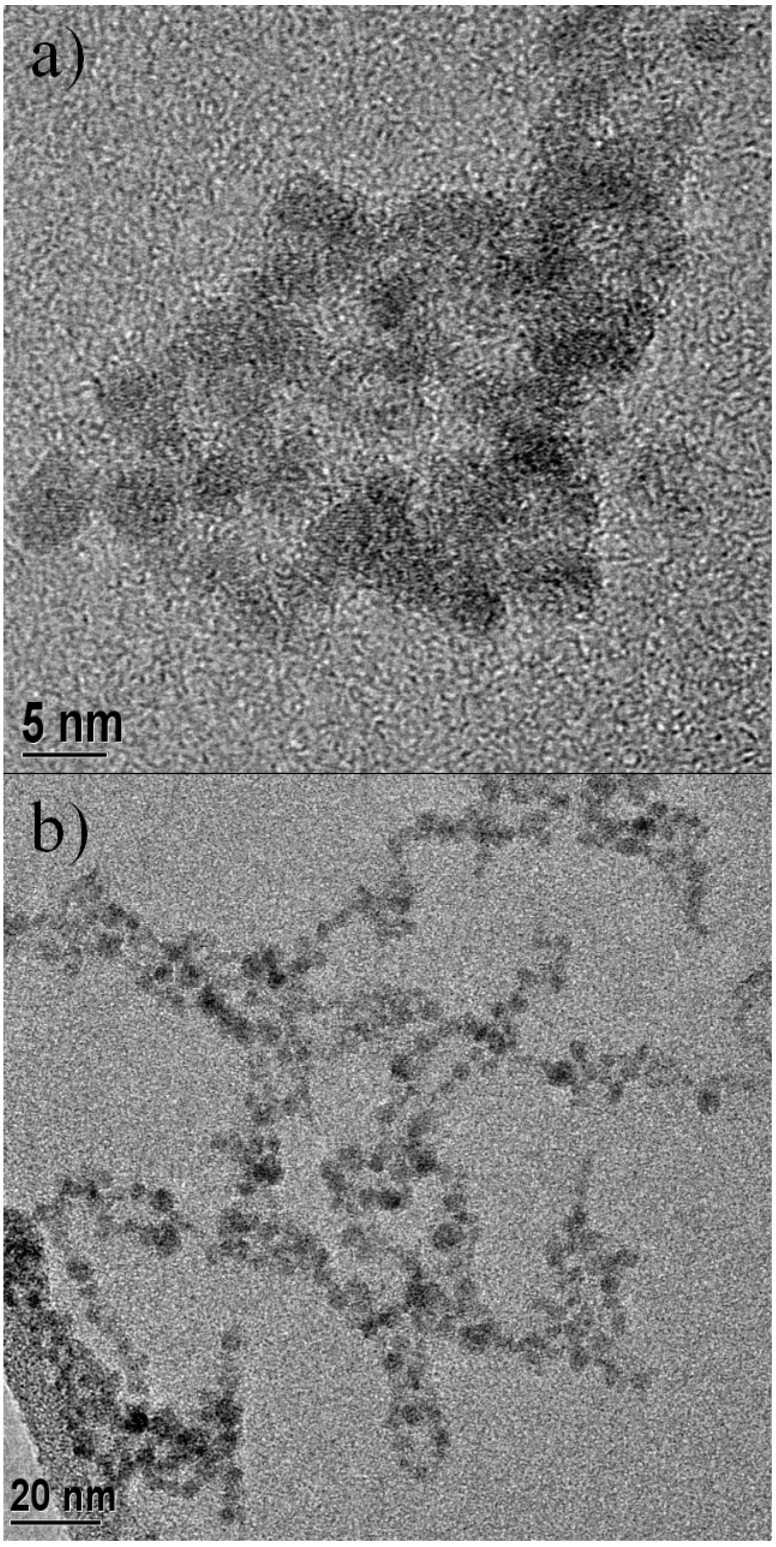

Figure 4.15: TEM images of 5nm particles a) closeup to show crystallinity b) wider view to show sizes.

Figure 4.15 shows two TEM images of the 5nm crystals. Although the image quality is not superb, the top figure shows clear lattice planes for most of the particles. The bottom figure is a wider view to emphasize the uniformity of the particle sizes.

This uniformity in particle size is one of the primary advantages of the solvo-thermal process detailed in Section 3.1.3. The particles can have a relatively narrow size distribution if the growth parameters are properly chosen. This is still not sufficient for our purposes, so some post-growth centrifugation and fractionation is necessary to improve the uniformity of the crystals.

Due to flocculation of the particles in the liquid suspension, the usual optical methods for determining particle sizes and size distributions were not particularly accurate for these samples. Therefore, it was necessary to resort to time-consuming scanning electron microscopy to characterize and sort the resulting samples. Figures 4.16 and 4.17 show the particle size distributions measured in the SEM for two of the best samples. Even with careful growth and post-treatment, the standard deviation in the particle size is still ten to twenty percent of the mean particle size.

The hematite nanoparticles show many of the behaviors typical of superparamagnetic systems, which were covered in Section 2.3.1. Figure 4.18 shows a moment versus temperature curve for the 5nm nanoparticles where the zero-field cooled curve and field cooled curves diverge at the blocking temperature. Note that the total moment of the sample *decreases* with temperature, which would seem to contradict the predictions of references [6] and [2]. The total moment of the sample is expected to be a combination of the bulk antiferromagnetic moment and the surface ferromagnetic (or ferrimagnetic) moment. In addition to these two effects, there is also the diamagnetic

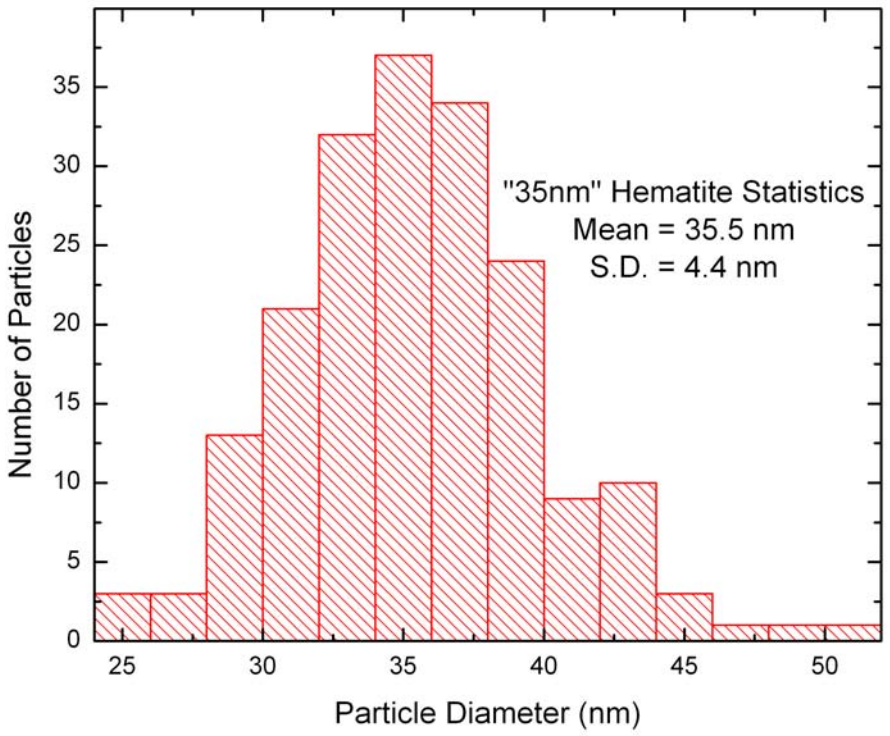

Figure 4.16: Statistics for "35nm" hematite particles.

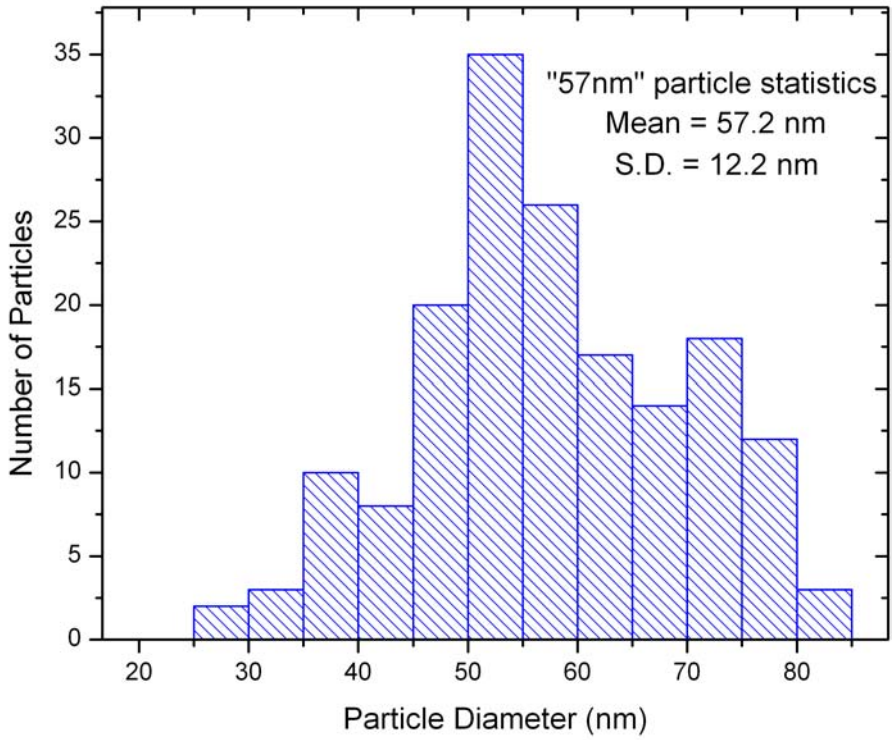

Figure 4.17: Particle statistics for "57nm" hematite particles.

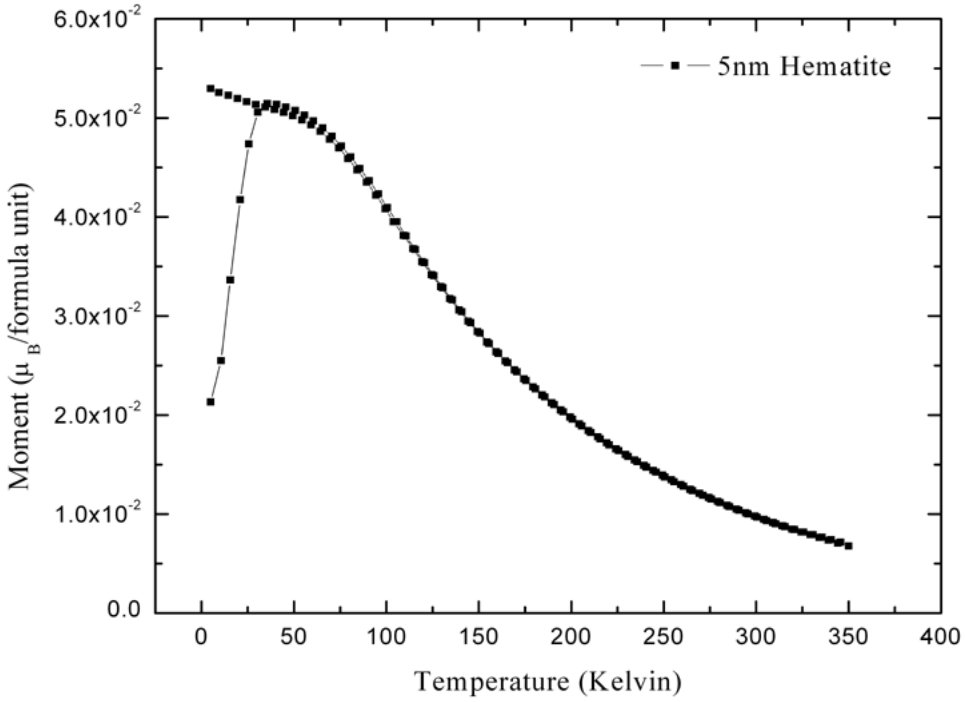

Figure 4.18: Blocking behavior of 5nm hematite particles.

behavior of the sample holder.

These overlapping effects are also visible in the magnetic moment versus applied field curves measured from the same sample, which are shown in Figure 4.19. The room temperature (300K) loop shows no hysteresis and no saturation up to 7 Tesla. The loop at 50 Kelvin shows an increased moment, but still no saturation or hysteresis. Well below the blocking temperature, as in the 2 Kelvin plot, there is substantial hysteresis. Figure 4.20 shows the moment versus temperature curves for samples in several different size regimes. As expected, the 5nm particle samples have the largest moment, which is entirely consistent with Néel prediction of uncompensated surface spins. The blocking temperature is higher for the 35nm diameter sample, as predicted in Section 2.3. However, the most striking feature occurs in the bottom curve, which shows the behavior of the 56nm particles. In this case, the low-temperature susceptibility is quite low. At 240 Kelvin the sample goes through a transition to a high susceptibility state. In addition, the room temperature moment is approximately the same for all samples. This transition is known as the Morin transition, and it is a peculiar property of the hematite itself. A

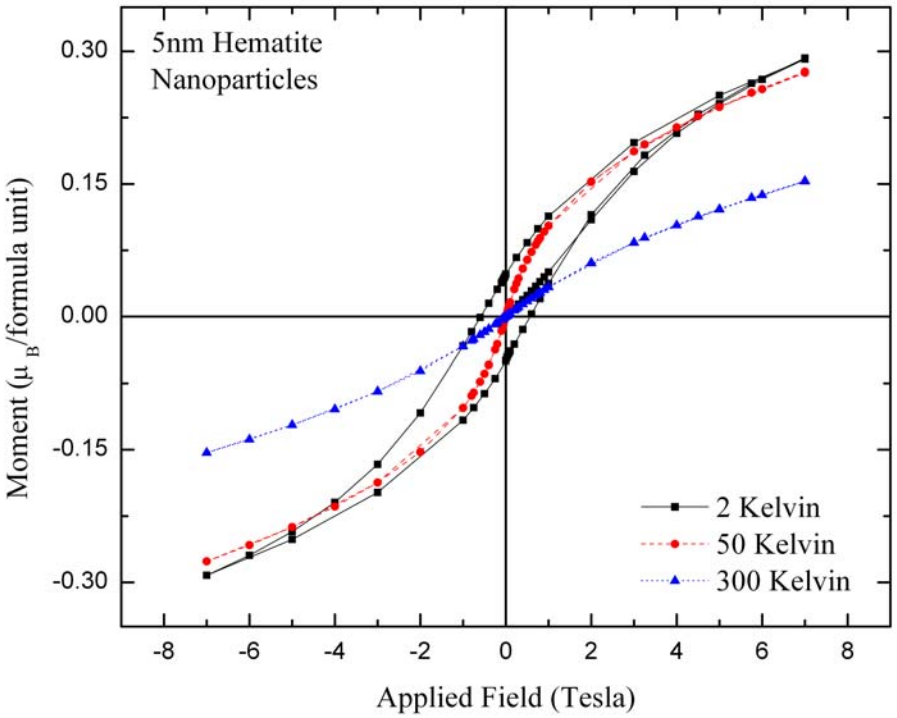

Figure 4.19: Hysteresis loops for 5nm hematite nanoparticles.

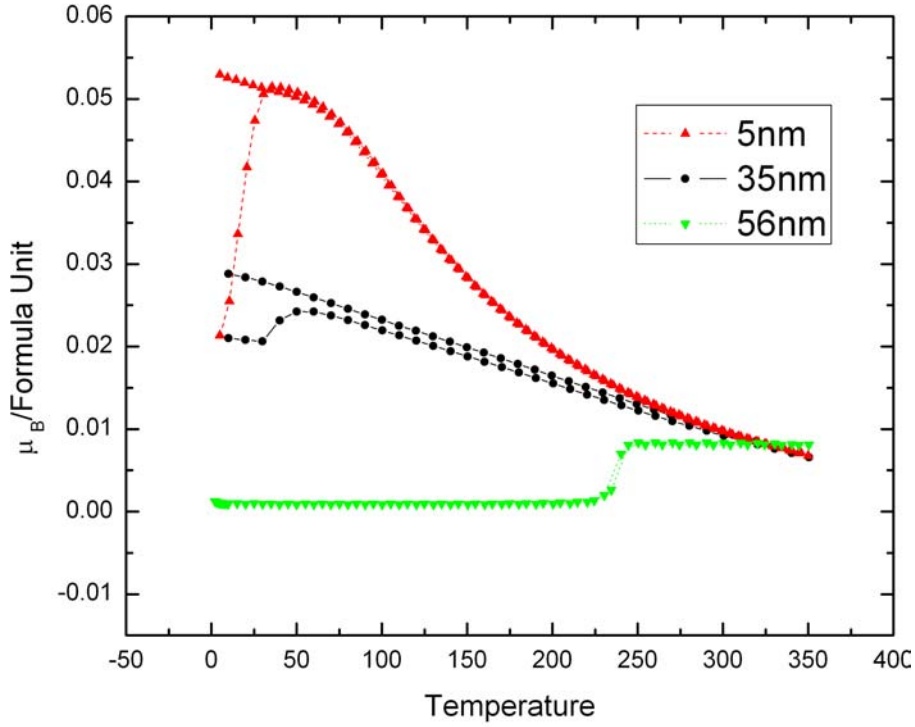

Figure 4.20: Combined moment versus temperature curves.

brief discussion of the history and physics of the Morin transition is included in Appendix B.

The Morin transition is actually a transition from a fully antiferromagnetic state at low temperature to a canted antiferromagnetic state at high temperature.[57] Figures 4.21 through 4.23 are more complete moment versus temperature scans for the three samples shown in Fig 4.20. In Figure 4.21, it is interesting to note that the onset temperature of the Morin transition changes as a function of the applied field. No such change is observed in the 5nm or 35nm samples shown in Figures 4.22 and 4.23.

This result draws into question exactly what is the magnetic state of the smallest particles. The complete lack of an observable Morin transition, coupled with the convergence at high temperature of the particle moments per formula unit, implies that the smaller particles are permanently in the canted antiferromagnetic state. This is

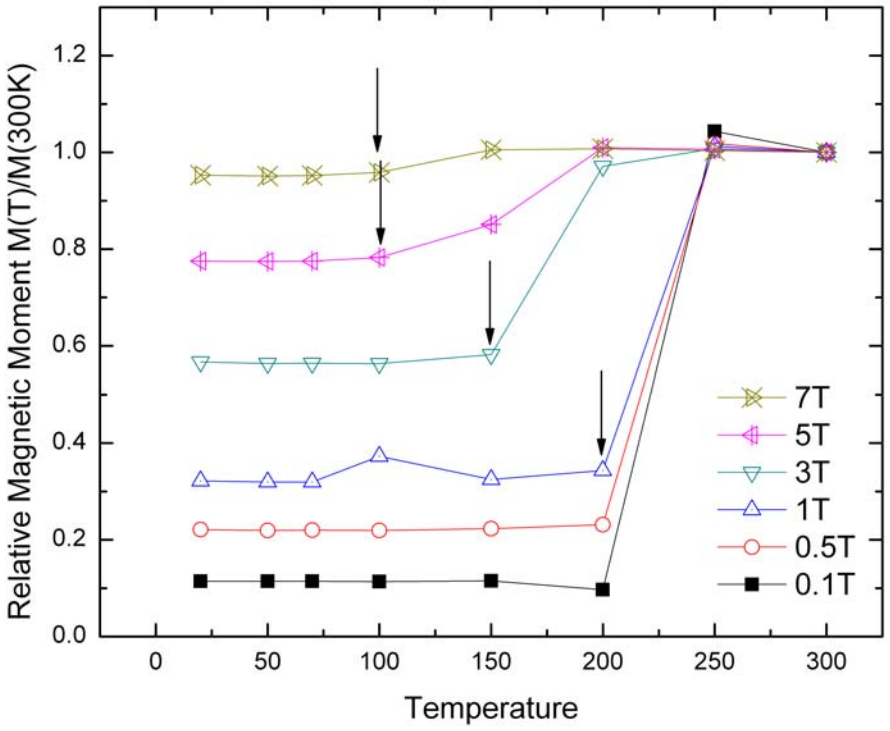

Figure 4.21: 56nm hematite relative moment versus temperature. The arrows indicate the beginning of the Morin transition.

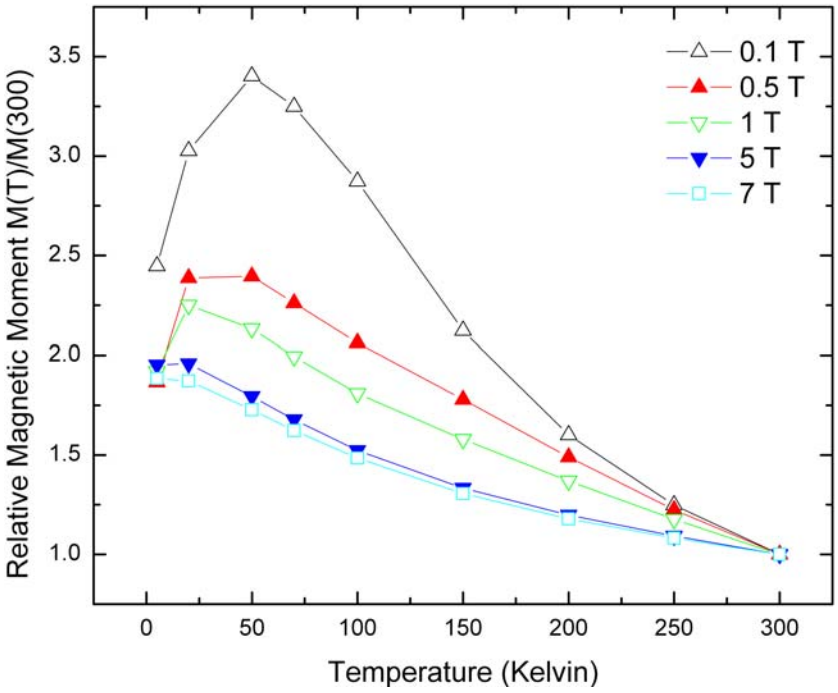

Figure 4.22: Relative moment for 5nm hematite particles.

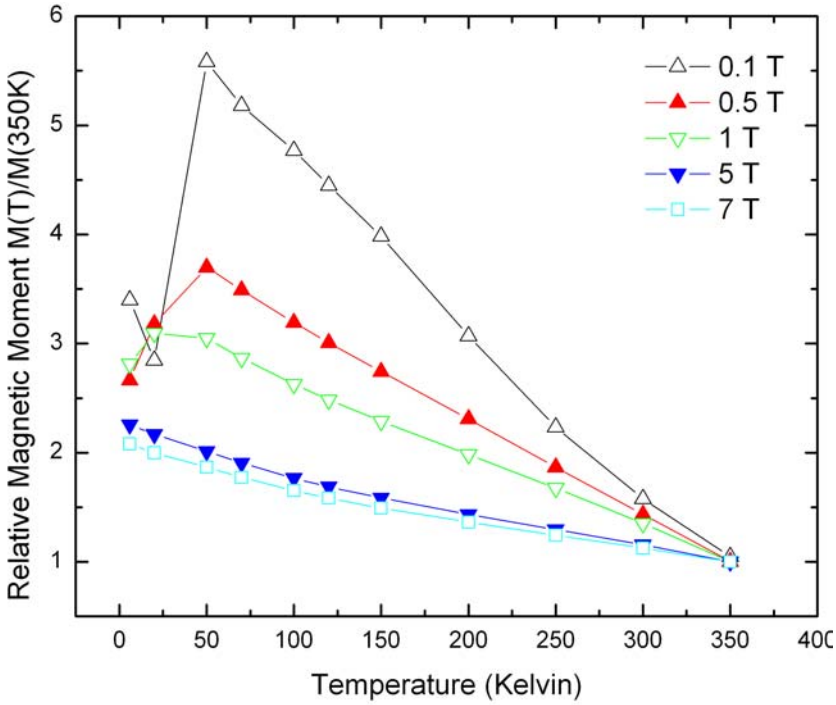

Figure 4.23: Relative moment for 35nm hematite nanoparticles.

consistent with the results of Ref. [58], where the Morin temperature decreased with decreasing particle size. It seems that the transition from bulk-like Morin behavior to a permanent canted state occurs between 35 and 56 nm.

4.3.2 Fitting results

In order to try and resolve the various competing effects, it is necessary to resort to more advanced methods. The easiest and most common approach is to try to use the Langevin equation derived in Appendix A.

$$M = N\mu_p[\coth(\frac{\mu_p H}{k_B T}) - \frac{k_B T}{\mu_p H}] = N\mu_p L(\frac{\mu_p H}{k_B T}) \tag{4.4}$$

where M is the total moment of the sample, N is the number of particles, and μ_p is the moment per particle.

This is will account for the behavior of the ferromagnetic component of the overall moment of the particles. It is also necessary to add a linear term to account for the antiferromagnetic bulk and the diamagnetic sample holder. This is the fitting scheme used by Seehra et al to determine the moment in ferrihydrite nanoparticles.[16] Their observation of an increasing moment versus temperature was used by Morup and Frandsen as a major justification for their thermoinduced moment theory. The full fitting equation is then:

$$M = N\mu_p L(\frac{\mu_p H}{k_B T}) + \chi_{AF} H \tag{4.5}$$

In order to use it, it is necessary to take measure the zero-field cooled initial magnetization curves at various temperatures, and perform the fitting at each temperature. The fitting will then yield values for μ_p, N, and χ_{AF}.

Figure 4.24 shows an example of an initial magnetization curve taken at 250 Kelvin for a sample with 35nm average particle diameter. The red curve is the result of a least-squares fitting routine using equation 4.5. The resulting fit parameters are shown in the figure. As stated above, the values for particle number, particle moment, and antiferromagnetic susceptibility can then be collected as a function of temperature. For our purposes, the most interesting parameter is the particle moment. The results for the

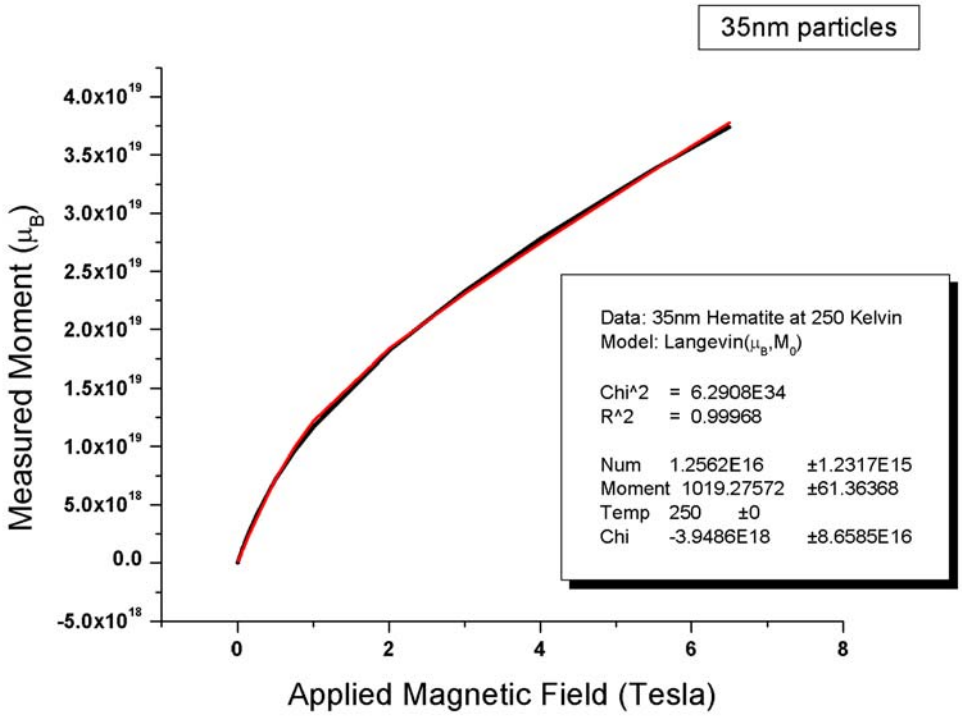

Figure 4.24: Initial magnetization curve (black) and Langevin model fit (red) for 35nm particles.

5nm and 35nm particles are shown in Figures 4.25 and 4.26. An increasing moment versus temperature is indeed observed for both samples. The fitting error is quite small, especially at lower temperatures. Interestingly enough, superparamagnetic effects seem to play no role in the behavior, as there is no substantial change below the blocking temperature at 50 Kelvin. The moment starts from zero at very low temperatures and increases almost linearly, saturating at approximately 200K. This linear increase is very similar to that observed in ferrihydrite by Seehra.[16] The near-zero intercept is perplexing, however. According to the thermo-induced moment picture from Morup and Frandsen, the zero-temperature moment should be strictly due to the uncompensated spins. This would imply that there are no uncompensated spins. If true, this would be an astonishing result, but it is not consistent with the earlier observation of the enhanced moment in 5nm particles versus the 35nm particles.

As stated above, this fitting procedure is relatively common, but it is somewhat controversial. The assumptions in the original derivation were not particularly realistic,

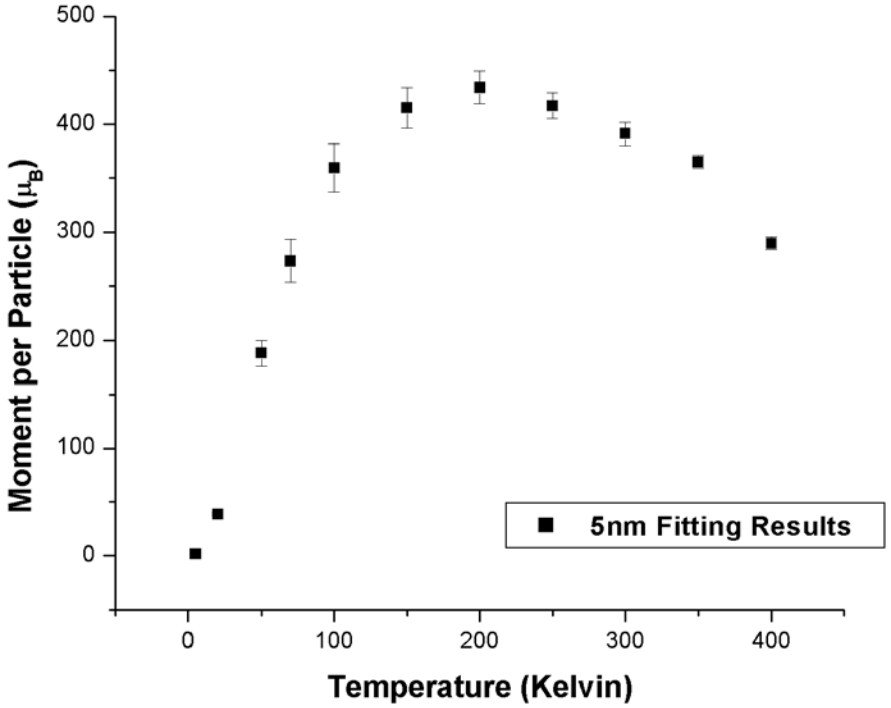

Figure 4.25: 5nm hematite particle moment versus temperature from first fitting procedure.

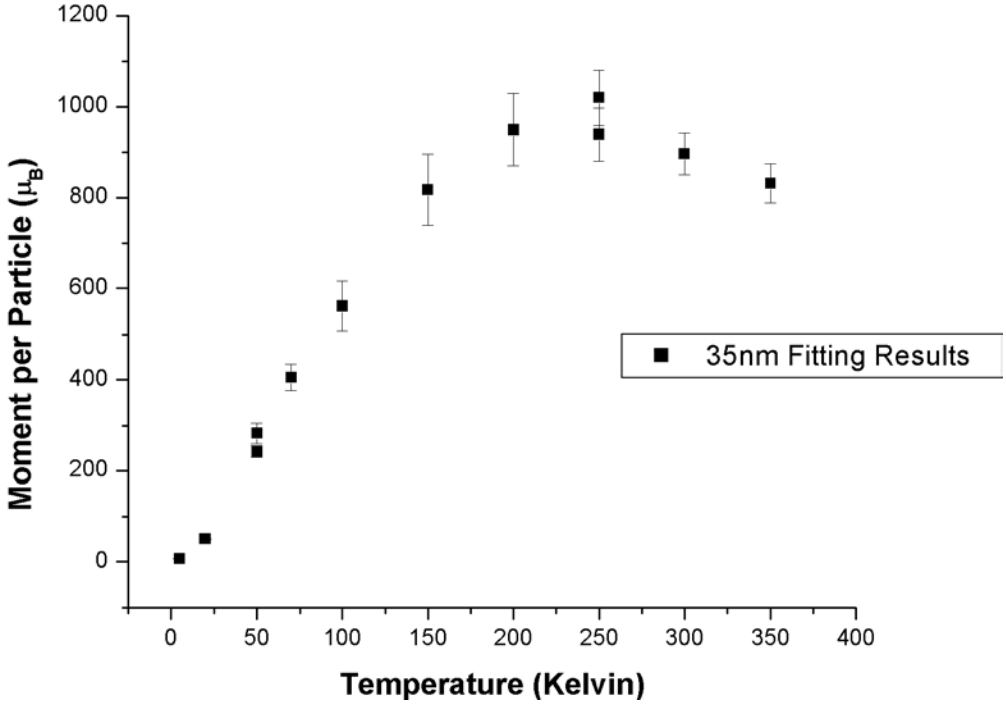

Figure 4.26: 35nm hematite particle moment versus temperature.

so it is not surprising that there are signs of a possible breakdown.

The most glaring deficiency is the assumption of complete uniformity in the particle moments. Figures 4.16 and 4.17 prove that the *size* distribution is non-uniform, so there is no reason to believe that *moment* distribution is uniform. In point of fact, in an article written by Silva et al, they pointed out that a fitting procedure involving a non-uniform distribution in moments is much more appropriate.[8] In addition, they performed just such an analysis on antiferromagnetic nanoparticles which were chosen to be very similar to those in the paper written by Seehra et al which had shown an *increasing* moment versus temperature.[16] The distributed moment results imply that the moments *decrease* with increasing temperature.

The relevant formula is

$$M(H,T) = N\int_{\mu_{\min}}^{\mu_{\max}} \mu L(\frac{\mu H}{kT}) f(\mu) d\mu + \chi_{AF}(T) H \,, \tag{4.6}$$

where μ is the particle moment and f(μ) is the normalized log-normal distribution.

$$f(\mu) = \frac{1}{\mu \cdot s\sqrt{2\pi}} \exp\{-\frac{[\log(\frac{\mu}{n})]^2}{2s^2}\} \tag{4.7}$$

S^2 is the variance in the log-normal function. The average particle moment is then

$$< \mu >= n\sqrt{\exp(s^2)} \,. \tag{4.8}$$

After some consultation with Dr. Silva, I used his fitting procedure to analyze the results for the hematite particles. The resulting particle moments, normalized to their value at 300K, are shown in Figures 4.27 and 4.28. The increased number of fitting parameters actually leads to a smaller calculated fitting error, but I have manually increased the size of the error bars in order to be cautious. In any case, each curve has interesting features.

The 5nm curve is difficult to interpret. Given my conservative error bars, it is possible to imagine that it shows a linear increase or a transition at 100K, at which point the moment increases rapidly until 250 Kelvin. Recall that Figures 4.18 and 4.22 show that the overall moment decreases with temperature, while the earlier fitting procedure shows a linear increase and saturation. Maybe some of the larger particles are not in the

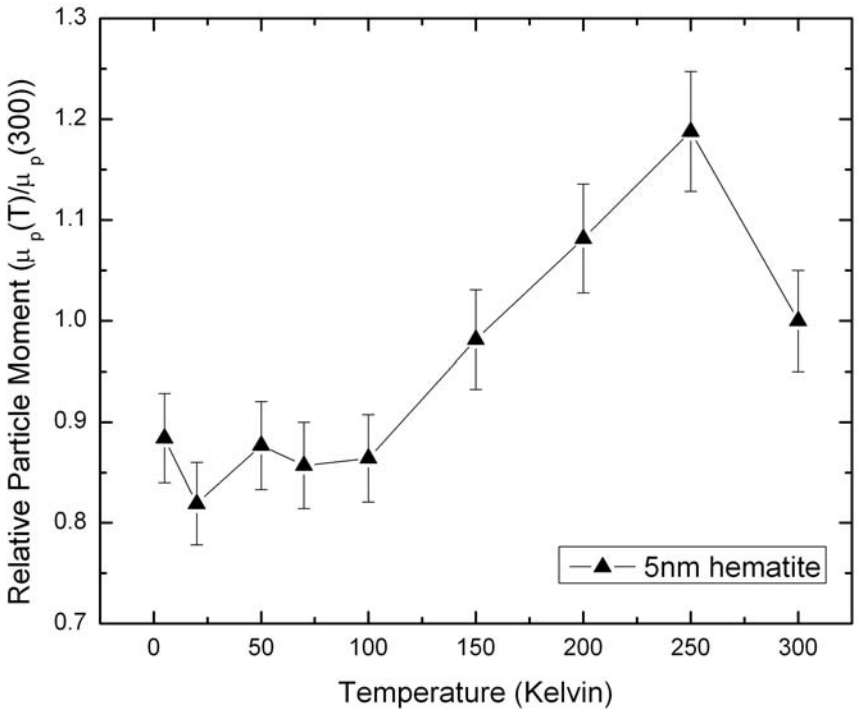

Figure 4.27: 5nm hematite distributed moment fitting results.

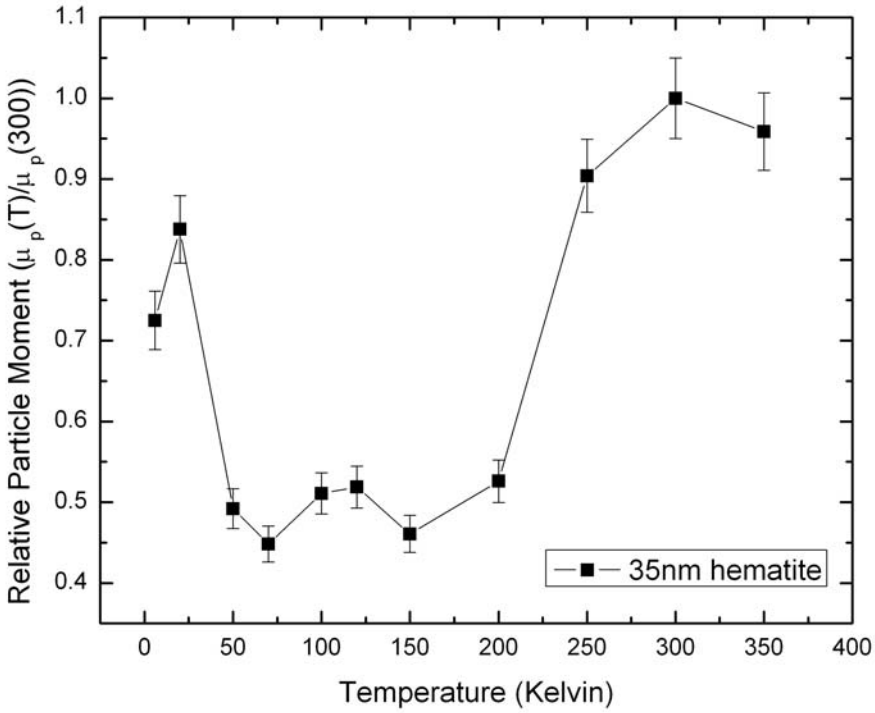

Figure 4.28: 35nm hematite distributed moment fitting results.

canted state at low temperature, but instead undergo a Morin transition starting at 100K.

The same logic might hold for the 35nm particles. The low temperature behavior might be due to blocking effects, followed by a comparable low moment regime and a rapid increase which bears a suspicious resemblance to the Morin transition. Here again, perhaps we are resolving some extremely small fraction of the particles which are not canted at low temperature but do not possess a large enough moment to show up in the earlier measurements.

Chapter 5 Conclusions and Future Directions

The results in the previous chapter clearly show some of the complex behavior in the transition metal oxides, as well as how our efforts at using spatial confinement as a tool have begun to bear fruit, but they also show that a large amount of work remains to be done.

The large changes in magnetoresistance in the LPCMO thin films caused by small changes in the substrate are impressive, but more data would make a stronger case for the influence of strain on phase separation. In particular, I think that the films on SLGO (negligible strain) and NGO (small tensile strain) are interesting, and I think it is important to get results for more films on these substrates. In addition, it is now possible to do more advanced x-ray reciprocal space maps, which can really show how the strain field changes through the thickness of the film. Figure 5.1 is an example of this, which shows how the base of the film is highly strained, but the strain has almost relaxed at the top of the film. In order to do a more exhaustive version of this experiment, full strain plots could be done for every sample, leading to a more complete picture.

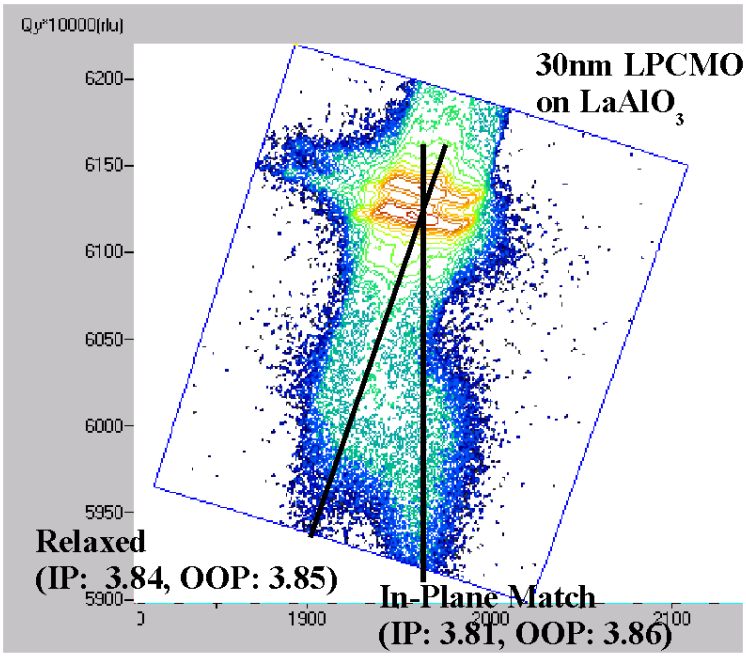

Figure 5.1: Reciprocal space map for 30nm LPCMO film on $LaAlO_3$.

Since disorder is believed to be a primary factor in phase separation, it would be useful to create artificially ordered films with the same overall stoichiometry and structure as the disordered films. Work is already commencing in this direction, as shown in the x-ray plot in Figure 5.2. In this case, an ordered superlattice of LCMO/PCMO films have been grown on a $SrLaGaO_4$ substrate, and the evidence shows up as two side peaks next to the film peak.

Another means of probing the physics of the manganites is to change the dimension of the sample. The thin films are two-dimensional, in the sense that they are constrained in thickness but not in either of the lateral dimensions. If the sample is modified so that one of the lateral dimensions is also constrained, then that region of the sample would be come one-dimensional or wire-like. As stated in Section 2.4.3, reducing the dimension of the sample changes the concentration of percolation sites that are necessary for conduction. If the length scale of the phase separation in a manganite wire is comparable to the width of the wire, then the effective dimension for percolation goes from two to one, with a correspondingly large change in the transport properties.

Figure 5.3 shows a schematic of this idea. I have taken part in the effort to pattern wires from thin films, and I am hopeful that these efforts will be soon be successful. Figure 5.4 shows just how close we are to succeeding.

Finally, the results from the hematite particle experiments are much more troubling. The distributed moment analysis, coupled with the other experimental data, seems to indicate that the particles are never in a truly antiferromagnetic state and are therefore a poor test case for thermoinduced magnetization. In light of those results, I have attempted to obtain other types of antiferromagnetic nanoparticles without success. However, there are hints that our collaborators may soon find a solution. Figure 5.5 shows an example of metallic chromium particles encapsulated in SiO_2. Once these samples are grown, I feel confident that the tools for measurement and analysis exist to really answer the questions properly.

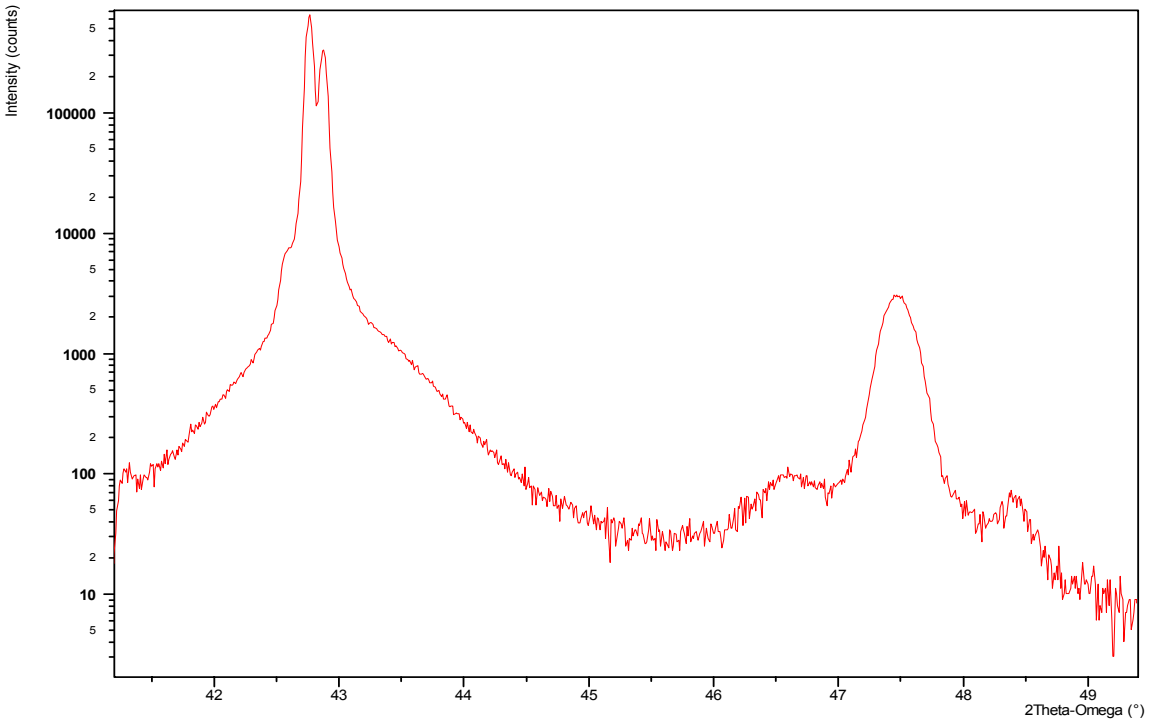

Figure 5.2: Diffraction plot of LCMO/PCMO multilayer sample.

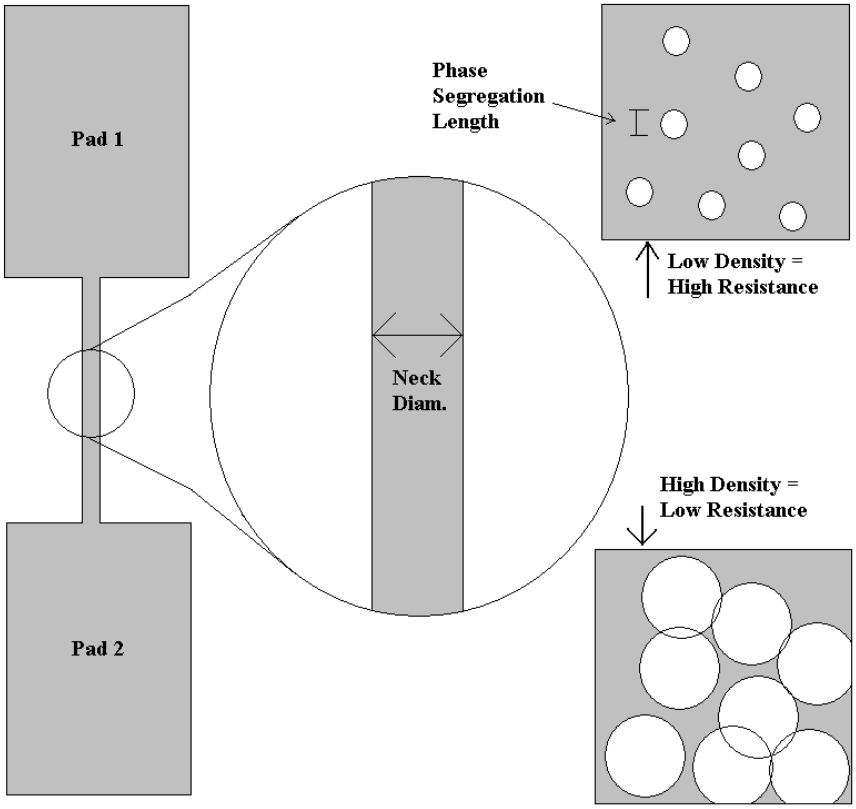

Figure 5.3: Schematic of phase separation effects in nanowire.

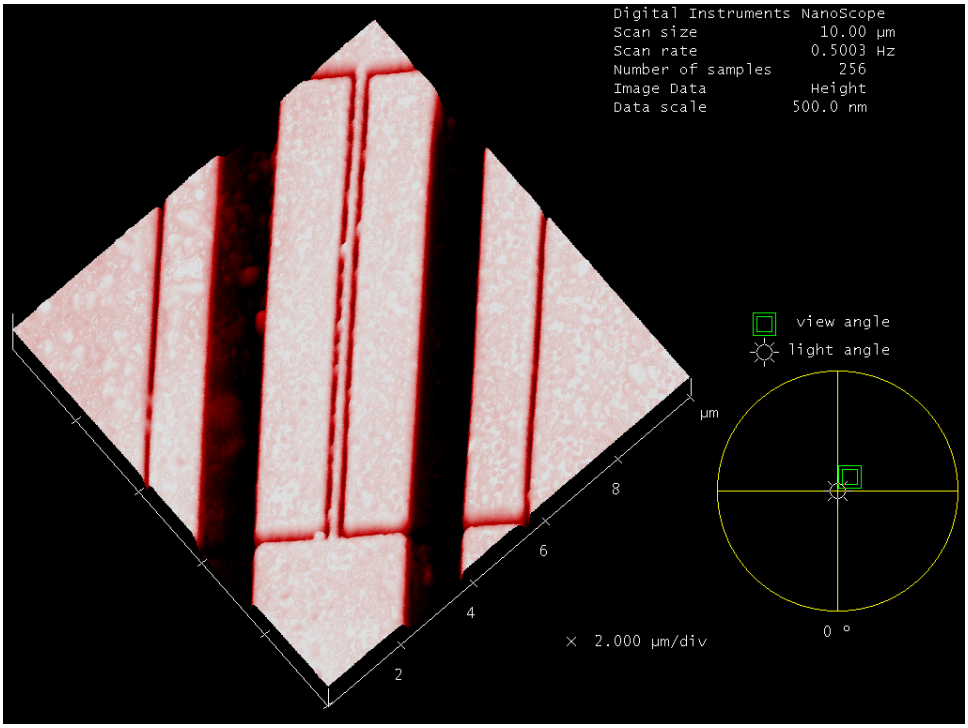

Figure 5.4: Early nanowire sample. Wire extends from bottom of picture to top.

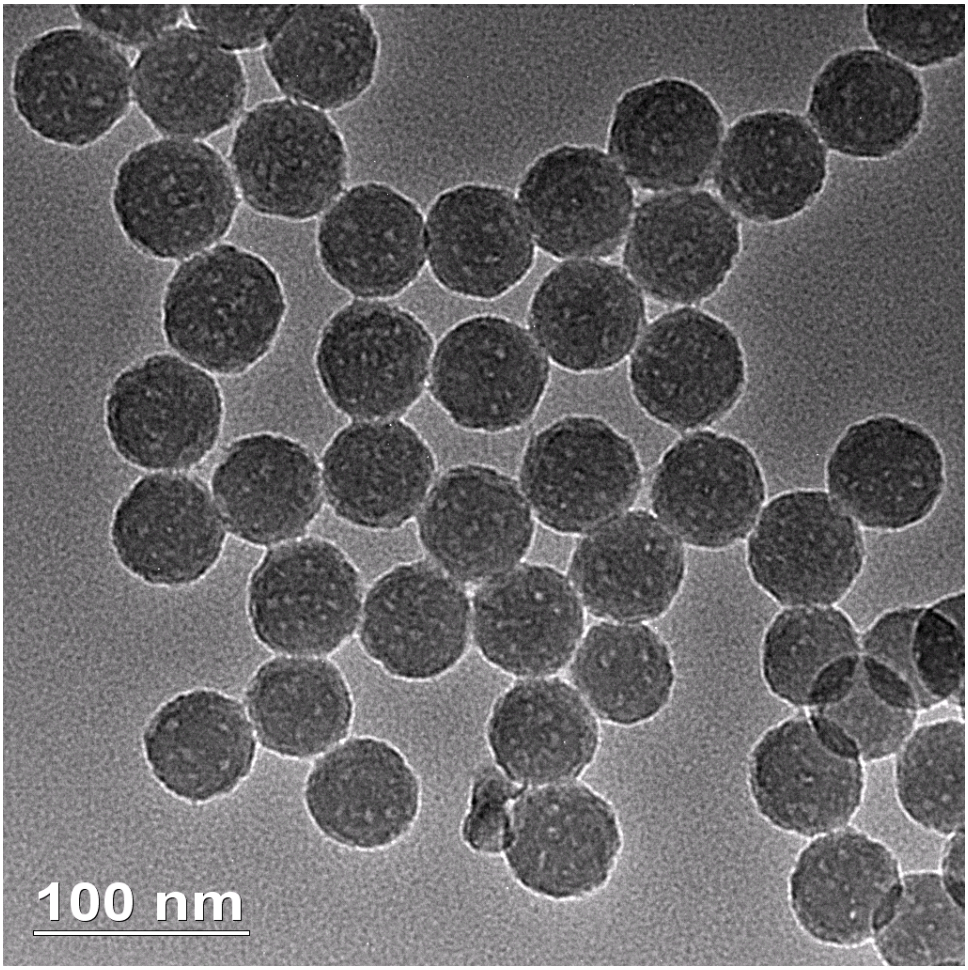

Figure 5.5: SiO_2-encapsulated Chromium particles.

References

References

1. Néel, L., Seances Acad. Sci., 1949. **228**: p. 664.
2. Brown, G., et al., *Intrinsic volume scaling of thermoinduced magnetization in antiferromagnetic nanoparticles.* Physical Review B, 2005. **72**(14): p. 140405.
3. Gilles, C., et al., *Non-Langevin behaviour of the uncompensated magnetization in nanoparticles of artificial ferritin.* European Physics Journal B, 2000. **17**: p. 417-427.
4. Harris, J.G.E., et al., *Excess spin and the dynamics of antiferromagnetic ferritin.* Physical Review B, 1999. **60**(5): p. 3453-3456.
5. Makhlouf, S.A., F.T. Parker, and A.E. Berkowitz, *Magnetic hysteresis anomalies in ferritin.* Physical Review B, 1997. **55**(22): p. R14717-R14720.
6. Morup, S. and C. Frandsen, *Thermoinduced magnetization in nanoparticles of antiferromagnetic materials.* Physical Review Letters, 2004. **92**: p. 217201.
7. Morup, S. and B.R. Hansen, *Uniform magnetic excitations in nanoparticles.* Physical Review B, 2005. **72**: p. 024418.
8. Silva, N.J.O., V.S. Amaral, and L.D. Carlos, *Relevance of magnetic moment distribution and scaling law methods to study the magnetic behavior of antiferromagnetic nanoparticles: Application to ferritin.* Physical Review B, 2005. **71**(18): p. 184408.
9. Ahn, K.H., T. Lookman, and A.R. Bishop, *Strain-induced metal-insulator phase coexistence in perovskite manganites.* Nature, 2004. **428**: p. 401 - 404.
10. Dagotto, E., *Nanoscale Phase Separation and Colossal Magnetoresistance: The Physics of Manganites and Related Compounds*. First ed. Springer Series in Solid-State Sciences, ed. P.F. M. Cardona, K. Von Klitzing, and H-J. Queisser. Vol. 136. 2003, Berlin: Springer Verlag. 456.
11. Griffiths, D.J., *Introduction to Electrodynamics*. Third ed. 1999, Upper Saddle River, NJ: Prentice Hall.
12. Reitz, J., F. Milford, and R. Christy, *Foundations of Electromagnetic Theory*. Fourth ed. 1993, Reading, MA: Addison-Wesley Publishing.
13. Jackson, J.D., *Classical Electrodynamics*. Third ed. 1999, New York: John Wiley and Sons, Inc.
14. Skomski, R. and J.M.D. Coey, *Permanent Magnetism*. Condensed Matter Physics. 1999, Bristol: Institute of Physics Publishing. 404.
15. Chikazumi, S., *Physics of Ferromagnetism*. The International Series of Monographs on Physics. 1997, Oxford, UK: Clarendon Press.
16. Seehra, M.S., et al., *Neutron scattering and magnetic studies of ferrihydrite nanoparticles.* Physical Review B, 2000. **61**(5): p. 313-3518.
17. Jonker, G.H. and J.H.v. Santen, *Ferromagnetic compounds of manganese with perovskite structure.* Physica, 1950. **16**(3): p. 337-349.
18. Santen, J.H.v. and G.H. Jonker, *Electrical conductivity of ferromagnetic compounds of manganese with perovskite structure.* Physica, 1950. **16**(7-9): p. 599-600.

19. Volger, J., *Further Experimental Investigations on some Ferromagnetic Oxidic Compounds of Manganese with Perovskite Structure.* Physica, 1954. **20**: p. 49 - 56.
20. Zener, C., *Interaction between the d shells in the transition metals.* Physical Review, 1951. **81**(4): p. 440-444.
21. Zener, C., *Interaction between the d-shells in the transition metals II. Ferromagnetic compounds of manganese with perovskite structure.* Physical Review, 1951. **82**(3): p. 403-405.
22. Zener, C., *Interaction between the d-shells in the transition metals III. Calculation of the Weiss factors in Fe, Co, and Ni.* Physical Review, 1951. **83**(2): p. 299-301.
23. Anderson, P.W. and H. Hasegawa, *Considerations on Double Exchange.* Physical Review, 1955. **100**(2): p. 675-681.
24. Wollan, E.O. and W.C. Koehler, *Neutron diffraction study of the magnetic properties of the series of perovskite-type compounds [(1-x)La, xCa]MnO_3.* Physical Review, 1955. **100**(2): p. 545-563.
25. Helmolt, R.V., et al., *Giant negative magnetoresistance in perovskite-like La2/3Ba1/2MnOx Ferromagnetic Films.* Physical Review Letters, 1993. **71**(14): p. 2331-2333.
26. Kusters, R.M., et al., *Magnetoresistance Measurements on the Magnetic Semiconductor Nd0.5Pb0.5MnO3.* Physica B, 1989. **155B**: p. 362.
27. Jin, S., et al., *Thousandfold change in resistivity in magnetoresistive La-Ca-Mn-O Films.* Science, 1994. **264**: p. 413-415.
28. Dagotto, E., T. Hotta, and A. Moreo, *Colossal Magnetoresistant Materials: The Key Role of Phase Separation.* Physics Reports, 2001. **344**: p. 1-153.
29. Ramirez, A.P., *Colossal Magnetoresistance.* Journal of Physics, Condensed Matter, 1997. **9**: p. 8171-8199.
30. Salamon, M.B. and M. Jaime, *The Physics of Manganites: Structure and Transport.* Reviews of Modern Physics, 2001. **73**: p. 583-628.
31. Ziese, M., *Extrinsic magnetotransport phenomena in ferromagnetic oxides.* Reports on Progress in Physics, 2002. **65**: p. 143-249.
32. Uehara, M., et al., *Percolative phase separation underlies colossal magnetoresistance in mixed-valent manganites.* Nature, 1999. **399**: p. 560-563.
33. Faeth, M., et al., *Spatially Inhomogeneous Metal-Insulator Transition in Doped Manganites.* Science, 1999. **285**: p. 1540.
34. Dho, J., I. Kim, and S. Lee, Physical Review B, 1999. **60**: p. 14545.
35. Lynn, J.W., et al., *Unconventional ferromagnetic transition in La1-xCaxMnO3.* Physical Review Letters, 1996. **76**(21): p. 4046-4049.
36. Burgy, J., et al., *Colossal Effects in Transition Metal Oxides Caused by Intrinsic Inhomogeneities.* Physical Review Letters, 2001. **87**(27): p. 277202.
37. Willmott, P.R. and J.R. Huber, *Pulsed laser vaporization and deposition.* Reviews of Modern Physics, 2000. **72**(1): p. 315-328.
38. Kan, S., et al., *Formation Process of Nanometer-Sized Cubic Ferric Oxide Single Crystals.* Journal of Colloid and Interface Science, 1996. **178**: p. 673-680.

39. Bode, M., *Spin-polarized scanning tunneling microscopy.* Reports on Progress in Physics, 2003. **66**(4): p. 523-582.
40. Rodriguez, B.J., et al., *Electromechanical imaging of biomaterials by scanning probe microscopy.* Journal of Structural Biology, 2006. **153**(2): p. 151-159.
41. Guinier, A., *X-Ray Diffraction: In Crystals, Imperfect Crystals, and Amorphous Bodies*. 1994: Dover.
42. Drenth, J., *Principles of Protein X-ray Crystallography*. 1994: Springer.
43. Als-Nielsen, J. and D. McMorrow, *Elements of Modern X-ray Physics*. 2001: John Wiley & Sons, Ltd.
44. Bowen, D.K. and B.K. Tanner, *High Resolution X-ray Diffractometry and Topography*. 1998: Taylor & Francis, Ltd.
45. Clarke, J., *Principles and Applications of SQUIDs.* Proceedings of the IEEE, 1989. **77**(8): p. 1208-1223.
46. Wu, T., et al., *Substrate induced strain effects in epitaxial La(0.67-x)Pr(x)Ca(0.33)MnO3 thin films.* Journal of Applied Physics, 2003. **93**(9): p. 5507-5513.
47. Technology, C.a.C., *Typical Properties of Single Crystal Substrates*.
48. Millward, G.C., M.J. Calderón, and P.B. Littlewood, *Electronically soft phases in manganites.* Nature, 2005. **433**: p. 607-610.
49. Bueble, S., et al., *Influence of the ferroelastic twin domain structure on the {100} surface morphology of LaAlO3 HTSC substrates.* Surface Science, 1998. **400**: p. 345-355.
50. Dvorak, J., et al., *Are strain-induced effects truly strain induced? A comprehensive study of strained LCMO thin films.* Journal of Applied Physics, 2005. **97**: p. 10C102.
51. Filippetti, A. and W.E. Pickett, *Double-exchange-driven spin pairing at the (001) surface of manganites.* Physical Review B, 2000. **62**: p. 11571.
52. Zenia, H., et al., *Electronic and magnetic properties of the (001) surface of hole-doped manganites.* Physical Review B, 2005. **71**: p. 024416.
53. Choi, J., et al., *Surfaces of the perovskite manganites La1-xCaxMnO3.* Physical Review B, 1999. **59**: p. 1353.
54. Nelson, C.S., *Correlated polarons in dissimilar perovskite manganites.* Physical Review B, 2001. **64**: p. 174405.
55. Kittel, C., *Introduction to Solid State Physics*. Seventh ed. 1996, New York: John Wiley and Sons, Inc.
56. *CRC Handbook of Chemistry and Physics*. 72nd ed, ed. D.R. Lide. 1991, Boca Raton: CRC Press, Inc.
57. Morrish, A.H., *Canted Antiferromagnetism: Hematite*. 1994, River Edge, NJ: World Scientific Publishing Company, Ltd.
58. Amin, N. and S. Arajs, *Morin temperature of annealed submicronic α-Fe_2O_3 particles.* Physical Review B, 1987. **35**(10): p. 4810-4811.
59. Pauling, L. and S. Hendricks, *The crystal structures of hematite and corundum.* Journal of the American Chemical Society, 1925. **47**: p. 781.

60. Shull, C.G., W.A. Strauser, and E.O. Wollan, *Neutron Diffraction by Paramagnetic and Antiferromagnetic Substances.* Physical Review, 1951. **83**(2): p. 333-345.
61. Morin, F.J., *Magnetic Susceptibility of α-Fe2O3 and AFe2O3 with Added Titanium.* Physical Review, 1950. **78**: p. 819.
62. Antipin, M., et al., Sov. Phys.-Dokl., 1985. **30**: p. 257.
63. Dzialoshinskii, I., Z. Eksp. Teor. Fiz., 1957. **32**: p. 1547.

Appendices

Appendix A Langevin Function Derivation

The sections in this dissertation dealing with superparamagnetic behavior make heavy use of the Langevin function in describing the magnetic response of (super)paramagnetic materials to an applied magnetic field.

Consider a single magnetic dipole in a uniform magnetic field. This can represent either a nanoparticle or a single atom or molecule. The potential energy is then

$$U_m = -(\vec{m} \cdot \vec{B}) \tag{A.1}$$

If one considers a non-interacting ensemble of these dipoles held at a finite temperature, then the number of dipoles with a given orientation should be proportional to $\exp(-U/k_BT)$. This means that the number of dipoles per unit of solid angle that have an angle θ to the applied field is

$$n = n_0 \exp(\frac{mB\cos\theta}{k_BT}) \tag{A.2}$$

where n_0 is the total number of dipoles, N, divided by 4π. In order to derive the net moment in the ensemble this is then integrated over θ from 0 to π.

$$\begin{aligned} M &= \int_0^\pi n(m\cos\theta)2\pi\sin\theta d\theta \\ &= \frac{Nm}{2}\int_0^\pi \exp(\frac{mB\cos\theta}{k_BT})\cos\theta\sin\theta d\theta \\ &= Nm[\coth(\frac{mB}{k_BT}) - \frac{k_BT}{mB}] \end{aligned} \tag{A.3}$$

This function is known as the *Langevin function*, and it is the expected response for a paramagnetic system.

If k_BT is large compared to mB, then the exponential can be expanded to yield the *Curie Law* stated in Section 2.2.

$$\begin{aligned} n &= n_0 \exp(\frac{mB\cos\theta}{k_BT}) \\ &\approx n_0(1 + \frac{mB\cos\theta}{k_BT}) \end{aligned} \tag{A.4}$$

Implies $M = \frac{Nm^2 B}{3k_B T}$.

Appendix B Hematite Background

A recurring theme in this dissertation is the complex behavior that emerges in transition metal oxides. Oddly enough, this is very true for iron oxide. There are four common iron oxide compounds: FeO, α-Fe_2O_3, γ-Fe_2O_3, and Fe_3O_4. Each has its own peculiarities, but hematite (α-Fe_2O_3) has more than its fair share. In fact, Dr. Allan Morrish wrote a book in 1994 devoted entirely to the peculiarities of hematite.[57]

Hematite shares its structure with corundum (Al_2O_3). It can be indexed as either rhombohedral or hexagonal, with a space group designation of $R\bar{3}c$ or D_{3d}^6. This approximate structure had been determined as early as 1924, but a more complete determination of the structure was published in 1925 by Pauling and Hendricks.[59] However, neutron diffraction experiments performed by Shull [60] were necessary to truly understand the underlying antiferromagnetic structure.

The work of Shull and contemporaries was still not sufficient to entirely resolve the behavior of hematite through and above the Morin transition, which derives its name from a paper published by Morin in 1950.[61] The 56nm data set in Figure 4.20 is an example of this transition. The large change in susceptibility occurs at approximately 250 – 260K, which is known as the Morin temperature (T_M). The accepted value of T_M for modern single-crystal samples is 263K.

Below T_M, bulk hematite is a true antiferromagnet with moments aligned along the [111] axis. Above T_M, the moments flip to lie within the (111) plane. The common explanation for the excess moment above T_M is a small canting of the anti-aligned moments. The magnitude of this canting angle is somewhat difficult to measure, but it is believed to be less than 5.[57]

Since hematite is an oxide, super-exchange should play an important role in describing its behavior. According to Antipin, both direct and indirect exchange occur along the [111] direction.[62]

In order to model the Morin transition, Dzialoshinskii proposed a "Dzialoshinskii exchange" term in the Hamiltonian.[63]

$$H_D = -D \cdot [M_1 \times M_2] \tag{B.1}$$

where D is a constant vector along the [111] direction and $M_{1,2}$ are themagnetization sublattice vectors.

In addition to the Dzialoshinskii term, several more terms are necessary to construct a reasonably successful model. These are detailed in Morrish, but suffice it to say that they involve first and second order crystalline anisotropy terms, a first order anisotropic exchange term, a basal-plane anisotropy term, a magnetostriction term, and a Zeeman term for any applied field.

Vita

Dane Thomas Gillaspie was born in Casper, Wyoming on June 21st, 1975. He attended Fairdale Elementary School, East Junior High School, and Kelly Walsh High School. He was quite successful in high school, earning a National Science Scholarship and a University of Wyoming Trustees Fellowship in the process.

At the University of Wyoming, Dane earned a B.S. in Physics with a minor in German. He worked in the optics labs of both Dr. Moorman and Dr. Luk. In his free time, he enjoyed basketball, rock climbing, and even played club-level lacrosse for two seasons. He spent a semester abroad in Kassel, Germany in 1995. He was also a member of the University of Wyoming Honors Program, which provides in-depth, small group courses for motivated students.

After graduating from UW in 1997, Dane went to the University of Tennessee, Knoxville to pursue his doctorate. After a long courtship, he married Laura Denise Williamson on October 22nd, 2005. He finally put together a dissertation in time to graduate in May 11th, 2006. He has agreed to begin work at the National Renewable Energy Laboratory in Colorado as a postdoctoral fellow immediately after graduation.